

*Theoretical Investigations on Stability and
Reactivity of Zinc Oxide Polar Surfaces*

*Vom Fachbereich für Physik und Elektrotechnik
der Universität Bremen*

*zur Erlangung des akademischen Grades eines
Doktor der Naturwissenschaften (Dr. rer. nat.)
genehmigte Dissertation*

von

M. Sc. Jianping Xiao

1. Gutachter: Prof. Dr. Thomas Frauenheim

2. Gutachter: Prof. Dr. Thomas Heine

Eingereicht am: 18.03.2013

Tag des Promotionskolloquiums: 27.05.2013

**Theoretical Investigations on Stability and Re-
activity of Zinc Oxide Polar Surfaces**

Jianping Xiao

Universität Bremen

2013

ABSTRACT

To date, materials at nanoscale are used increasingly in many fields of science and technology. ZnO is an interesting metal oxide, which has been successfully synthesized in a wide variety of shapes and sizes. However, recent experiments indicate that ZnO NPs may be very toxic for biological systems. The toxicity of ZnO NPs can, however, be reduced by a small amount of Fe dopants. This is due to the fact that Fe dopants can suppress the dissolution of ZnO NPs and the number of released toxic Zn^{2+} cations. Though, the stabilization mechanism of ZnO NPs by Fe is still an open question.

In addition, ZnO is also employed as a support to improve the reactivity of catalysts. Even if the Cu/ZnO/ Al_2O_3 catalysts have been used in the industrial processes for many years, the active sites and synergy effects on these catalysts are still unknown. Neither Cu nor ZnO alone can achieve a comparable efficiency of methanol synthesis with respect to the mixed Cu/ZnO system. As the industrial synthesis is carried out under high temperature (> 500 K) and pressure (> 50 bar), numerous experimental studies performed under vacuum condition are to be questioned.

For the Fe-ZnO case, we first performed calculations of core-level spectroscopy (XANES) to compare with experimental spectra (ISEELS). It has been found that the Fe dopants are present as Fe^{2+} instead of Fe^{3+} in the ZnO NPs. Furthermore, using Mößbauer spectroscopy, we have found surprisingly that the local charge of Fe^{2+} in ZnO NPs is close to that of Fe^{3+} in Fe_2O_3 , instead of Fe^{2+} in FeO. This finding can explain well the observed stabilization of ZnO NPs by Fe doing.

In addition, we have studied the stability of ZnO polar and nonpolar surfaces in the presence of Fe dopants. Fe dopants stabilize only the ZnO polar surfaces, which are the least stable part of the ZnO NPs. This confirms that the reduced ZnO dissolution is due to the ZnO polar surfaces stabilization by Fe doing.

For the Cu/ZnO case, we have found that the catalytic properties are also correlated with the ZnO(000 $\bar{1}$) polar surface. Because Cu dopants destabilize the ZnO(000 $\bar{1}$) surface, oxygen vacancies are formed on this surface, accompanied by complete surface reduction. In other words, metallic monolayers can be formed and supported on the ZnO(000 $\bar{1}$) surface in the atmosphere of CO₂, CO, and H₂ gases. Furthermore, the reactivity of the supported metallic monolayers was optimized for CO₂ adsorption and the subsequent CO₂ reduction. This synergy effect can explain why the mixed Cu/ZnO system can achieve an optimal efficiency for methanol synthesis.

Moreover, we performed DFT calculations to propose an optimized catalyst, AgO/ZnO, for CO₂ reduction in the atmosphere of H₂ gas. It has been found that the Ag(111) monolayer supported on the ZnO(000 $\bar{1}$) surface has an optimized reactivity for CO₂ reduction. In practice, AgO/ZnO was proposed as the precursor to generate the supported Ag(111) monolayers in the atmosphere of H₂ gas.

CONTENTS

ABSTRACT.....	2
ACKNOWLEDGEMENTS	5
ABBREVIATIONS	7
PREFACE	9
1. INTRODUCTION	11
1.1 Toxicity of Nanomaterials	12
1.2 Fe-doped ZnO Nanoparticles	13
1.3 Cu/ZnO And Synergy Effects	16
1.4 ZnO Polar Surfaces	17
2. THEORETICAL METHODS	21
2.1 Density Functional Theory	22
2.2 Core-level Spectroscopy	26
2.3 Mößbauer Spectroscopy	28
3. POLAR SURFACES AND STABILITY	31
3.1 Fe-doped ZnO Bulk	31
3.1.1 Core-level Spectroscopy.....	31
3.1.2 Mößbauer Spectroscopy.....	34
3.2 Fe-doped ZnO Surfaces	35
4. POLAR SURFACES AND REACTIVITY	44
4.1 Active Sites on α -Fe ₂ O ₃ (0001) Surfaces	44
4.2 Synergy Effects on Cu/ZnO(0001) Surfaces	47
4.3 CO ₂ Reduction on Ag/ZnO(0001) Surfaces	49
5. CONCLUSIONS	51
5.1 Polar Surfaces and Stability.....	51
5.2 Polar Surfaces and Reactivity	51
REFERENCES.....	53
APPENDICES.....	61

ACKNOWLEDGEMENTS

I would like to acknowledge all the people, who have contributed scientifically to my PhD dissertation, as well as who helped me in different ways in my daily life during these years. Special Thanks:

To my supervisors, **Prof. Thomas Heine** and **Prof. Thomas Frauenheim**, for advising my research and providing me with plenty of opportunities to participate advanced academic conferences, workshops, and to visit other groups.

To **Dr. Agnieszka Kuc** for patiently teaching me step by step how to use these scientific packages and graphical programs at the initial stage; and many fruitful discussions for my work and corrections for all joint published articles.

To all collaborators, **Prof. Lars G.M. Pettersson**, **Dr. Suman Pokhrel**, **Prof. Lutz Mädler**, **Dr. Marco Schowalter**, **Prof. Andreas Rosenauer**, **Prof. Rainer Pöttgen** for impressive and fruitful discussions.

To **Dr. Binghai Yan** and **Dr. Ney Henrique Moreira** for kindly sharing your valuable experiences, which inspire me a lot to make interesting science.

To all **friends** and **colleagues**: Shuanping, Ke, Gao, Liangzhi, Min, Xingqiang, Jacky, and Svea, Andreia, Christof, Moloud, Aline, Volker, Jan, Bálint, Peter, Feiming, and Adriel, *etc.* in BCCMS; and Lyuben, Nina, Augusto, Andreas, Christian, Binit, Barbara, Wahid, Nour-dine, Mahdi, Lei, Rosalba, Ievgenia, Wenqing, Guilherme, Farjana, *etc.* in Jacobs University Bremen.

To **China Scholarship Council (CSC)** for financial support.

Dedicated to my wife and parents.

ABBREVIATIONS

NMs:	Nanomaterials
NPs:	Nanoparticles
ROS:	Reactive Oxygen Species
XRD:	X-ray Diffraction
(HR)TEM:	(High-Resolution) Transmission Electron Microscopy
SMSI:	Strong Metal-Support Interaction
GIXD:	Grazing Incidence X-ray Diffraction
STM:	Scanning Tunneling Microscopy
DFT:	Density Functional Theory
XPS:	X-ray Photoemission Spectroscopy
LDA:	Local Density Approximation
GGA:	Generalized Gradient Approximation
PW91:	Perdew-Wang Functional
PBE:	Perdew-Burke-Ernzerhof Functional
HSE:	Heyd-Scuseria-Ernzerhof Functional
XANES:	X-ray Absorption Near Edge Structure
(IS)EELS:	(Inner Shell) Electron Energy Loss Spectroscopy
MS:	Mößbauer Spectroscopy
IS and δ :	Isomer Shift
QS:	Quadrupole Splitting
EFG and V_{zz} :	Electric Field Gradient
FSP:	Flame Spray Pyrolysis
MD:	Molecular Dynamics
NVE:	Microcanonical Ensemble
NVT:	Canonical Ensemble

FM:	Ferromagnetic
AFM:	Antiferromagnetic
Fe-ZnO:	Fe-doped ZnO NPs
Cu/ZnO:	Cu-doped ZnO NPs
AgO/ZnO:	Ag-doped ZnO NPs
Fe _{Zn} and Fe _{subs}	Zn Sites Substituted by Fe
O _i and O _{int} :	Interstitial Oxygen
V _{Zn} and Zn _{vac} :	Zinc Vacancy
(<i>s, d, t, q</i>)V _O :	(25%, 50%, 75%, 100%) Oxygen Vacancy
(<i>m, b, t</i>)-Ag/ZnO:	(<i>mono, bi, tri</i>)-layer(s) Ag(111) supported by ZnO(0001)
Zn _{<i>n</i>} Cu _{<i>m</i>} :	<i>n</i> and <i>m</i> denote the number of atoms in the first cation layer.
Ag _{<i>n</i>} Zn _{<i>m</i>} :	<i>n</i> and <i>m</i> denote the number of atoms in the first cation layer.

PREFACE

My PhD dissertation is based on the work during the past three and a half years when I was studying as a PhD candidate in officially registered affiliation, *Bremen Center for Computational Materials Science (BCCMS) at Universität Bremen*, and as a guest PhD student in *School of Engineering and Science at Jacobs University Bremen*. Now I am preparing my PhD dissertation in an accumulative way based on five already published articles and letters in peer-reviewed journals and one more to be submitted manuscript.

In **Chapter 1**, I will first review the current applications and future prospects of NMs. Then, I turn to discuss an important semiconducting material, namely, ZnO. On one hand, it turns out that ZnO NMs are potentially toxicity for biological cells. This toxic performance can be eliminated by, *e.g.*, Fe doping. On the other hand, the recent studies of the industrial Cu/ZnO/Al₂O₃ catalysts and some controversial issues for the catalysts are introduced. Finally, I am going to analyze some intrinsic surface properties of ZnO NMs, particularly the ZnO polar surfaces.

In **Chapter 2**, I will shortly summarize the main theoretical methods, namely Density Functional Theory, Core-Level Spectroscopy, and Mößbauer Spectroscopy, which have been employed in the present investigations.

In **Chapter 3**, I am going to briefly discuss the Fe-ZnO NPs, Fe oxidation states inside the ZnO matrix, and the surface stabilization mechanisms. Theoretical results are also compared with the recent experimental studies performed by our collaborators. We have concluded that the reduced toxicity of Fe-ZnO NPs is due to the stabilization of ZnO polar surfaces. These results are discussed in details in the two published articles provided as Appendices A and B, and also in Section 3.2, where the most recent results, still unpublished, are presented.

Experimentally, the α -Fe₂O₃(0001) polar surface is well characterized, therefore, we have investigated this surface to correlate the reactivity of NMs with their polar surfaces. We have also carried out similar studies on the Cu/ZnO(000 $\bar{1}$) and AgO/ZnO(000 $\bar{1}$) surfaces towards the CO₂ reduction. These results are explained in details in the attached articles and letters (see Appendices C, D and E). Some insights are also briefly summarized in **Chapter 4**.

Finally, I will conclude my PhD dissertation on the basis of two findings, that is, correlation between Fe-ZnO polar surfaces and its stability, as well as correlation between Cu/ZnO polar surface and its reactivity, in **Chapter 5**.

Chapter 1

INTRODUCTION

1. INTRODUCTION

For NMs, it is like a coin that we can always see two sides. On one side, we are eager to make a good use of their surface reactivity to be served as, *e.g.*, catalysts. On the other side, we have to justify and eliminate their potential toxicity induced by their surface reactivity and instability. In this chapter, I will first review the current academic research of the nanoscience and applications of nanotechnology. Then, both toxicity and catalysis are briefly introduced based on the Fe- and Cu-doped ZnO NPs. Finally, I will discuss some basic concepts of ZnO polar surfaces.

1.1 Toxicity of Nanomaterials

Nanoscience is the study of the fundamental principles of materials with, at least, one dimension smaller than 100 nm. Nanotechnology is the application of these NMs embedded in functionalized devices at their nanoscale. Apparently, the nanotechnology was developing rapidly within the past decades. To date, our abilities to fabricate and manipulate materials at the nanoscale are much better than before, with new capabilities to prepare and synthesize highly functionalized NMs, and new instruments to investigate them.^[1]

It is no doubt that the application of NMs is already feasible in some fields. For instance, Intel and other computer companies sell computer chips of billions of dollars every year, which are packed with electronic modules at their nanoscale. Furthermore, a wide variety of computer hardwares, LED-based traffic lights, and electronic players account for billions or more in sales.^[2] According to some official estimates, the application of NMs promises to exceed the impact of the industrial revolution. It is probably going to occupy the market of more than \$1 trillion by 2015.^[3] In addition, functionalized NMs are not only available in electronic devices, but also have been increasingly utilized in medical fields for diagnosis, imaging, drug delivery, *etc.*

These successful applications of NMs are directly contributed from their unusual physicochemical properties at the nanoscale. Although it is pretty impressive from a physicochemical viewpoint, these novel properties of NMs raise concerns about negative effects on biological systems too, particularly on human cells and tissues. Indeed, some studies indicate that NMs are not inherently friendly to us and they destroy regular biological behavior at the subcellular, cellular, peptide, and protein scales.^[2, 4, 5] Furthermore, these unusual physicochemical properties of NMs can be always attributed to their characteristics of chemical composition, small size, large specific surface area, surface stability and reactivity, electronic properties, *etc.*

The small size of NMs results in a number of chemical reactions at the interface between the NMs and their biological surroundings, which could be responsible for a wide variety of toxicological effects. Some NMs can be easily dissolved and travel throughout the biological body, even accumulatively deposit in the target organs, directly penetrate cell membranes, and finally trigger some toxicological responses.^[5]

With the increased applications of NMs in the commercial goods, a growing public debate is also emerging on the environmental costs of NMs in comparison with their many benefits. By contrast, the nuclear power and genetically modified food have been recognized to be extremely dangerous already, while the public does not yet realize that some NMs have a noteworthy toxicity too, compared with their bulk forms.^[2] However this situation could change rapidly with public interests on this topic. To date, more and more attention is paid from both experimental and theoretical sides. Therefore, the elimination of potential toxicity regarding the applications of NMs is a prerequisite for the acceptance of these new materials and technologies in the society.^[6, 7, 8, 9]

1.2 Fe-doped ZnO Nanoparticles

Zinc Oxide (ZnO) is a semiconducting material with a band gap of 3.4 eV and large exciton energy of 60 meV. ZnO NMs have been intensively investigated from physical,

chemical, and biological point of view because of their promising physicochemical properties and successful applications in consumer's products.^[10] A large variety of ZnO NMs with different shapes and sizes, including nanowires,^[11] nanobelts,^[12] nanorods,^[13] nanorings,^[14] nanohelices,^[15] *etc.*, have been already synthesized and characterized in details. These ZnO NMs can be functionalized by capping organic molecules, polymers, biomolecules, and inorganic thin films for biological and medical applications.^[16]

However, a number of experimental hazard assessments of ZnO nanoparticles (NPs), in comparison to other NMs, *e.g.* TiO₂, CuO, CeO₂ NPs, *etc.*, were carefully investigated by many research groups.^[17] It was observed by Moos *et al.*^[18] that the ZnO NPs are more toxic compared with ZnO at micron scale. Then, Monika *et al.*^[19] have investigated comparatively the toxicity of ZnO and CuO NPs towards ciliated protozoa tetrahymena thermophila, where they found that nanoscale ZnO was remarkably more toxic with respect to CuO NPs under the same conditions. Similarly, Hsiao *et al.*^[20] concluded that the smaller ZnO NPs are more toxic than the larger ones. Moreover, the toxicity of ZnO NPs is apparently higher compared with TiO₂ NPs of comparable size. In addition, the ZnO NPs exhibit acute toxicity towards earthworms (*Eisenia fetida*), while it has not been observed for TiO₂ NPs in a terrestrial system. This result was obtained by Canas *et al.*^[21] in the *in vivo* experiments. Obviously, a more convinced assessment of ZnO NPs toxicity is urgently required to elucidate the mechanism at the atomistic level, and a way to reduce the toxicity is necessary to be carried out, in order to achieve the public acceptance for ZnO NMs.

Numerous *in vitro* and *in vivo* testings have been performed by the group of Nel and collaborators to justify and elucidate the toxicity of ZnO NPs.^[22] They found that ZnO NPs induce *in vitro* toxicity, leading to the generation of reactive oxygen species (ROS), oxidant injury, excitation of inflammation, and cell death, while CeO₂ and TiO₂ NPs do not.^[23] The notable toxicity of ZnO NPs is consistent with the previous experiments and the corresponding mechanism was discussed. They claimed that the dissolution of ZnO NPs correlates well with the toxicity, that is, the observed toxicity results from dissolved Zn²⁺ cations.

Moreover, the subsequent *in vivo* measurements of rodent lung and zebrafish embryos were also consistent with the previous *in vitro* experiments.^[24]

In order to understand the relation between structure and toxicity, experimental characterizations and theoretical studies of ZnO NPs are further carried out.^[23] These experimental characterizations were performed concerning structural and electronic features. It was found that the toxicity of ZnO NPs can be significantly reduced by Fe doping as the ZnO dissolution is decreased, where the ZnO wurtzite crystalline structure is not changed essentially by Fe dopants, what was determined by X-ray Diffraction (XRD) patterns and Transmission Electron Microscopy (TEM). Therefore, Fe²⁺ cations substitution for Zn²⁺ sites was proposed initially based on these experimental results in ref [24].

On one hand, this finding is remarkable, considering that a significant amount of Fe²⁺ (~10%) can be incorporated into ZnO wurtzite structure with only minor changes in the ZnO lattice parameters. On the other hand, in the air the ferric cation (Fe³⁺) is more stable than the ferrous cation (Fe²⁺). Once in ZnO NPs the Fe³⁺ cation is present, to achieve lattice charge balance, some amount of defects, like interstitial oxygen (O_i) and zinc vacancy (V_{Zn}), is required. As far as a number of defects are formed in Fe-ZnO (Fe-doped ZnO) NPs, the structure of Fe-ZnO should not be as perfect as we have observed. Also the stability of Fe-ZnO should not be comparable with respect to the pure ZnO NPs without defects. Hence, it is quite surprising experimental results from perspective of the Fe oxidation state.

As we have mentioned, dissolvable Zn²⁺ cations are quite critical for the toxicity of ZnO NPs, which are tightly correlated with the ZnO dissolution. Furthermore, the ZnO dissolution should be related directly to the stability of ZnO NPs, in particular, the stability of ZnO surfaces. However, the stability of ZnO NPs and surfaces is unknown in the presence of Fe dopants. Thus, it requires further theoretical investigations to elucidate the stabilization mechanism of Fe-ZnO NPs and the correlation with the toxicity of ZnO NPs.

1.3 Cu/ZnO And Synergy Effects

In addition to the toxicity, NMs also play a significant role in heterogeneous catalysis, because we can efficiently make use of their surface effects. It is well known that ZnO is an active catalyst and catalyst's support. One of the most successful applications of ZnO is the industrial process of methanol synthesis using the Cu/ZnO/Al₂O₃ catalysts with gaseous H₂, CO, and CO₂ mixture.^[25] This catalytic system is also of recent interests for the potential capability of CO₂ capture and reduction. As the mechanism is not yet understood, it is not feasible to utilize a Cu/ZnO-based catalyst for CO₂ reduction until now.

Despite the fact that the methanol synthesis technology has been in industrial application for nearly 100 years, several key mechanistic questions have not yet been answered. CO₂ hydrogenation was assumed to be the main reaction pathway for methanol synthesis,^[26] until the isotope labeling experiments by Chinchin *et al.*^[27] Although CO₂ was proposed to be the main carbon source in the methanol synthesis, CO₂ adsorption and dissociation on the Cu(100) surface are not as good as expected, compared with other transition-metal surfaces, that is, Fe, Co, and Ni(100).^[28] Hence, we can not explain why the Cu/ZnO is optimal for the industrial methanol synthesis. That means we do not know what respective roles the ZnO and Cu play in the Cu/ZnO system.

In addition, the active sites and surfaces on the Cu/ZnO/Al₂O₃ catalysts are not clearly specified. It was first proposed that ionic Cu⁺ cations are the active catalytic centers. However, it has also been reported that the catalyst activity scales linearly with the metallic Cu surface area. Recently, Behrens *et al.*^[29] reported a combined experimental and theoretical (DFT) study. The authors found that there is an essential difference between pure Cu surfaces and the industrial Cu/ZnO/Al₂O₃ catalyst. They claimed that most of the Cu surfaces are not active at all. A small fraction of the catalyst's surface, namely, Zn-decorated Cu(211) steps, mainly contributes to the active sites of the industrial catalyst.

One possible answer to the above problem is the strong metal-support interaction (SMSI),^[30] where the activity of Cu surfaces can be improved significantly compared with

the surfaces without any support. However, the synergistic effects on the Cu/ZnO interface are not yet clarified.

1.4 ZnO Polar Surfaces

Toxicity and catalytic properties of ZnO NMs are driven by the active sites present on the surfaces of finite materials. As the size of NPs is very small compared with their bulk forms, the surface to bulk ratio increases as the surface area increases. The surfaces created by confinement from bulk to nanoparticles can be stable or instable. The latter ones are responsible for the reactivity of NPs with the environment.

For crystalline structures of ionic compounds, a particular type of surfaces can be defined by its orientations with respect to the surface plane. The formal definition for these surface types can be achieved by considering the projection of the accumulative dipole moment of the repeated unit cell on the perpendicular direction to the surface (**Figure 2.1**). If, for a specific surface orientation, the accumulative dipole moment is non-zero, such a surface is called polar surface. In contrast, a nonpolar surface has zero dipole moment. ^[31]

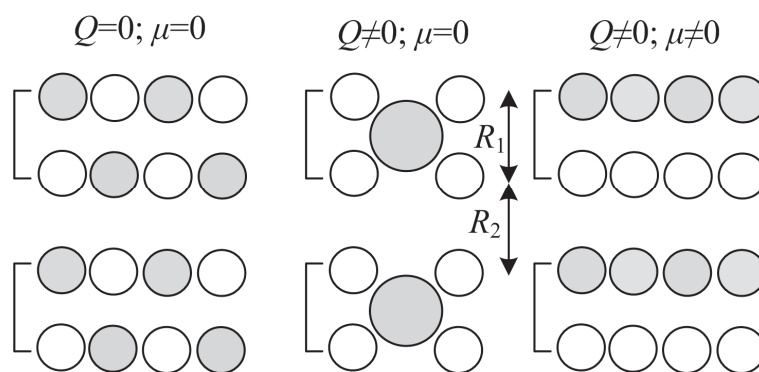


Figure 1.4.1 Three surface types according to the Tasker^[32,33] rule. Q and μ are the layer charge density and dipole moment in the repeated unit perpendicular to the surface, respectively.

ZnO possesses two types of dominant surfaces: nonpolar ZnO(10 $\bar{1}$ 0) and ZnO(11 $\bar{2}$ 0) surfaces, and polar ZnO(0001) and ZnO(000 $\bar{1}$) surfaces. The two polar surfaces exhibit a nonzero dipole moment parallel to the surface normal (**Figure 1.4.1**, right) and are highly

instable, while the other two nonpolar surfaces are very stable and have zero dipole moment (**Figure 1.4.1**, left). The dipole moment of the ZnO bulk is oriented along the crystal-line [0001] direction. Meanwhile, the presence of a finite dipole moment per surface area for polar surfaces gives rise to a macroscopic electrostatic field, which diverges with the size of ZnO NPs. This phenomenon is well-known as polar catastrophe.^[32]

There are three strategies to suppress the dipole moment and stabilize polar surfaces. The first strategy is closely associated with the reconstruction of polar surfaces, where certain surface defects are created. Second, adatoms or adsorbed molecules might stabilize polar surfaces. These two stabilization mechanisms were observed in certain oxide polar surfaces, also supported by theoretical calculations.^[31,32] The third means is to transfer a part of charge from the ZnO(000 $\bar{1}$) surface to the ZnO(0001) surface. The stoichiometric polar surfaces can maintain stability without surface reconstructions.

For the polar surfaces, shown in **Figure 1.4.1**, two inequivalent layers (in grey and white) of charge densities, $\pm\sigma$, are alternatively stacked along the normal to the surface. As the instability of ZnO polar surfaces scales with the size of the samples, namely $E=2\pi NR_1\sigma^2$ (N is the number of bilayers), these surfaces can be stabilized even for extremely small particle sizes. For macroscopic samples, even at the nanoscale, however, the electrostatic field becomes so large that either the electronic or geometric structures of the polar surface is compromised.^[33]

In the initial stage, most studies failed to observe any ZnO(000 $\bar{1}$) surface reconstructions.^[34] In other words, there are no observations of different surface structures from a simple bulk-like termination. The experimental studies always reported (1 \times 1) diffraction patterns of ZnO(000 $\bar{1}$) with ideal bulk-like termination.^[35] For the ZnO(0001) surface, previous studies based on grazing incidence X-ray diffraction (GIXD) provided evidence with a high degree of disordered surface. Fitted experimental data hold the assumption that ~25% Zn vacancies are formed.^[31]

In a recent scanning tunneling microscopy (STM) study performed by Dulub *et al.*^[36] concerning the ZnO(0001) surface, a large number of steps were observed, which result in a rather rough surface with many triangular-shaped terraces. DFT calculations indicate that the observed triangular terraces can compensate the electrostatic instability and cancel the dipole moment.^[36] In contrast, for the ZnO(000 $\bar{1}$) surface, the O 1s line detected by photoelectron spectroscopy (XPS) always showed a shoulder at higher binding energies,^[37] which corresponds to the presence of hydroxyl (OH) groups. More investigations regarding hydrogen-free ZnO(000 $\bar{1}$) surfaces were carried out and a clear (1 \times 3) reconstruction have been observed. Therefore, one of reasonable explanations for observed perfect ZnO(000 $\bar{1}$) surfaces is attributed to the hydrogen contamination.^[31]

A scenario of charge transfer in-between the two polar surfaces is also a possible stabilization mechanism. As a result, the charge transfer of $\sim 0.25 e$ should cause the formation of partially filled surface states, which was supported by a theoretical study.^[38] However, this approach is questionable as the metallic characteristics have never been detected for ZnO polar surfaces. All in all, ZnO polar surfaces are still controversial without any consistent conclusions from both experiment and theory.

Chapter 2

THEORETICAL METHODS

2. THEORETICAL METHODS

In this chapter, the basic approaches and approximations used in this dissertation are explained. Section 2.1 discussed the Schrödinger equation, Density Functional Theory (DFT), and the exchange-correlation functionals. Sections 2.2 and 2.3 focus on the theoretical background of the core-level spectroscopy and the Mößbauer spectroscopy, respectively. They are discussed with respect to methods described in Section 2.1.

2.1 Density Functional Theory

There are many fields within the physical sciences and engineering, where a key issue to scientific interpretations and technological applications is to understand and also manipulate the properties of matters at their atomistic level. The Schrödinger equation^[39] (Equ 2.1) provides us an approach to describe the properties of matters with well-defined structures, in which we need to define not only the atomistic structures, but also the nuclear-electron interactions. In the Schrödinger equation:

$$\hat{H}\Psi(\mathbf{R}, \mathbf{r}) = E\Psi(\mathbf{R}, \mathbf{r}) \quad (2.1)$$

\hat{H} is the Hamiltonian operator, E is the eigenvalues, and $\Psi(\mathbf{R}, \mathbf{r})$ is the electron wave function in terms of nuclear (\mathbf{R}) and electronic (\mathbf{r}) coordinations. The energy of an interacting system of electrons in a well-defined nuclear coordinates can be described as follows:

$$E = E_K + E_V + E_U \quad (2.2)$$

Here, E_K is the electron kinetic energy, E_V and E_U define the interaction energies between each electron and atomic nuclei, and electron-electron coupling, respectively.^[40] As the ground state energy of electrons (E) is time independent, we can solve the electronic wave function, $\Psi(\mathbf{R}, \mathbf{r})$, in terms of spatial coordinations of these nuclei and electrons.

As the atomic nuclei are much heavier than individual electrons, each proton and neutron in a nucleus has more than 1800 times the mass of an electron. This hints that,

generally speaking, electrons always respond much more rapidly to perturbations in their surroundings than the nuclei. Therefore, the Schrödinger equation can be treated separately for the nuclei and electrons, which is known as the *Born-Oppenheimer* approximation:^[41,42]

$$\Psi(\mathbf{R}, \mathbf{r}) = \Psi_{el}(\mathbf{R}; \mathbf{r})\Psi_{nuc}(\mathbf{R}) \quad (2.3)$$

where $\Psi_{el}(\mathbf{R}; \mathbf{r})$ and $\Psi_{nuc}(\mathbf{R})$ are the electronic and nuclear parts, respectively.

According to the above approximation, we can decompose the solution of the Schrödinger equation into two steps. First, we solve the Schrödinger equation of the system with fixed atomic positions using a correct description for electronic coupling. Then, the second derivative of the potential energy with respect to the coordinations can be adopted to calculate the force on individual atoms. Finally, the atomistic structures can be updated with a small displacement of individual atomic coordinates. The lowest energy state is obtained as the ground state. Once we are able to calculate this potential energy surface, we can solve the Schrödinger equation.^[42,43]

As the number of electrons is considerably larger than the number of nuclei, the dimensions of Equ. 2.3 highly depend on the number of electrons. If, for example, we were interested in a single CO₂ molecule, the full wave function is a function of 66 dimensions (3 degrees×22 electrons). For any crystalline system, *e.g.* ZnO, we have many more atoms to deal with (for ZnO it would be 800 atoms). The full description of electronic wave function requires for the ZnO example already 45600 dimensions. It becomes not feasible to solve the Equ. 2.3 and further approximations are needed.

In addition, there is another fundamental problem when we consider the solution of the Hamiltonian, which stands from the electron-electron interaction, a typical many-body problem. The Schrödinger equation, defined by only considering individual electronic wave function, is not relevant when the electron-electron interactions are neglected.

In the middle of 1960s, the first theorem, proposed by Hohenberg and Kohn, was stated as: *The energy of ground state from the Schrödinger's equation is a unique functional of the electron density.*^[44] This theorem emphasizes that there is a one-to-one corresponding relation between the wave function and the electron density in the ground state. It suggests that we can think about solving the Schrödinger equation by finding a function of the electron density in terms of three spatial variables rather than a wave function of $3N$ variables.^[42]

Although the first Hohenberg-Kohn theorem points out that a functional of the electron density can be served to solve the Schrödinger equation, we still know nothing regarding the form of the exact functional. The second Hohenberg-Kohn theorem defines an important property of the functional: *The ground state energy can be obtained variationally: the density which minimizes the total energy is corresponding to the exact ground state density.*^[42] Therefore, we can obtain a one-to-one corresponding relation between the electron density and minimum energy. This is known as *Density Functional Theory (DFT)*.

Although the DFT approach gives a nice prospect, the full solution of equation described by the exact DFT is still formidable. Furthermore, on the basis of single-electron approximation, Kohn and Sham proposed an approach to describe the Schrödinger equation formulated in Equ 2.4 as follows:

$$\left[-\frac{1}{2}\nabla^2 + v_{\text{eff}}(r) \right] \phi_i(\mathbf{r})^{KS} = \varepsilon_i \phi_i(\mathbf{r})^{KS} \quad (2.4)$$

where the $v_{\text{eff}}(\mathbf{r})$ is composed of three potentials, $V(\mathbf{r})$, $V_{\text{H}}(\mathbf{r})$, and $V_{\text{xc}}(\mathbf{r})$. The first and second potentials are the descriptions of the electron-nuclei and the electron-electron Coulomb repulsion, respectively. The second potential, however, includes an unphysical description, namely, *self-interaction energy*. Large effort is drawn to correct this issue.^[42] Finally, all difficulties of physical descriptions are merged in the term of the exchange-correlation potential ($V_{\text{xc}}(\mathbf{r})$). Because the exchange-correlation functional is defined as the “functional deri-

vation" of the exchange-correlation potential, we need to solve the Kohn-Sham equations iteratively.^[45]

Up to now, a reasonable description of the exchange-correlation functionals becomes the key to solve the Kohn-Sham equation. A vast number of approximations have been proposed to describe this functional. The first approximation was called local density approximation^[46] (LDA), obtained from a uniform electron gas. Although the LDA functional fails for most realistic systems in comparison with experimental data, it gives us a way to completely define the Kohn-Sham equations. The development of functionals is always an active research in DFT community to obtain more precise results. An improvement is obtained by the so-called generalized gradient approximation^[47] (GGA), which considers not only the local electron density but also the gradient of the electron density. Two important functionals, widely used in the solid-state calculations, at the GGA level, are Perdew-Wang^[48] and Perdew-Burke-Ernzerhof^[49] functionals.

As the Kohn-Sham equation approximates a fictitious system of noninteracting electron, the most used functionals always underestimate the electron-electron interaction strength. In contrast, the exact-exchange description, which was proposed by Hartree and Fock,^[50] gives overestimation of the electron-electron interactions in a realistic system. In 1993, Becke proposed a hybrid description of exchange-correlation functional, which is known as hybrid B3LYP functional. This functional achieves a lot of success for studies in chemistry. Adamo and Barone have obtained analogous improvements by introducing exact exchange into standard PBE functional (PBE0).^[51] Furthermore, Heyd, Scuseria, and Ernzerhof proposed another hybrid functional of adjustable short-range interactions (HSE).^[52] These hybrid functionals have achieved significant improvements for descriptions of electronic band structure of many correlated systems.

2.2 Core-level Spectroscopy

Core-level spectroscopy of solids is due to electronic transition from a core level of a probed atom to the conduction band. This spectroscopy can be used to describe a variety of experimental phenomena correlated with such processes. Core-holes can be generated using X-ray or electron beam in a TEM instrument. As the core level is quite localized, core-level spectroscopy provides an informative picture of the local electronic structures around the probed atomic site.

X-ray absorption near edge structure (XANES) is one of the core-level spectroscopies, which has been applied in many fields and gained great reputation due to the use of synchrotron radiation sources. There are two well-known theoretical approaches to calculate XANES spectra. A well developed approach is the transition potential DFT method,^[53] which is based on Slater's transition-state approximation. The other approach is provided by *multiple-scattering* theory. In this section, we first introduce the general muffin-tin approximation in DFT approach, followed by discussion of selected mathematical concepts of Green's function and its application within the multiple-scattering theory proposed by J. J Rehr *et al.*^[54]

Now, let us imagine a scattering process from potential, v^i , of a huge number of atoms or ions. Each of these atoms makes a significant contribution within a spherical and non-overlapping scattering regions of a finite radius, r . The atoms close to the scattering centers contribute more than the other atoms. The potential is assumed to be constant in the interstitial region, that is, outside of the spherical regions (see **Figure 2.2.1**).^[55]

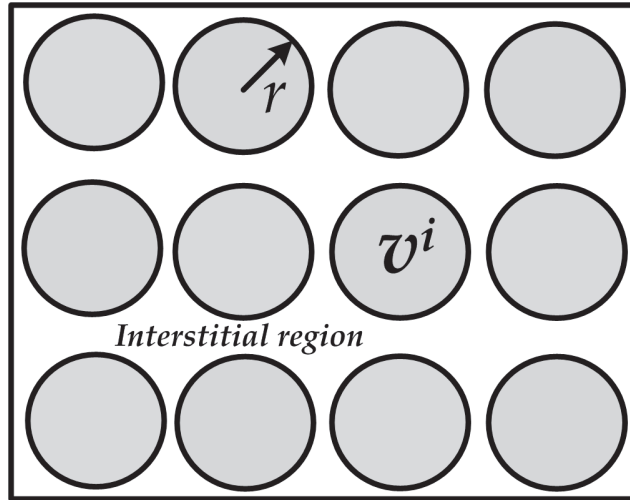


Figure 2.2.1 Scheme of Muffin-tin approximation represented by grey spheres with radius, r , and potential, v^i , and white interstitial region.

The muffin-tins provide atomic scattering centers described by atomic phase shifts. Green's function propagators are used to connect these scattering centers. In a scattering process, propagation of a photoelectron in such a muffin-tin potential, v , can be described by Hamiltonian:

$$H = H_0 + V, \quad (2.5)$$

$$V = \sum_i v^i, \quad (2.6)$$

where H_0 is the kinetic energy operator. We can seek the stationary solution $|\varphi\rangle$ with the energy, E :

$$H|\varphi\rangle = E|\varphi\rangle, \quad (2.7)$$

which is given as:

$$(E - H_0)|\varphi\rangle = V|\varphi\rangle. \quad (2.8)$$

For a free electron, Green's function G_0 is defined as:

$$(E - H_0)G_0(\mathbf{r}, \mathbf{r}'; E) = \delta(\mathbf{r} - \mathbf{r}'). \quad (2.9)$$

In order to calculate XANES spectra, we can employ a description of one-particle Green's function. According to the Fermi's golden rule and the dipole selection rule:^[54]

$$\mu(E) \propto -\frac{2}{\pi} \text{Im} \langle i | \hat{\epsilon} \cdot r' G_0(r, r'; E) \hat{\epsilon} \cdot r' | i \rangle. \quad (2.10)$$

The total Green's function is considered as the contribution from the central probed atom (G^0) and the neighboring scattering atoms (G^{SC}):

$$G = G^0 + G^{SC} \quad (2.11)$$

$$G^{SC} = G^0 T G^0 + G^0 T G^0 T G^0 + \dots \quad (2.12)$$

Herein, the mathematical solution of the G^{SC} equation is neglected. Please refer to the articles of J. J Rehr *et al.*^[54] for details.

In addition, an electron beam can be used to replace X-ray as incident radiation source to generate core-level spectroscopy. XANES and core-level EELS are described using very similar physical concepts, therefore, they are quite comparable from the theoretical point of view. Therefore, the details of the theoretical approach of the core-level EELS calculations are not discussed here.

2.3 Mößbauer Spectroscopy

Mößbauer spectroscopy (MS) is an analytical technique based on the recoil-free resonance fluorescence of *gamma*-photons.^[56] It also gives information about the electric monopole interaction on the resonant nucleus of Mößbauer-active atoms via the hyperfine interactions.^[57] As the probed samples and reference absorbers are located in different local environments, their nuclear energy levels are shifted differently (see **Figure 2.3.1**). MS isomer shift (IS) is one of the important parameters to determine the chemical states and the electronic charge density at the nucleus of the probed atom. Furthermore, MS quadrupole splitting (QS) has been accepted as a choice to identify the local structure of the probed atoms.

The MS technique has been shared with solid-state chemistry as a golden standard for determination of Fe^{3+} and Fe^{2+} in solid materials, particularly for a number of geological compounds.^[57] In order to interpret the measured data (IS and QS) with MS technique, comparable results from theoretical calculations are highly desirable. The MS parameters are all correlated with the electron (or spin) density, which can be obtained from the wave function solving the Schrödinger equation based on self-consistent iterations.^[58]

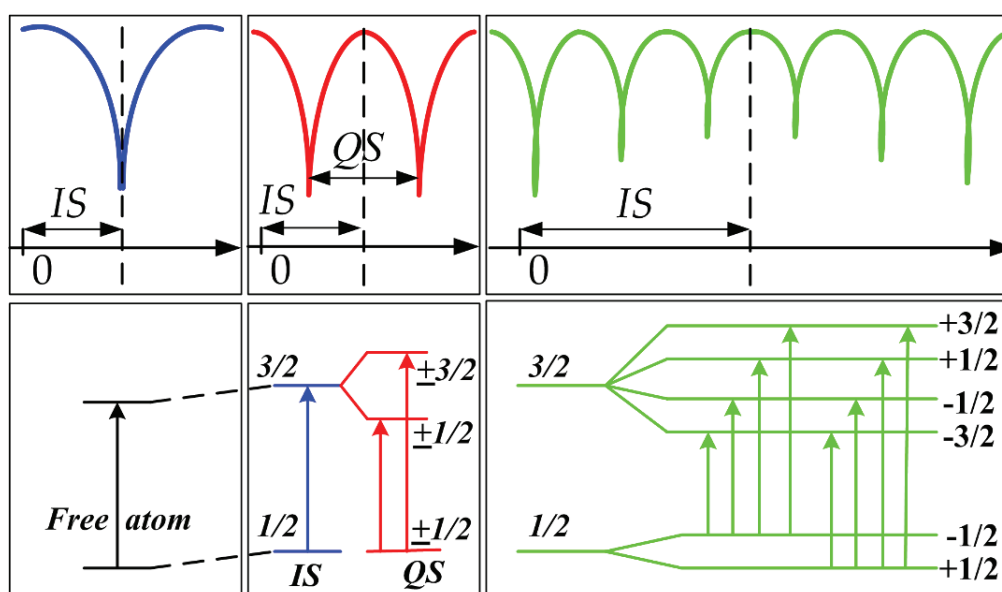


Figure 2.3.1 Schematic representations of the MS parameters.^[57] The isomer shift (IS) - blue curves, the quadrupole splitting (QS) - red curves, and the hyperfine - green curves.

In practice, the Mößbauer IS value of a probed atom can be obtained by comparing its electron density at the nucleus with that of a reference system. As iron is the most common Mößbauer-active element, the body centered cubic iron (α -Fe) is always served as the reference. Therefore, the Mößbauer IS value (δ) can be calculated as following:^[58]

$$\delta = \alpha(\rho_0^S - \rho_0^R), \quad (2.13)$$

where α is a constant that can be estimated based on calibration, the two terms in the parenthesis account for the charge density at nucleus for the sample and the reference system, respectively. In the work of Wdowik *et al.*,^[59] α was found to be $-0.29 \text{ a.u.}^3 \text{ mm s}^{-1}$, which is

slightly larger than the calibrated value by Duff *et al.*^[60] of $-0.23 \text{ a.u.}^3 \text{ mm s}^{-1}$. In a recent theoretical work, Navarro *et al.*^[61] obtained a calibrated value of $-0.25 \text{ a.u.}^3 \text{ mm s}^{-1}$ on the basis of DFT calculations using WIEN2K code.

In addition, the Mößbauer QS is directly proportional to the product of the nuclear quadrupole moment, Q , multiplied by the electric field gradient (EFG), V_{zz} . The nuclear quadrupole moment Q was determined by Dufek *et al.*^[62] to be $\sim 0.16 \text{ barn}$ ($1 \text{ barn} = 10^{-28} \text{ m}^2$) based on comparisons between theoretical and experimental data for a number of Fe-containing compounds. The EFG value can be directly calculated from the electronic and nuclear charge distribution as follows:^[58]

$$V_{zz} = \int \rho(r) \frac{2P_2(\cos\theta)}{r^3} dr, \quad (2.14)$$

where P_2 is the second-order Legendre polynomial, which can be obtained from the projection of the $l = 2$ component of the self-consistently converged total charge density.^[58]

Chapter 3

POLAR SURFACES AND STABILITY

3. POLAR SURFACES AND STABILITY

In order to understand the stabilization mechanism of ZnO NPs by Fe doping, we have performed three stepwise investigations of ZnO bulk and surfaces. For the ZnO bulk, we have employed two approaches, that is, the core-level and the Mößbauer spectroscopies, to determine the oxidation states and the local charge of Fe dopants. Last but not least, we have investigated surface models to correlate the reduced dissolution with the stability of ZnO surfaces.

3.1 Fe-doped ZnO Bulk

3.1.1 Core-level Spectroscopy

In the previous experiments, the results indicated that the overall lattice structure of ZnO is not significantly distorted by Fe dopants up to about 10 at % and that Fe is almost homogeneously distributed inside the NPs, replacing Zn atoms at their lattice sites. This result might indicate that the oxidation state of Fe is that of the ferrous cation, Fe^{2+} . In addition, a ferric cation, Fe^{3+} , can be obtained by intrinsic Zn vacancy and interstitial oxygen at the neighboring sites of Fe dopants.

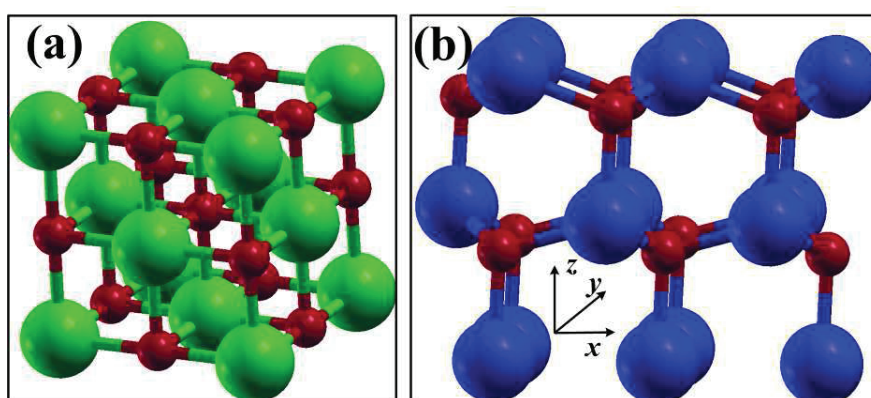


Figure 3.1.1 Atomistic arrangements of FeO and ZnO in the crystalline phases of rocksalt and wurtzite, respectively. Fe: green, Zn: blue, O: red.

As the most stable Fe^{2+} cations are in the rocksalt phase, shown in **Figure 3.1.1**, a significant amount of Fe^{2+} cations in the wurtzite structure was not expected. In addition, the previous experiments were carried out in the atmosphere of air.^[23] The Fe^{2+} cation is unusual because the Fe^{3+} is the most stable state in such atmosphere. The oxidation state of Fe dopants can be identified by their $3d$ orbitals occupancy. In the previous experiments, ISEELS spectra show a single signal of white line, which may correspond to the $2p$ - $3d$ transition of Fe dopants. Moreover, one of Fe oxidation states must be dominant, as we have not observed the chemical shifts between Fe^{2+} and Fe^{3+} cations. Hence, we have performed systematic theoretical calculations to elucidate these issues.

First-principles calculations were used to investigate the structural and electronic properties of Fe-ZnO nanoparticles. Based on extensive validation studies, surveying various density functionals, the hybrid functional PBE0 was selected to calculate the structures, formation energies, and electronic properties of Fe in ZnO with Fe concentrations of 6.25, 12.5, and 18.75 at %. Substitution of Zn by Fe, zinc vacancies, and interstitial oxygen defects were studied. High-resolution ISEELS measurements and XANES calculations for both Fe and O atoms were performed. The results show that Fe-ZnO NPs are structurally and energetically more stable than the isolated FeO (rocksalt) and ZnO (wurtzite) phases. Fe dopants distribute homogeneously in ZnO nanoparticles and do not significantly alter the host ZnO lattice parameters. Simulations of the absorption spectra demonstrate that Fe^{2+} dominates in the Fe-ZnO NPs reported recently, whereas Fe^{3+} is only present as a trace.

We have published a joint article with our collaborating experimental groups in **Small**, 2011 (7), 2879–2886.

Evidence for Fe^{2+} in Wurtzite Coordination: Iron Doping Stabilizes ZnO Nanoparticles,
J. Xiao, A. Kuc, S. Pokhrel, M. Schowalter, S. Porlapalli, A. Rosenauer, T. Frauenheim, L. Mädler,
L.G.M. Pettersson, T. Heine*

Please refer to the APPENDIX A for detailed results and discussions.

3.1.2 Mößbauer Spectroscopy

The Mößbauer spectroscopy isomer shift (IS) is an important parameter, which results from the Coulomb interaction between the nucleus and electron density at the site of the nucleus. As the oxidation state is always assumed to be tightly correlated with the charge density at the nucleus, the Mößbauer IS was often employed to determine the oxidation state of the probed element.

The IS of Fe^{3+} is typically close to 0.3 mm s^{-1} in the corundum Fe_2O_3 structure, while the IS of Fe^{2+} in the rocksalt FeO structure is always observed at around 0.9 mm s^{-1} . Our investigations, however, demonstrate that the Mößbauer IS is just correlated with local charge and not oxidation states of Fe dopants. In addition, we found that the QS values can provide more insights to distinguish between different types of Fe dopants in a ZnO matrix.

In order to evaluate the oxidation state of Fe dopants, we have carried out systematic calculations of the Mößbauer IS and QS of FeO , Fe_2O_3 , Fe-ZnO , and $\text{Fe-ZnO-}n\text{H}$ ($n = 1-4$) systems. The Mößbauer IS of 0.3 mm s^{-1} and QS of 0.83 mm s^{-1} for Fe in Fe-ZnO NPs correspond to the presence of Fe^{2+} ions in these phases. This result arises from the charge depletion on the ZnO matrix, supported by the compression of the Fe-O bond lengths of the tetrahedral Fe site in the wurtzite ZnO lattice.

We have published a joint article with our collaborating experimental groups in *Chem. Eur. J.*, **2013** (19), 3287-3291.

Fe-doped ZnO Nanoparticles: The iron oxidation number and local charge studied by ^{57}Fe Mößbauer spectroscopy and DFT,

J. Xiao, A. Kuc, S. Pokhrel, L. Mädler, R. Pöttgen, F. Winter, T. Frauenheim and T. Heine,*

Please refer to APPENDIX B for detailed results and analyses.

In a word, we have calculated the stability of Fe^{2+} and Fe^{3+} in ZnO wurtzite structure, which indicates that Fe^{2+} prefers to be present at the substitutional sites of Zn lattice. In addition, the same conclusion can be drawn from the computed XANES spectra, which was compared with measured ISEELS data. Furthermore, joint experimental and theoretical evidence based on the Mößbauer spectroscopy demonstrates that the atomic charge of Fe^{2+} dopants in ZnO is, however, close to that of Fe^{3+} in Fe_2O_3 phase. Therefore, the Mößbauer IS is not efficient to determine the Fe oxidation states in mixed phases. On the other hand, QS values give more detailed information and our results are in line with Fe^{2+} as predominantly present in the ZnO NPs prepared by FSP.

3.2 Fe-doped ZnO Surfaces

As the most important chemical reactions always take place on the surfaces, in order to understand the reduced dissolution and toxicity by Fe doping we need to consider both contributions of Fe, which are inside ZnO bulk and on the surfaces. In principle, we could expect Fe-ZnO NPs to be stabilized inside bulk phase, as well as on the surfaces. **Figure 3.2.1** shows the perfect polar and nonpolar surfaces, while the defective polar surface models are given in **Figure 3.2.2**.

ZnO surfaces, including polar $\text{ZnO}(000\bar{1})$ and $\text{ZnO}(0001)$ surfaces, and nonpolar $\text{ZnO}(10\bar{1}0)$ and $\text{ZnO}(11\bar{2}0)$ surfaces, have been simulated using 2D periodic slab models cut out from the bulk forms using Miller indices. In order to avoid interactions between Fe dopants in one unit cell and its images in the neighbouring cells, we have performed calculations using the (2×1) supercell approach for nonpolar $\text{ZnO}(10\bar{1}0)$ surfaces and (2×2) supercell for polar $\text{ZnO}(000\bar{1})$ and $\text{ZnO}(0001)$ surfaces. These slab models are schematically represented in **Figure 3.2.1**, omitting partial layers in the middle of surface models. Hereafter, the abbreviation of $\text{Fe}@N$ refers to Fe dopants placed at the substitutional site N .

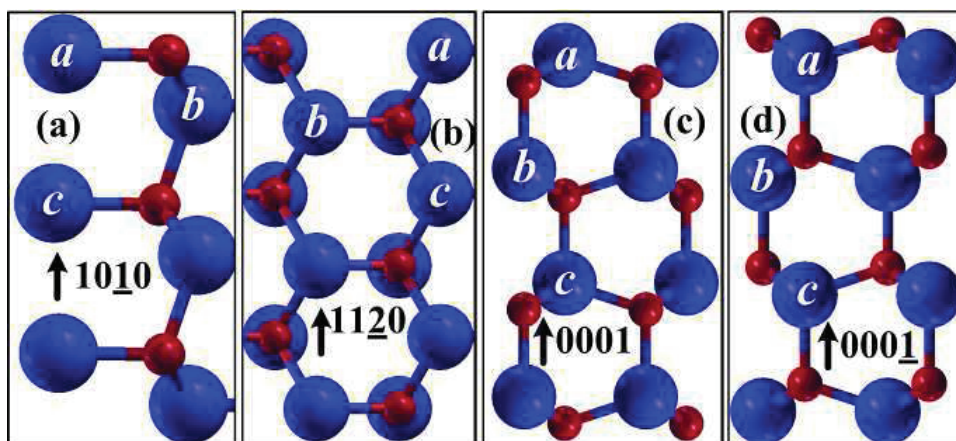


Figure 3.2.1 Side views of schematic surface models (omitting partial layers in the bulk) corresponding to (a) $\text{ZnO}(10\bar{1}0)$, (b) $\text{ZnO}(11\bar{2}0)$, (c) $\text{ZnO}(0001)$, and (d) $\text{ZnO}(000\bar{1})$. blue-zinc, red-oxygen. *a*, *b*, and *c* represent substitutional sites.

Recent investigations have shown that the $\text{ZnO}(0001)$ polar surface is reconstructed with about a quarter of the Zn cations missing from the topmost layer of this surface.^[63] Thus, we have also established corresponding models to investigate zinc vacancies on polar surfaces. Our defective (2×2) polar surface models involve $\frac{1}{4}$ zinc vacancies ($\text{Zn}_{0.75}\text{O}_{1.00}$), as well as, combined cases of $\frac{1}{4}$ zinc vacancies and $\frac{1}{4}$ oxygen vacancies ($\text{Zn}_{0.75}\text{O}_{0.75}$). The corresponding slab models are schematically shown in **Figure 3.2.2**, omitting partial atomic layers in the surface models. The zinc and oxygen vacant sites have been placed in three different layers (see **Figure 3.2.2**).

Furthermore, we have previously demonstrated on the basis of experiments and theory that Fe^{2+} cations prefer to distribute homogeneously inside the ZnO bulk.^[23] Thus, we have also combined polar surface models and the ZnO bulk model with uniform substitutions of Zn lattice sites with Fe^{2+} cations to investigate the charge transfer between two polar surfaces.

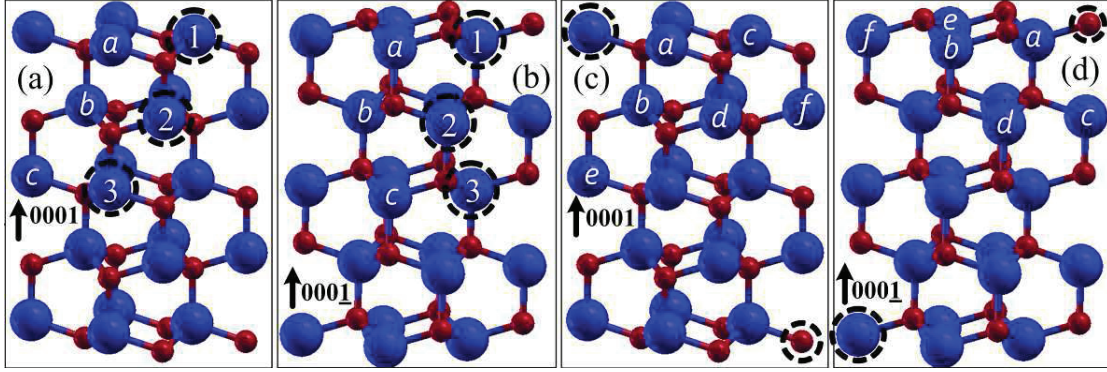


Figure 3.2.2 Schematic side views of defective (2×2) polar surface models, omitting partial intermediate layers: (a) $(\text{Zn}_{0.75}\text{O}_{1.00})-(0001)$, (b) $(\text{Zn}_{0.75}\text{O}_{1.00})-(0001)$, (c) $(\text{Zn}_{0.75}\text{O}_{0.75})-(0001)$, (d) $(\text{Zn}_{0.75}\text{O}_{0.75})-(0001)$. Dashed circles with numbers denote three cases of studied vacant sites, dashed circles without number denote constant vacant sites. Letters represent substitutional sites. blue-zinc and red-oxygen.

Since it is difficult to define a surface energy of the ZnO polar surfaces due to their nonequivalent terminations on two ends, the cleavage energy (energetic difference of ZnO slab models (E_{slab}) with respect to ZnO bulk model (E_{bulk}) with the identical stoichiometry) is well defined and can be directly compared for both polar and nonpolar surfaces (see **Equ. 3.1**). Moreover, the doping energy, as defined in **Equ. 3.2**, compares the stability of Fe-ZnO with respect to pure ZnO:^[64]

$$E_{\text{cleavage}} = E_{\text{slab}} - E_{\text{bulk}} \quad (3.1)$$

$$E_{\text{doping}} = E_{\text{cleavage}(\text{Fe-ZnO})} - E_{\text{cleavage}(\text{ZnO})} \quad (3.2)$$

where $E_{\text{cleavage}(\text{Fe-ZnO})}$ denotes the cleavage energy of the corresponding Fe-ZnO surface models, and $E_{\text{cleavage}(\text{ZnO})}$ refers to the cleavage energy of the corresponding ZnO surface models. We have also performed validation calculations to obtain converged cleavage energies with respect to the thickness of the slab models (ZnO(10 $\bar{1}$ 0): 16 layers, ZnO(11 $\bar{2}$ 0): 12 layers, ZnO(0001) and ZnO(000 $\bar{1}$): 18 layers).

We have performed first-principles DFT calculations using CRYSTAL09 code.^[65] Full geometry optimization of atomic positions and cell parameters was performed for all

models. All-electron basis sets were employed (Zn: 86-411(41d)G,^[66] O: 6-31(1d),^[67] Fe: 86-411(41d)G^[68]) in order to be independent of parameterization of pseudopotentials. The PBE0 hybrid functional was used, as our recent studies have shown that this functional gives better results for Fe-ZnO NPs than other exchange-correlation functionals.

Furthermore, we have also computed X-ray Absorption Near Edge Structure (XANES) to study the oxidation state of Fe dopants on the topmost surface and those placed on sub-surface of the ZnO (000 $\bar{1}$) models. XANES calculations were carried out using FEFF9.0 code^[69] with multiple-scattering scheme, on the basis of optimized geometries from slab models.

TABLE 3.1 Calculated cleavage energies, E_{cleavage} , of perfect ZnO polar and nonpolar surface models and doping energies, E_{doping} , (in $\text{eV } \text{\AA}^{-2}$).

Surface	E_{cleavage}			
	ZnO	Fe@a	Fe@b	Fe@c
(11 $\bar{2}$ 0)	+0.18	+0.05	+0.06	+0.07
(10 $\bar{1}$ 0)	+0.17	+0.08	+0.08	+0.09
(0001)	+0.34	-0.04	-0.04	-0.05
(000 $\bar{1}$)	+0.34	-0.06	-0.08	-0.12

On one hand, the doping energy of Fe@a on ZnO(10 $\bar{1}$ 0) and ZnO(11 $\bar{2}$ 0) surfaces is 0.08 $\text{eV } \text{\AA}^{-2}$ and 0.05 $\text{eV } \text{\AA}^{-2}$, respectively (see **TABLE 3.1**). The calculated doping energies indicate that Fe dopants do not stabilize nonpolar surfaces. This is in agreement with the previous experiments, i.e. that Fe dopants prefer to distribute in the ZnO NP matrix without Fe dopants aggregated on the surfaces of ZnO NPs. On the other hand, the computed doping energies of Fe@a on polar ZnO(000 $\bar{1}$) and ZnO(0001) surfaces are -0.06 $\text{eV } \text{\AA}^{-2}$ and -0.04 $\text{eV } \text{\AA}^{-2}$, respectively. This indicates that the Fe dopants stabilize perfect polar surfaces. Furthermore, the consistent stabilization also occurs on the polar surfaces with an amount of zinc and oxygen vacancies, namely, Fe@a on (Zn_{0.75}O_{1.00})-(0001), Fe@a and Fe@d on (Zn_{0.75}O_{0.75})-(0001), Fe@d and Fe@f on (Zn_{0.75}O_{0.75})-(000 $\bar{1}$) (see **TABLE 3.2**). These results, in-

deed, suggest that stabilization of ZnO polar surfaces, instead of nonpolar surfaces, plays a significant role in experimentally observed reduced dissolution and toxicity of Fe-ZnO NPs.^[23]

TABLE 3.2 Calculated doping energies, E_{doping} , of polar ZnO(000 $\bar{1}$) and ZnO(0001) surfaces with a certain amount of zinc and oxygen vacancies defects ($eV \text{ \AA}^{-2}$).

Surface	E_{doping}		
(Zn _{0.75} O _{1.00})	Fe@a	Fe@b	Fe@c
(0001)	+0.23	+0.23	+0.25
(000 $\bar{1}$)	-0.05	+0.26	+0.23
(Zn _{0.75} O _{0.75})	Fe@a	Fe@b	Fe@c
(0001)	-0.27	+0.65	+0.02
(000 $\bar{1}$)	+0.01	+0.01	+0.01
(Zn _{0.75} O _{0.75})	Fe@d	Fe@e	Fe@f
(0001)	-0.05	+0.02	+0.02
(000 $\bar{1}$)	+0.01	+0.23	-0.07

In spite of limited polar surface area on ZnO NPs, the stabilization of Fe dopants on ZnO polar surfaces is a very critical feature. It stabilizes polar surfaces that are instable facets on pure ZnO NPs. In a nanoparticle, small portions of instable surfaces are always present at edges and vertices, and the stabilization of these surfaces result in the reduced sites where solvent molecules can successfully attack the NP. Stabilizing these surfaces is, therefore, a very important.

In principle, the stabilization of polar surfaces can be achieved by saturating dangling bonds and suppressing the macroscopic dipole moment. Therefore, we have computed XANES to elucidate the oxidation states and also charge density of Fe dopants on ZnO polar surfaces. This information helps to understand the stabilization mechanisms of Fe-ZnO NPs.

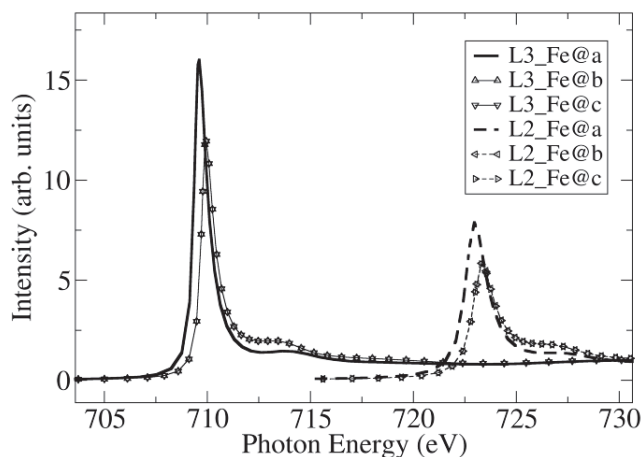


Figure 3.2.3 XANES calculations of Fe L3 and L2 on the ZnO(0001) surface. The L3 edge is represented by solid curves and the L2 edge in dashed curves. Please refer to Figure 3.2.1 for the nomenclature.

We have calibrated oxidation states of Fe with computed XANES of Fe_2O_3 and FeCO_3 in our previous work.^[70] In the present work, XANES calculations reveal that Fe dopants are present in the form of Fe^{3+} on the topmost surface (see **Figure 3.2.3**), while Fe^{2+} dopants are present on the subsurface and bulk of ZnO NPs. The dangling bonds of a pair of zinc and oxygen atoms on the nonpolar surfaces can compensate supersaturated charges. A Fe dopant destroys such a charge balance and reduces the stability of ZnO NPs. Thus, the observed reduced dissolution and toxicity of ZnO NPs is not attributed to nonpolar surfaces.

However, for polar surfaces, Fe^{2+} cation first substitutes for a Zn^{2+} cation on the ZnO(0001) surface and then it can transfer one more d -electron to saturate dangling bonds, forming Fe^{3+} with more stable half filled d -orbital configuration. We have obtained direct evidence of Fe^{3+} that is shown in **Figure 3.2.3**. Thus, the reduced dissolution of ZnO NPs can be contributed from polar surfaces stabilizations. However, the existence of Fe^{3+} cannot cancel the macroscopic dipole moment, where an amount of charge transfer is needed to stabilize the NPs.

The macroscopic dipole moment of ZnO NPs can be described by charge density of layers in the bulk, σ , and that on surfaces, σ' . The dipole moment can be cancelled completely by charge transfer in between two polar surfaces. The ideal charge density of polar

surfaces is $\sigma'=76.5\%\sigma$ to suppress completely the macroscopic dipole moment.^[38] The computed charge density of perfect ZnO polar surfaces is $\sigma'=83.3\%\sigma$, while it can be reduced to $\sigma'=76.1\%\sigma$ in Fe-ZnO. Thus, Fe dopants assisted charge transfer is much closer to the ideal one with respect to the pure ZnO NPs. It is the origin to suppress macroscopic dipole moment and then enhance the overall stability of ZnO polar surfaces.

Electronic structure can be served to interpret the mechanism of Fe dopants assisted charge transfer. The computed O K-edge XANES are shown in **Figure 3.2.4** for the ZnO bulk, Fe-ZnO bulk, perfect Fe-ZnO(000 $\bar{1}$) surface, as well as the defective (Zn_{0.75}O_{1.00})-(000 $\bar{1}$) and (Zn_{0.75}O_{0.75})-(000 $\bar{1}$) surfaces.

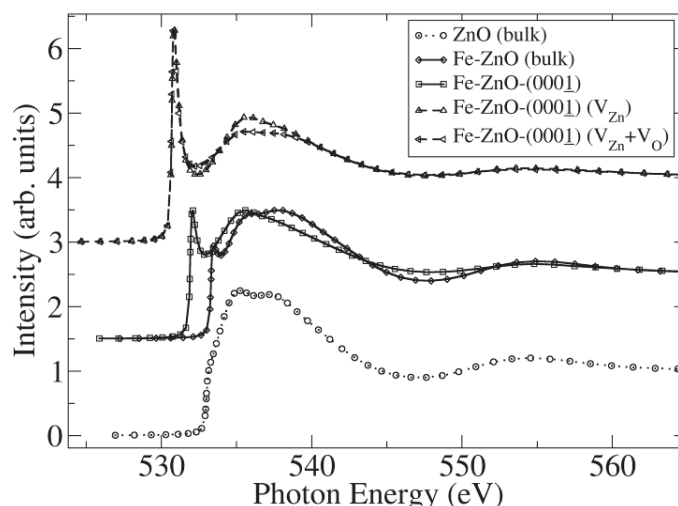


Figure 3.2.4 XANES calculations of O K-edge of ZnO bulk, Fe-doped ZnO bulk, perfect Fe-doped ZnO (000 $\bar{1}$), (Zn_{0.75}O_{1.00})-(000 $\bar{1}$) and (Zn_{0.75}O_{0.75})-(000 $\bar{1}$) surfaces, respectively.

In the Fe-ZnO NPs with mixed valence (Fe³⁺ and Fe²⁺) the Fe-3d orbitals are directly interacting with O-2p orbitals and activate Fe-3d electron hopping to the neighboring Fe cation. This is, indeed, in agreement with the double exchange mechanism proposed by Zener,^[71] where a Fe²⁺-Fe³⁺ pair can facilitate electron hopping in magnetic systems (**Figure 3.2.5**). The pre-edge peak of O K-edge of Fe-ZnO shown in computed XANES is unprecedented electronic state with respect to ZnO (see **Figure 3.2.4**). Comparison between Fe-ZnO and pure ZnO indicates that it is contributed from partially vacant d orbitals, that is, a

result of hybridization between O-2p and Fe-3d orbitals.^[72] The partial charges of oxygen on the topmost layer of ZnO(000 $\bar{1}$) surface are transferred to zinc termination on the ZnO(0001) surface in the opposite end through the hybridized vacant orbitals (see **Figure 3.2.5**). This process can suppress effectively the macroscopic dipole moment and then stabilize polar surfaces indirectly by charge transfer.

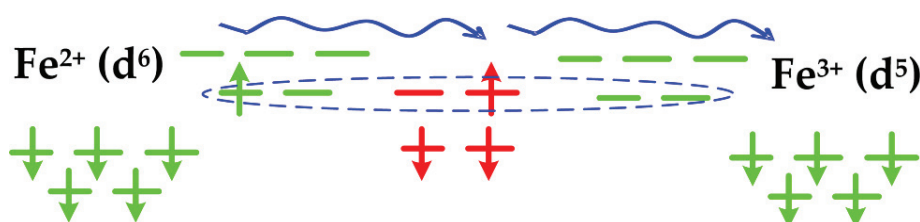


Figure 3.2.5 Schematic representation of the charge transfer assisted by hybridized O-2p and Fe-3d orbitals and double exchange mechanism (Fe²⁺-Fe³⁺ pair).

In summary, we have investigated stability of perfect polar and nonpolar surfaces in ZnO NPs by Fe doping, as well as, defective polar surfaces including $\frac{1}{4}$ zinc and $\frac{1}{4}$ oxygen vacancies. Fe dopants do not stabilize nonpolar surfaces of ZnO NPs, while stabilization occurs only in the case of polar surfaces. It supports the observed reduced dissolution of ZnO NPs. There are two stabilization mechanisms to interpret the above results. On one hand, Fe dopants assisted charge transfer can suppress the macroscopic dipole moment of ZnO NPs. On the other hand, the Fe³⁺ cation, whose existence has been demonstrated with the computed XANES of Fe L3 and L2 edges, can saturate dangling bonds on the ZnO(000 $\bar{1}$) surface and stabilize the NPs.

We have prepared a manuscript to be submitted on the basis of above results and discussion.

Novel Stabilization Mechanism of ZnO Polar Surfaces by Fe doping

J. Xiao, A. Kuc, T. Frauenheim and T. Heine*

My contribution is to prepare these polar and nonpolar surface models, perform geometry optimization and XANES spectra calculations, then analyze stabilization mechanism, finally prepare a preliminary manuscript.

Chapter 4

POLAR SURFACES AND REACTIVITY

4. POLAR SURFACES AND REACTIVITY

As we have analyzed in the previous chapter, the stability of ZnO polar surfaces is correlated with its dissolution, which is very important for intrinsic toxicity of ZnO NPs. In addition, the stability of ZnO polar surfaces can be also correlated with their reactivity. In this chapter, we first discuss the reactivity of α -Fe₂O₃(0001) polar surfaces in comparison with experimental observations. Then, we turn to investigate the reactivity, active sites, and synergy effects of the Cu/ZnO(0001) surface for methanol synthesis under the industrial conditions. Finally, on the basis of the obtained synergy effects, we further proposed an optimized catalyst, namely AgO/ZnO, for CO₂ reduction.

4.1 Active Sites on α -Fe₂O₃(0001) Surfaces

Using in-situ XPS and STM, the signal of adsorbed CO has been detected for the α -Fe₂O₃ nanocrystals size of 6-7 nm. In addition, the adsorbed hydroxyl (OH) groups have been also detected, when exposed to H₂O atmosphere. However, the continuous α -Fe₂O₃ thin film, prepared using the same Au(111) substrate, is inert for H₂O and CO molecules. This reactivity difference can be possibly attributed to crystal edges and the interfaces between the Fe₂O₃ nanocrystals and the Au(111) substrate.^[73]

First, for clean α -Fe₂O₃(0001) surfaces, Wang *et al.*^[74] found two distinct surfaces terminations, namely, Fe-O₃-Fe and O₃-Fe-Fe, shown in **Figure 4.1.1** (We continue to use the nomenclature proposed by Wang *et al.*). The stability of these terminations can be significantly affected by chemical potential of surface oxygen. The proposed stability of these terminations is indeed consistent with the first-principles thermodynamic calculations taking the effects of temperature and pressure into account.^[75]

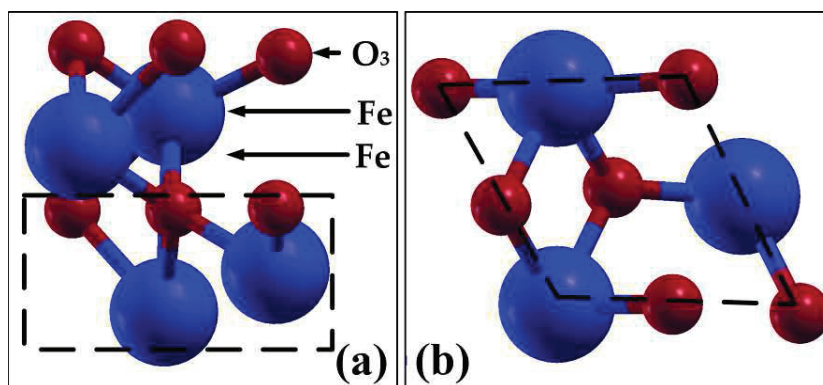


Figure 4.1.1 a) Side view and b) top view of (1×1) oxygen terminated $\alpha\text{-Fe}_2\text{O}_3(0001)$ surface ($\text{O}_3\text{-Fe-Fe}$); Fe: green, O: red. The dashed box represents the replicated unit cell.

Therefore, we have performed calculations to elucidate the different reactivity on the $\alpha\text{-Fe}_2\text{O}_3$ nanocrystals and continuous $\alpha\text{-Fe}_2\text{O}_3$ thin film. The realistic $\alpha\text{-Fe}_2\text{O}_3$ surfaces would exchange adsorbates with their chemical reservoirs. Hence, we have analyzed the Gibbs free energies and their dependence on the chemical potentials of adsorbates. The chemical potential depends on the partial pressure of CO gas, as well as, its surface coverage. We have considered three gradients of CO surface coverage, namely, one third (θ_1), two third (θ_2), and single monolayer (θ_3), based on a (1×1) primitive unit cell. As there are unpaired $3d$ electrons in Fe atoms, we have also considered different spin orderings in our $\alpha\text{-Fe}_2\text{O}_3$ surface models.

Furthermore, first-principles molecular dynamics (MD) simulations were performed to investigate thermal stability of CO-modified surfaces. First of all, we ran a couple of trials (NVE, $T=0\rightarrow 300\text{K}$) to get different initial configurations. Then, we performed calculations with these initial configurations (NVT, $T=300\text{K}$) to equilibrate our systems. The systems were equilibrated within 2 ps with Nosé thermostat and a time step of 2 fs. The MD results are reproducible within random assignments of initial velocities.

We have first found that the $\alpha\text{-Fe}_2\text{O}_3(0001)$ polar surface is reducible, accompanied by CO_2 emission and formation of oxygen vacancy (V_O). In addition, we have also reproduced the experimentally observed hydroxyl and formate groups at the site of V_O . Thus, it turns

out that the V_O is the active site on the $\alpha\text{-Fe}_2\text{O}_3(0001)$ surface. Although the $\alpha\text{-Fe}_2\text{O}_3$ surface is more stable than the $\text{ZnO}(000\bar{1})$ polar surface, the reactivity of $\alpha\text{-Fe}_2\text{O}_3$ polar surface can be improved in a reductive atmosphere of CO gas. It raises an open question whether the $\text{ZnO}(000\bar{1})$ polar surface can be more reactive in a reductive atmosphere.

We have published the above results and analyses as a letter in *App. Phys. Lett.* 101 (2012) 041603.

Activation mechanism of carbon monoxide on $\alpha\text{-Fe}_2\text{O}_3(0001)$ surface studied by using first principle calculations,

*J. Xiao** and T. Frauenheim,

Please refer to the APPENDIX C for detailed results and discussions.

4.2 Synergy Effects on $\text{Cu}/\text{ZnO}(000\bar{1})$ Surfaces

In industry, a typical application of the Cu/ZnO system is the methanol synthesis. However, the chemical reactions on the heterogeneous interface are not well understood. The main challenge to understand a microscopic mechanism of heterogeneous reactions is the identification of the geometry and composition of the catalyst's surfaces. Unfortunately, most experimental techniques in surface science are difficult to be directly performed at a pressure with a magnitude larger than 50 bar and a temperature higher than 500 K. Such conditions are typically used in the industrial process of the methanol synthesis.^[25]

In this work, we first constructed slab models for various $\text{Cu}/\text{ZnO}(000\bar{1})$ surfaces. Then, we employed first-principles thermodynamic calculations to determine the phase diagram of the $\text{Cu}/\text{ZnO}(000\bar{1})$ surfaces under the industrial conditions of temperature and pressure. According to the phase diagram, we found that the reduced $\text{Cu}/\text{ZnO}(000\bar{1})$ surfaces with metallic monolayers, which contain different amount of Cu and Zn atoms, can

be formed and maintain stable. Therefore, CO₂ adsorption was studied thoroughly on these metallic monolayers of all reduced Cu/ZnO(000 $\bar{1}$) surfaces. Calculated projected electronic states of CO₂ adsorbed on these metallic monolayers are analyzed to compare with *d*-band model. Finally, we investigated the CO₂ reduction on these surfaces. The results indicate that these surfaces are indeed more favorable for CO₂ reduction in comparison with reported surfaces from available literature, *e.g.*, Cu(100) and CuZn(211). This behavior is also quite reasonably interpreted with the *d*-band model. Thus, we have found two important synergy effects between the metallic monolayers and their support, namely the ZnO(000 $\bar{1}$) surface.

Our proposed surfaces were, however, not directly observed in the high-resolution transmission electron microscopy (HRTEM).^[76] This is because the HRTEM measurements were performed under conventional vacuum conditions, instead of the condition with a gaseous H₂ and CO₂ atmosphere. Therefore, these surfaces that we proposed are definitely reconstructed under vacuum conditions. According to the above analyses, the CO₂ reduction is, indeed, feasible on the polar surface of Cu/ZnO-based catalysts. The critical issue is to activate the Cu/ZnO(000 $\bar{1}$) surface before its industrial application.

We have published a letter in *J. Phys. Chem. Lett.* **2012**, 3, 2638-2642.

Activity and Synergy Effects on a Cu/ZnO(000 $\bar{1}$) Surface Studied

Using First-Principle Thermodynamics,

J. Xiao and T. Frauenheim,*

Please refer to the APPENDIX D for detailed results and discussions.

4.3 CO₂ Reduction on Ag/ZnO(0001) Surfaces

Although the Cu/ZnO(0001) surface seems to be an appropriate catalyst for CO₂ reduction, we are not able to activate this surface without the atmosphere of CO gas. We still need to design a better catalyst for CO₂ reduction.

Over the past several decades, our understanding why particular catalysts are good for specific reactions has been improved. Current challenge is to answer the inverted problem: given that we need to catalyze a certain reaction under a number of specified conditions, which material should we choose? Theoretical descriptors are becoming more and more important for computational design of catalysts. Therefore, the *d*-band model was developed and served as an important descriptor for understanding and predicting the reactivity of catalysts.

In the group IB of periodic table, a close-packed Ag(111) surface possesses the deepest-lying *d*-band states of -4.30 eV with respect to its Fermi level, while the *d*-band centers of Cu(-2.67) and Au(-3.56) are closer to their Fermi levels. In addition, thanks to a small adsorbate-metal *d*-coupling matrix element between the Ag(111) surface and certain adsorbates, *e.g.*, carbon and nitrogen, it results in the extremely noble Ag(111) surface. Therefore, activating the Ag(111) surface could provide valuable information to improve the reactivity of other noble metals.

We have first studied the CO₂ adsorption on the pristine Ag(111) surface as a reference. Meanwhile, the CO₂ activity on the Ag(111) surface subject to a tensile strain of 14% was investigated, as well. The calculated *d*-band states of the stretched Ag(111) surface are shown to be shifted slightly upward. The CO₂ activity on the stretched Ag(111) surface is similar to that on the pristine materials. Then, we made further investigations with the Ag(111) surfaces of the same tensile strain supported on a ZnO(0001) substrate. To understand the extension of the SMSI effect, we have considered trilayers, bilayers, and monolayer of the Ag(111) surface supported on the same ZnO(0001) substrate.

On one hand, we found that the *m*-Ag/ZnO surface have an intermediate binding ability towards CO₂ molecules. Calculated results indicate that this surface can serve as a catalyst for the subsequent CO₂ reduction. On the other hand, in order to obtain an optimized efficiency of Ag utilization, we turn to investigate the stability of the Ag-doped ZnO(000 $\bar{1}$) surface, that is, the precursor of the *m*-Ag/ZnO surface, under H₂-rich conditions, as well as, this surface with a certain amount of Zn impurities.

The results show the reactivity of the *m*-Ag/ZnO surface to be quite steady in the presence of Zn impurities. This result can further inspire us to propose a strategy to optimize the efficiency of Ag utilization, as well as, more practical operations in the experiments.

We have published an article in J. Phys. Chem. C **2013** (117) 1804-1808.

Theoretical insights into CO₂ activation and reduction on the Ag(111) monolayer supported on a ZnO(000 $\bar{1}$) substrate,

J. Xiao and T. Frauenheim,*

Please refer to the APPENDIX E for detailed results and analyses.

Chapter 5

CONCLUSIONS

5. CONCLUSIONS

5.1 Polar Surfaces and Stability

In the ZnO bulk, Fe dopants were found to be Fe²⁺ from our XANES calculations, in a good agreement with the experimental ISEELS spectra. Since the Fe²⁺ dopants are compressed in the ZnO wurtzite lattice with respect to FeO in rocksalt phase, the local charge of Fe²⁺ is close to that of Fe³⁺ of Fe₂O₃ in corundum phase, determined by Mößbauer measurements and DFT calculations. It clarifies the stabilization mechanism of ZnO bulk by Fe doping.

In contrast to ZnO bulk, our simulations indicate that only the ZnO polar surfaces are stabilized by Fe dopants, which implies that the reduced ZnO dissolution is due to the stabilization of polar surfaces. In addition, it was found that Fe³⁺, instead of Fe²⁺, prefers to be on the ZnO(0001) surface. Moreover, the Fe²⁺-Fe³⁺ pairs can efficiently improve charge transfer in-between two ZnO polar surfaces. In short, the observed reduced toxicity of ZnO NPs can be attributable to the stabilization of ZnO polar surfaces.

5.2 Polar Surfaces and Reactivity

In the case of Cu/ZnO catalysts, Cu dopants can destabilize the ZnO(0001) surface, accompanied by metallic monolayers formation. The metallic monolayers are automatically supported by the ZnO(0001) surface. Moreover, the *d*-band states of the monolayers are quite improved and the reactivity is also optimized for the subsequent CO₂ hydrogenation. Therefore, this is an important synergy effect at the Cu/ZnO(0001) interface. However, the atmosphere of CO gas is necessary to activate this surface. We need further studies to quest an optimized catalyst for CO₂ reduction.

According to the obtained synergy effects in the case of Cu/ZnO(0001), we have performed systematic calculations to improve the reactivity of the pristine Ag/ZnO(0001) surface, concerning stretched Ag(111) surfaces and Ag(111) layers supported by the ZnO(0001) surface. It has been found that the Ag(111) monolayer supported by the ZnO(0001) surface has optimized reactivity for CO₂ adsorption and subsequent reduction. Further calculations indicate that the AgO/ZnO NPs can serve as a precursor of this catalyst. Therefore, we were able to propose a strategy to obtain an optimized catalyst for CO₂ reduction, which is also quite feasible in practice.

REFERENCES

-
- [1] V. H. Grassian, *Nanoscience and Nanotechnology Environmental and Health Impacts*. Wiley, 2008.
- [2] R. F. Service, Nanotechnology Crows Up. *Science* 304 (2004) 1732-1734.
- [3] A. Nel, T. Xia, L. Mädler, and N. Li, Toxic Potential of Materials at the Nanolevel. *Science* 311 (2006) 622-627.
- [4] V. L. Colvin, The Potential Environmental Impact of Engineered Nanomaterials. *Nature Biotechnology* 21 (2003) 1166-1170.
- [5] K. Donaldson, V. Stone, C. L. Tran, W. Kreyling, and P. J. A. Borm, Nanotoxicology, *Occup. Environ. Med.* 113 (2005) 727-728.
- [6] G. Oberdörster, E. Oberdörster, J. Oberdörster, Nanotoxicology: An Emerging Discipline Evolving From Studies of Ultrafine Particles, *Environ. Health. Perspect.* 113 (2005) 823-839.
- [7] A. Nel, Air Pollution-Related Illness: Effects of Particles, *Science* 308 (2005) 804-806.
- [8] T. Cedervall, I. Lynch, S. Lindman, T. Berggård, E. Thulin, H. Nilsson, K. A. Dawson, S. Linse, Understanding the Nanoparticle-Protein Corona Using Methods to Quantify Exchange Rates and Affinities of Proteins for Nanoparticles, *Proc. Natl. Acad. Sci. USA* 104 (2007) 2050-2055.
- [9] A. A. Vertegel, R. W. Siegel, J. S. Dordick, Silica Nanoparticle Size Influences the Structure and Enzymatic Activity of Adsorbed Lysozyme. *Langmuir* 20 (2004) 6800-6807.
- [10] (a) K. Ueda, H. Tabata, T. Kawai, Magnetic and Electric Properties of Transition-Metal-Doped ZnO films, *Appl. Phys. Lett.* 79 (2001) 79-81. (b) P. V. Kamat, Photophysical, Photochemical and Photocatalytic Aspects of Metal Nanoparticles, *J. Phys. Chem. B* 106 (2002) 7729-7744. (c) C. Soci, A. Zhang, B. Xiang, S. A. Dayeh, D. P. R. Aplin, J. Park, X. Y. Bao, Y. H. Lo, D. Wang, ZnO Nanowire UV Photodetectors with High Internal Gain, *Nano Lett.* 7 (2007) 1003-1009. (d) J. P. Richters, T. Voss, L. Wischmeier, L. Rüdchmann, J. Gutowski, Influence of Polymer Coating on the Low-Temperature Photoluminescence Properties of ZnO Nanowires, *Appl. Phys. Lett.* 92 (2008) 011103-3.
- [11] (a) M. Law, L. E. Greene, J. C. Johnson, R. Saykally, P. Yang, Nanowire Dye-sensitized Solar Cells, *Nat. Mater.* 4 (2005) 455-459. (b) Y. Li, W. Meng, L. D. Zhang, F. Phillipp, Ordered Semicon-

ductor ZnO Nanowires Arrays and Their Photoluminescence Properties, *Appl. Phys. Lett.* 76 (2000), 2011-2013. (c) X. Wang, J. Song, P. Li, J. H. Ryou, R. D. Dupuis, C. J. Summers, Z. L. Wang, Growth of Uniformly Aligned ZnO Nanowire Heterojunction Arrays on GaN, AlN, and Al_{0.5}Ga_{0.5}N Substrates, *J. Am. Chem. Soc.* 127 (2005) 7920-7923.

[12] (a) W. L. Hughes, Z. L. Wang, Controlled Synthesis and Manipulation of ZnO Nanorings and Nanobows, *Appl. Phys. Lett.* 86 (2005) 043106. (b) X. Wen, Y. Fang, Q. Fang, C. Yang, J. Wang, W. Ge, K. S. Wong, S. Yang, ZnO Nanobelt Arrays Grown Directly from and on Zinc Substrates: Synthesis, Characterization and Applications, *J. Phys. Chem. B* 109 (2005) 15303-15308. (c) Z. W. Pan, Z. R. Dai, Z. L. Wang, Nanobelts of Semiconducting Oxides, *Science*, 291 (2001) 1947-1949.

[13] (a) X. Y. Xu, H. Z. Zhang, Q. Zhao, Y. F. Chen, J. Xu, D. P. Yu, Patterned Growth of ZnO Nanorod Arrays on a Large-Area Stainless Steel Grid, *J. Phys. Chem. B* 109 (2005), 1699-1702. (b) Z. R. Tian, J. A. Vogit, J. Liu, B. Mckenzie, M. J. Mcdermott, Biomimetic Arrays of Oriented Helical ZnO Nanorods and Columns, *J. Am. Chem. Soc.* 124 (2002) 12954-12955.

[14] Z. L. Wang, Zinc Oxide Nanostructures: Growth, Properties and Applications, *J. Phys: Condens. Matter* 16 (2004) 829-858.

[15] P. X. Gao, Y. Ding, W. Mai, W. L. Hughes, C. Lao, Z. L. Wang, Conversion of Zinc Oxide Nanobelts into Superlattice-Structured Nanohelices, *Science* 309 (2005) 1700-1704.

[16] (a) S. Guo, S. Dong, Biomolecule-Nanoparticle Hybrids for Electrochemical Biosensors, *Trends Anal. Chem.* 28 (2009) 96-109. (b) S. P. Singh, S. K. Arya, P. Pandey, B. D. Malhotra, S. Saha, K. Sreenivas, V. Gupta, Cholesterol Biosensor Based on rf Sputtered Zinc Oxide Nanoporous Thin Film, *Appl. Phys. Lett.* 91 (2007) 063901.

[17] T. Xia, M. Kovoichich, M. Liong, L. Mädler, B. Gilbert, H. Shi, J. I. Yeh, J. I. Zink, A. E. Nel, Comparison of the Mechanism of Toxicity of Zinc Oxide and Cerium Oxide Nanoparticles Based on Dissolution and Oxidative Stress Properties, *ACS nano* 2 (2008), 2121-2134.

[18] P. J. Moos, K. Chung, D. Woessner, M. Honegger, N. S. Cutler, J. M. Veranth, ZnO Particulate Matter Requires Cell Contact for Toxicity in Human Colon Cancer Cells, *Chem. Res. Toxicol* 23 (2010), 733-739.

[19] M. Mortimer, K. Kasemets, A. Kahru, Toxicity of ZnO and CuO Nanoparticles to Ciliated Protozoa Tetrahymena Thermophila, *Toxicology* 269 (2010), 182-189.

- [20] I. L. Hsiao, Y. J. Huang, Effects of Various Physicochemical Characteristics on the Toxicities of ZnO and TiO₂ Nanoparticles toward Human Lung Epithelial Cells, *Sci. Total Environ.* 409 (2011) 1219-1228.
- [21] J. E. Canas, B. B. Qi, S.B. Li, J. D. Maul, S. B. Cox, S. Das, M. J. Green, Acute and Reproductive Toxicity of Nano-sized Metal Oxides (ZnO and TiO₂) to Earthworms (*Eisenia fetida*), *J. Environ. Monitor.* 13 (2011) 3351-3357.
- [22] C. R. Thomas, S. George, A. M. Horst, Z. Ji, R. J. Miller, J. R. Peralta-Videa, T. Xia, S. Pokhrel, L. Mädler, J. L. Gardea-Torredey, P. A. Holden, A. A. Keller, H. S. Lenihan, A. E. Nel, J. I. Zink, Nanomaterials in the Environment: From Materials to High-Throughput Screening to Organisms, *ACS nano* 5 (2011) 13-20.
- [23] S. George, S. Pokhrel, T. Xia, B. Gilbert, Z. Ji, M. Schowalter, A. Rosenauer, R. Damoiseaux, K. A. Bradley, L. Mädler, A. E. Nel, Use of a Rapid Cytotoxicity Screening Approach to Engineer a Safer Zinc Oxide Nanoparticle Through Iron Doping, *ACS nano* 4 (2010) 15-29.
- [24] T. Xia, Y. Zhao, T. Sager, S. George, S. Pokhrel, N. Li, D. Schoenfeld, H. Meng, S. Lin, X. Wang, M. Wang, Z. Ji, J. I. Zink, L. Mädler, V. Castranova, S. Lin, A. E. Nel, Decreased Dissolution of ZnO by Iron doping Yields Nanoparticles with Reduced Toxicity in the Rodent Lung and Zebrafish Embryos, *ACS nano* 2 (2011), 1223-1235.
- [25] S. Lee, Methanol Synthesis Technology. CRC Press: Boca Raton, FL, 1989.
- [26] Klier, Methanol Synthesis. *Adv. Catal.* 31, (1982) 243-313.
- [27] G. C. Chinchin, K. C. Waugh, D. A. Whan, The Activity and State of the Copper Surface in Methanol Synthesis Catalysts. *Appl. Catal.* 25, (1986) 101-107.
- [28] C. Liu, T. R. Cundari, A. K. Wilson, CO₂ Reduction on Transition Metal (Fe, Co, Ni, and Cu) Surfaces: In Comparison with Homogeneous Catalysis. *J. Phys. Chem. C.* 116 (2012) 5681-5688.
- [29] M. Behrens, F. Studt, I. Kasatkin, S. Kuhl, M. Havecker, F. A. Pedersen, S. Zander, F. Girgsdies, P. Kurr, B. L. Kniep, M. Tovar, R. W. Fischer, J. K. Nørskov, R. Schlogl, The Active Site of Methanol Synthesis over Cu/ZnO/Al₂O₃ Industrial Catalysts, *Science*, 336 (2012), 893-897.
- [30] (a) S. J. Tauster, Strong Metal-Support Interactions, *Acc. Chem. Res.* 20 (1987) 389-394. (b) G. L. Haller, D. E. Resasco, Metal-Support Interaction: Group VIII Metals and Reducible Oxides, *Adv.*

-
- Catal.* 36 (1989), 173-235. (c) M. S. Chen, D. W. Goodman, The Structure of Catalytically Active Gold on Titania. *Science* 306 (2004), 252-255. (d) Q. Fu, T. Wagner, Interaction of Nanostructured Metal Overlayers with Oxide Surface. *Surf. Sci. Rep.* 62 (2007) 431-498.
- [31] Christof Wöll, The Chemistry and Physics of Zinc Oxide Surfaces, *Prog. Surf. Sci.* 82 (2007), 55-120.
- [32] P. W. Tasker, the Stability of Ionic Crystal Surfaces, *J. Phys. C: Solid State Phys.* 12 (1979) 4977-4984.
- [33] C. Noguera, Polar Oxide Surfaces, *J. of Phys.:Condens. Matter* 12 (2000) R367-R410.
- [34] (a) S. H. Overbury, P. V. Radulovic, S. Thevuthasan, G. S. Herman, M. A. Henderson, C. H. F. Peden, Ion Scattering Study of The Zn and Oxygen-terminated Basal Plane Surfaces of ZnO, *Surface Science*, 410 (1998) 106-122. (b) N. Jedrecy, S. Gallini, M. Sauvage-Simkin, R. Pinchaux, Copper Growth on the O-terminated ZnO(000 $\bar{1}$) Surface: Structure And Morphology, *Phys. Rev. B* 64 (2001) 085424.
- [35] (a) A. Wander, F. Schedin, P. Steadman, A. Norris, R. McGrath, T.S. Turner, G. Thornton, N.M. Harrison, Stability of Polar Oxide Surfaces, *Phys. Rev. Lett.* 86 (2001) 3811-3814. (b) C.B. Duke, A.R. Lubinsky, Calculations of Low-Energy Electron Diffraction Intensities from the Polar Faces of Zinc Oxide, *Surf. Sci.* 50 (1975) 605-614. (c) N. Jedrecy, S. Gallini, M.Sauvage-Simkin, R. Pinchaux, Copper Growth on the O-terminated ZnO(000 $\bar{1}$) Surface: Structure and Morphology, *Phys. Rev. B* 64 (2001) 085424.
- [36] O. Dulub, U. Diebold, G. Kresse, Novel Stabilization Mechanism on Polar Surfaces: ZnO(0001)-Zn, *Phys. Rev. Lett.* 90 (2003) 016102.
- [37] M. Kunat, S. Gil-Girol, T. Becker, U. Burghaus, C. Wöll, The Stability of the Polar Surfaces of ZnO: a Reinvestigation Using He-atom Scattering, *Phys. Rev. B* 66 (2002) 081402
- [38] A. Wander, F. Schedin, P. Steadman, A. Norris, R. McGrath, T. S. Turner, G. Thornton, N. M. Harrison, Stability of Polar Oxide Surfaces, *Phys. Rev. Lett.* 86 (2001) 3811-3814.
- [39] E. Schrödinger, An Undulatory Theory of the Mechanics of Atoms and Molecules, *Phys. Rev.* 28 (1926) 1049-1070.

-
- [40] K. T. Wikfeldt, Structure, Dynamics and Thermodynamics of Liquid Water: Insights from Molecular Simulations. PhD diss. Stockholm University, **2011**.
- [41] M. Born, J. R. Oppenheimer, Zur Quantentheorie der Molekeln, *Ann. Phys.* 84 (1927) 457-487.
- [42] D. S. Sholl, J. A. Steckel, *Density Functional Theory: A Practical Introduction*, Wiley-interscience, New Jersey, **2009**.
- [43] T. Heine, J. O. Joswig, A. Gelessus, Computational Chemistry Workbook: Learning Through Examples, *Wiley-VCH*, **2009**.
- [44] P. Hohenberg, W. Kohn, Inhomogeneous Electron Gas, *Rhys. Rev.* 136 (1964) B864-B871.
- [45] W. Kohn, L. J. Sham. Self-Consistent Equations Including Exchange and Correlation Effects, *Phys. Rev.* 140 (1965) A1133-A1138.
- [46] R. G. Parr, W. Yang, Density Functional Theory of Atoms and Molecules. Oxford: Oxford University Press, **1994**.
- [47] D. C. Langreth, J. P. Perdew, Theory of Nonuniform Electronic Systems. I. Analysis of the Gradient Approximation and a Generalization That Works, *Phys. Rev. B* 21 (1980) 5469.
- [48] J. P. Perdew, Y. Wang, Accurate and Simple Density Functional for Electronic Exchange Energy: Generalized Gradient Approximation, *Phys. Rev. B* 33 (1986) 8800-8802.
- [49] J. P. Perdew, K. Burke, M. Ernzerhof, Generalized Gradient Approximation Made Simple, *Phys. Rev. Lett.* 77 (1996) 3865-3868.
- [50] A. Szabo, N. S. Ostlund, Modern Quantum Chemistry: Introduction to Advanced Electronic Structure Theory. *Dover publication*, Dover, **1996**.
- [51] C. Adamo, V. Barone, Toward Chemical Accuracy in the Computation of NMR Shielding: the PBE0 Model. *Chem. Phys. Lett.* 298 (1998) 113-119.
- [52] J. Heyd, G. E. Scuseria, M. Ernzerhof, Hybrid Functional Based on a Screened Coulomb Potential. *J. Chem. Phys.* 118 (2003) 8207-8215.
- [53] J. C. Slater, K. H. Johnson, Self-Consistent-Field $X\alpha$ Cluster Method for Polyatomic Molecules and Solids, *Phys. Rev. B* 5 (1972) 844-853.

-
- [54] J. J. Rehr, R. C. Albers, Theoretical Approaches to X-ray Absorption Fine Structure, *Rev. Mod. Phys.* 72 (2000) 621-654.
- [55] J. C. Slater, Wave Functions in a Periodic Potential, *Phys. Rev.* 51 (1937) 846-851.
- [56] E. Kuzmann, S. Nagy, A. Vértes, Critical Review of Analytical Application of Mößbauer Spectroscopy Illustrated by Mineralogical and Geological Examples, *Pure Appl. Chem.* 75 (2003) 801-858.
- [57] M. D. Dyar, D. G. Agresti, M. W. Schaefer, C. A. Grant, E. C. Sklute, Mößbauer Spectroscopy of Earth and Planetary Materials, *Annu. Rev. Earth Planet. Sci.* 34 (2006) 83-125.
- [58] P. Blaha, Calculations of Mößbauer Parameters in Solids by DFT Bandstructure Calculations, *J. Phys.: Conf. Ser.* 217 (2009) 012009.
- [59] U. D. Wdowik, K. Ruebenbauer, Calibration of the Isomer Shift for the 14.4-keV Transition in ^{57}Fe Using the Full-Potential Linearized Augmented Plane-Wave Method, *Phys. Rev. B* 76 (2007) 155118.
- [60] K. J. Duff, Calibration of the Isomer Shift for ^{57}Fe , *Phys. Rev. B* 9 (1974) 66-72.
- [61] A. M. Mudarra Navarro, C. E. R. Torres, L. A. Errico, Calibration of the Isomer Shift of the 14.4 keV Transition of ^{57}Fe , *Hyperfine Interact.* 202 (2011) 117-121.
- [62] P. Dufek, P. Blaha, K. Schwarz, Determination of the Nuclear Quadrupole Moment of ^{57}Fe , *Phys. Rev. Lett.* 75 (1995) 3545-3548.
- [63] (a) N. Jedrecy, M. Sauvage-Simkin, P. Pinchaux, The Hexagonal Polar ZnO(0001)-(1×1) Surfaces: Structural Features as Stemming from X-ray diffraction, *Appl. Surf. Sci.* 162-163 (2000) 69-73.
(b) M. Kunat, S. G. Girol, Th. Becker, U. Burghaus and Ch. Wöll, Stability of the Polar Surfaces of ZnO: A Reinvestigation Using He-atom Scattering, *Phys. Rev. B* 66 (2002) 081402.
- [64] B. Meyer, D. Marx. Density-Functional Study of the Structure and Stability of ZnO surfaces, *Phys. Rev. B* 67 (2003) 035403.
- [65] R. Dovesi, V.R. Saunders, C. Roetti, R. Orlando, C. M. Zicovich-Wilson, F. Pascale, B. Civalleri, K. Doll, N.M. Harrison, I.J. Bush, Ph. D'Arco, M. Llunell, CRYSTAL09 User's Manual, (2009) University of Torino, Torino.

-
- [66] J. E. Jaffe and A. C. Hess, Hartree-Fock Study of Phase Changes in ZnO at High Pressure, *Phys. Rev. B* 48 (1993) 7903-7909.
- [67] C. Gatti, V. R. Saunders, C. Roetti, Crystal Field Effects on the Topological Properties of the Electron Density in Molecular Crystals: The Case of Urea, *J. Chem. Phys.* 101 (1994) 10686-10696.
- [68] G. Valerio, M. Catti, R. Dovesi and R. Orlando, Ab Initio Study of Antiferromagnetic Rutile-Type FeF₂, *Phys. Rev. B* 52 (1995) 2422-2427.
- [69] A. L. Ankudinov, B. Ravel, J. J. Rehr and S. D. Conradson. Real-Space Multiple-Scattering Calculation and Interpretation of X-Ray-Absorption Near-Edge Structure, *Phys. Rev. B.* 58, 7565 (1998).
- [70] J. Xiao, A. Kuc, S. Pokhrel, M. Schowalter, S. Porlapalli, A. Rosenauer, T. Frauenheim, L. Mädler, L. G.M. Pettersson, T. Heine. Evidence for Fe²⁺ in Wurtzite Coordination: Iron Doping Stabilizes ZnO Nanoparticles, *Small* 7 (2011) 2879–2886.
- [71] C. Zener, Interaction between the *d*-Shells in the Transition Metals. II. Ferromagnetic Compounds of Manganese with Perovskite Structure, *Phys. Rev. Lett.* 82 (1951) 403-405
- [72] (a) Y. Chueh, M. Lai, J. Liang, L. Chou, Z. Wang, Systematic Study of the Growth of Aligned Arrays of α -Fe₂O₃ and Fe₃O₄ Nanowires by a Vapor–Solid Process, *Adv. Funct. Mater.* 16 (2006) 2243-2251. (b) Y. Lee, Y. Chuen, C. Hsieh, M. Chang, L. Chou, Z. Wang, Y. Lan, C. Chen, H. Kurata, S. Isoda. p-Type α -Fe₂O₃ Nanowires and their n-Type Transition in a Reductive Ambient, *small* 8 (2007) 1356-1361.
- [73] X. Deng, J. Lee, C. Wang, C. Matranga, F. Aksoy, Z. Liu, Reactivity Difference of Nanocrystals and Continuous Films of α -Fe₂O₃ on Au(111) Studied with in situ X-ray Photoelectron Spectroscopy, *J. Phys. Chem. C* 114 (2010) 22619-22623.
- [74] X.-G. Wang, W. Weiss, Sh. K. Shaikhutdinov, M. Ritter, M. Petersen, F. Wagner, R. Schlögl, M. Scheffler, The Hematite (α -Fe₂O₃) (0001) Surface: Evidence for Domains of Distinct Chemistry, *Phys. Rev. Lett.* 81, (1998) 1038-1041.
- [75] W. Bergermayer, H. Schweiger, *Ab Initio* Thermodynamics of Oxide Surfaces: O₂ on α -Fe₂O₃(0001), *Phys. Rev. B* 69 (2004) 195409.

- [76] M. Behrens, F. Studt, I. Kasatkin, S. Kühl, M. Hävecker, F. A. Pedersen, S. Zander, F. Girgsdies, P. Kurr, B. L. Kniep, M. Tovar, R. W. Fischer, J. K. Nørskov, R. Schlögl, The Active Site of Methanol Synthesis over Cu/ZnO/Al₂O₃ Industrial Catalysts, *Science* 336 (2012) 893–897.

APPENDICES

APPENDIX A:

Evidence for Fe²⁺ in Wurtzite Coordination: Iron Doping Stabilizes ZnO Nanoparticles, (Small, 2011 (7), 2879–2886)

J. Xiao, A. Kuc, S. Pokhrel, M. Schowalter, S. Porlapalli, A. Rosenauer, T. Frauenheim, L. Mädler, L.G.M. Pettersson, T. Heine,*

My contribution is to build up atomistic models, optimize structures, calculate formation energies and core-level spectra, and prepare a preliminary manuscript.

APPENDIX B:

Fe-doped ZnO Nanoparticles: The iron oxidation number and local charge studied by ⁵⁷Fe Mößbauer spectroscopy and DFT, (Chem. Eur. J, 2013 (19), 3287-3291).

*J. Xiao, A. Kuc, S. Pokhrel, L. Mädler, R. Pöttgen, F. Winter, T. Frauenheim and T. Heine**

My contribution is to use these atomistic models in the previous work and build up more hydrogen saturated models, and then perform optimization and analyze Fe-3d orbitals occupancy, calculate IS and QS values of Mößbauer spectroscopy, make Bader charge population analysis, and prepare a preliminary manuscript.

APPENDIX C:

Activation mechanism of carbon monoxide on α -Fe₂O₃(0001) surface studied by using first principle calculations, (App. Phys. Lett. 2012 (101), 041603).

J. Xiao and T. Frauenheim,*

My contribution is to build up these slab models, perform static DFT calculations and analyze thermal stability of adsorbate using MD simulation, and analyze the active sites of α -Fe₂O₃(0001) surface. Finally, I wrote the paper and was corresponding to the submission of this letter.

APPENDIX D:

Activity and Synergy Effects on a Cu/ZnO(0001) Surface Studied Using First-Principle Thermodynamics. (J. Phys. Chem. Lett. 2012 (3), 2638-2642).

J. Xiao and T. Frauenheim,*

My contribution is to establish all models, then perform DFT calculations and analyze the synergy effects, and perform calculations to analyze the activity of CO₂ adsorption and reduction on the Cu/ZnO(0001) surface. Finally, I was writing the letter and corresponding to the submission.

APPENDIX E:

Theoretical insights into CO₂ activation and reduction on the Ag(111) monolayer supported on a ZnO(0001) substrate. (J. Phys. Chem. C 2013 (117) 1804-1808)

J. Xiao and T. Frauenheim,*

My contribution is to establish these theoretical models, perform calculations and analyze the d-band evolution for all models, and then calculate CO₂ adsorption and reduction on these Ag/ZnO(0001) surfaces. Finally, I prepared the preliminary manuscript.

APPENDIX A:

Evidence for Fe²⁺ in Wurtzite Coordination: Iron Doping Stabilizes ZnO Nanoparticles,

Small, 2011 (7), 2879–2886,

J. Xiao, A. Kuc, S. Pokhrel, M. Schowalter, S. Porlapalli, A. Rosenauer, T.

Frauenheim, L. Mädler, L.G.M. Pettersson, T. Heine,*

NANO || MICRO

small

Doped Nanoparticles

Zinc oxide nanoparticles can be stabilized by substitutional addition of iron, where up to 10% Fe^{2+} replace Zn^{2+} ions. The picture shows the transmission electron microscope image of a Fe-doped ZnO nanoparticle, decorated with the representation of the atomic positions of a computer simulation (Fe: yellow, Zn: blue, O: red). The samples have been characterized by TEM, PXRD, and ISEELS, and detailed density functional calculations confirm experimental observations: Fe ions stabilize the structure, the structural characteristics of the Fe-doped ZnO nanoparticles remain essentially unchanged, and comparison of experimental and simulated core-shell spectroscopy data exclude significant amounts of Fe^{3+} in the samples.

20/2011

WileyVCH

Evidence for Fe^{2+} in Wurtzite Coordination: Iron Doping Stabilizes ZnO Nanoparticles

T. Heine et al.

Evidence for Fe²⁺ in Wurtzite Coordination: Iron Doping Stabilizes ZnO Nanoparticles

Jianping Xiao, Agnieszka Kuc, Suman Pokhrel, Marco Schowalter, Satyam Parlapalli, Andreas Rosenauer, Thomas Frauenheim, Lutz Mädler, Lars G. M. Pettersson, and Thomas Heine*

First-principles calculations are used to investigate the structural and electronic properties of Fe-doped ZnO nanoparticles. Based on extensive validation studies surveying various density functionals, the hybrid functional PBE0 is employed to calculate the structures, formation energies, and electronic properties of Fe in ZnO with Fe concentrations of 6.25, 12.5, and 18.75 at%. Substitution of Zn by Fe, zinc vacancies, and interstitial oxygen defects is studied. High-resolution inner-shell electron energy loss spectroscopy measurements and X-ray absorption near-edge structure calculations of Fe and O atoms are performed. The results show that Fe-doped ZnO nanoparticles are structurally and energetically more stable than the isolated FeO (rocksalt) and ZnO (wurtzite) phases. The Fe dopants distribute homogeneously in ZnO nanoparticles and do not significantly alter the host ZnO lattice parameters. Simulations of the absorption spectra demonstrate that Fe²⁺ dominates in the Fe-doped ZnO nanoparticles reported recently, whereas Fe³⁺ is present only as a trace.

J. Xiao, Dr. A. Kuc, Prof. T. Heine
School of Engineering and Science
Jacobs University Bremen
Campus Ring 1, 28759 Bremen, Germany
E-mail: t.heine@jacobs-university.de

J. Xiao, Prof. T. Frauenheim
Bremen Center for Computational Materials Science
Universität Bremen
Am Fallturm 1, 28359 Bremen, Germany
Dr. S. Pokhrel, Prof. L. Mädler
IWT Foundation Institute of Materials Science
Department of Production Engineering
Universität Bremen
Bremen 28359, Germany

Dr. M. Schowalter, S. Parlapalli, Prof. A. Rosenauer
Institute for Solid State Physics
Universität Bremen
28359 Bremen, Germany

Prof. L. G. M. Pettersson
Department of Physics
AlbaNova University Center
Stockholm University
10691 Stockholm, Sweden

DOI: 10.1002/sml.201100963

1. Introduction

Zinc oxide (ZnO) is a very important multifunctional material, which can potentially be utilized in electronics,^[1] optoelectronics,^[2] and photodetectors^[3–5] since it is a wide-bandgap semiconductor. ZnO also plays a significant role in many biological processes^[6,7] as metalloenzymes or organic–inorganic hybrid complexes with, for example, amino acids and nucleic acids.^[8] Additionally, it is also applied in the medical field to enhance antibacterial action. The elimination of potential safety issues regarding the use of nanomaterials is a prerequisite for acceptance of these new technologies in society.^[9–13] In this respect it was recently demonstrated that a key property involved in oxidative injury, namely particle dissolution, could be modified by engineering nanoparticles (NPs), such as ZnO. George et al. have shown that iron doping changes the dissolution characteristics of ZnO NPs, which could lead to rendering the material less toxic and hence reduce oxidative injury.^[14]

The appropriate evaluation and elimination of toxicity of nanomaterials has been a subject of considerable concern.^[15,16] The traditional toxicological approach to chemical testing involves animal studies as the primary means of

hazard assessment. This strategy is costly, labor intensive, and raises ethical issues.^[17] While admittedly it is impossible to perform risk assessment and management without in vivo toxicological data, it is absolutely necessary to develop predictive in vitro toxicological screening to evaluate the safety of nanomaterials.

Recently, George et al.^[14] reported the synthesis of Fe-doped ZnO NPs and investigations of their toxicity (hereafter, we will use Fe–ZnO NPs to refer to Fe-doped ZnO nanoparticles, unless otherwise stated). Fe–ZnO NPs show immense potential for a wide range of applications as the Fe content lowers their solubility, and hence their toxicity. The materials were produced by flame spray pyrolysis (FSP), where an Fe concentration of more than 10 at% was successfully incorporated in the wurtzite ZnO matrix. The material has been characterized by transmission electron microscopy (TEM) imaging, inner-shell electron energy loss spectroscopy (ISEELS), and X-ray diffraction (XRD) techniques. In summary, George et al.'s measurements indicate that the overall lattice structure of ZnO is not distorted by the Fe atoms; Fe is homogeneously distributed in the NPs, and basically replaces Zn atoms at their lattice positions.^[14] This indicates the oxidation state of iron to be Fe²⁺. The last finding is remarkable, considering that significant amounts of Fe²⁺ (note that FeO has a rocksalt structure which is hexacoordinated) can be incorporated into ZnO (wurtzite structure, tetraordinated) with only minor changes in the ZnO lattice parameters. The possible presence of Fe atoms with other oxidation states (i.e., Fe³⁺) thus remains an open question. This important issue requires further theoretical and experimental investigation because it determines the magnetic properties of the doped ZnO.

In the present work, the following issues have been theoretically addressed, which have emerged after doping Fe in ZnO using versatile FSP:

- The thermodynamic stability of Fe–ZnO NPs
- The influence of Fe on the structure of ZnO
- The distribution of Fe in the ZnO lattice
- The preferable oxidation state of Fe (Fe²⁺ or Fe³⁺) in the lattice

We have computationally investigated Fe-doped systems with Fe contents of up to 18 at% and three types of defects (substitution of Zn by Fe (Fe²⁺), combinations of substitution with a zinc vacancy (Fe³⁺–Zn), and combinations of substitution of Zn by Fe with interstitial oxygen (Fe³⁺–O)). The basic electronic and energetic properties are investigated and compared with experimental data obtained for ZnO NPs. Moreover, we have performed high-resolution ISEELS measurements and compared them to the computed spectra in order to study the local chemical bonding and coordination of substitutive Fe atoms.

2. Computational and Experimental Details

The experimentally obtained NPs have a size of about 20 nm.^[14] These relatively large NPs have a small surface-to-bulk ratio. We therefore restrict our theoretical investigations

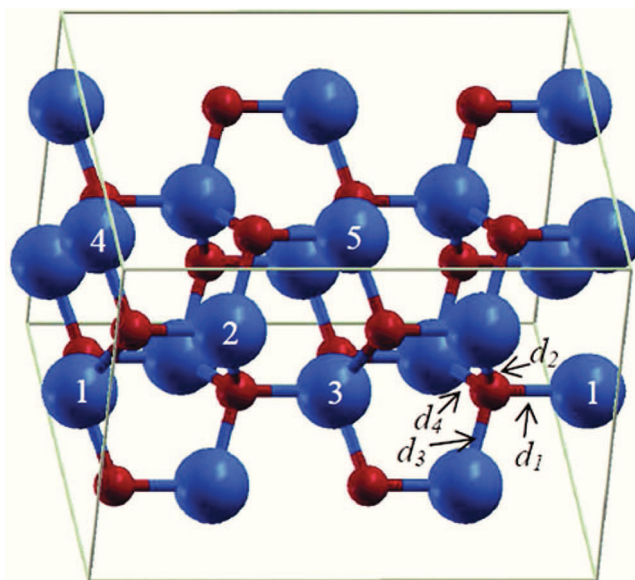


Figure 1. The $2 \times 2 \times 2$ ZnO supercell with substitutional positions marked 1–5. See Table 2 for the Fe substitution configurations studied in this work. The local bonds are indicated by d_1 – d_4 : the d_1 bond connects two hexagonal layers; d_2 – d_4 are equivalent bonds in the same hexagonal layer. Blue: Zn; red: O.

to the bulk phase, which is represented by a periodic model and neglects surface and finite size effects. We postpone the discussion of the surface effects to a forthcoming article. ZnO has the wurtzite crystal structure (see **Figure 1**) with two molecular units of ZnO.^[18] The systems with impurities were treated within the supercell approach. To obtain equivalent k -points in the reciprocal space, a $2 \times 2 \times 2$ unit cell was used, and shrinking factor 2, corresponding to eight independent k -points in the irreducible part of the Brillouin zone within the Monkhorst–Pack scheme.^[19] Full optimization of atomic positions and cell parameters in fractional coordinates was carried out in all cases. All optimizations and calculations of electronic structure were performed using the CRYSTAL09 code,^[20] hence employing local Gaussian-type basis functions. As relativistic effects are not significant, we chose all-electron basis sets (Zn: 86-411(41d)G,^[21] O: 6-31(1d),^[22] Fe: 86-411(41d)G^[23]) in order to be independent of the parameterization of pseudopotentials.

Following the literature, we placed strong emphasis on selecting the most suitable density functional for our study. **Table 1** compares the lattice parameters, the formation energy (E_f), defined as

$$E_f = E_{\text{ZnO}} - 0.5 \times n_{\text{O}} E_{\text{O}} - n_{\text{Zn}} E_{\text{Zn}} \quad (1)$$

and the bandgap of ZnO, calculated using various density functionals. In Equation 1, E_{ZnO} denotes the total energy of the ZnO unit cell, E_{Zn} is the energy of a single Zn atom in metallic Zn, and E_{O} is the energy of a single oxygen molecule (triplet spin state); n_{O} and n_{Zn} are the numbers of O₂ molecules and Zn atoms, respectively. All employed functionals, including local density approximation (LDA), generalized gradient approximation (GGA), and hybrid functionals, give reasonable structural parameters compared with available

Table 1. Calculated lattice parameters, formation energy (E_f), and bandgap (Δ) obtained with different functionals compared with experimental data. The E_f is calculated according to Equation 1. All experimental and calculated values are given for the crystalline conventional cell (lengths in Å and energies in eV).

		LDA	PW(GGA)	PBE(GGA)	B3LYP	PBE0	Experiments
ZnO	<i>a</i>	3.18	3.27	3.28	3.28	3.25	3.25, ^[24] 3.249, ^[25] 3.25 ^[26]
	<i>b</i>	3.18	3.27	3.28	3.28	3.25	3.25, ^[24] 3.249, ^[25] 3.25 ^[26]
	<i>c</i>	5.15	5.27	5.28	5.28	5.17	5.20, ^[24] 5.205, ^[25] 5.21 ^[26]
	<i>V</i>	45.24	48.72	49.04	49.07	47.24	47.62 ^[24]
	E_f	-4.72	-4.30	-4.14	-4.72	-3.67	-3.61, ^[27] -3.63 ^[28]
	Δ	1.30	1.27	1.25	3.22	3.59	3.3 – 3.44, ^[29] 3.4 ^[26]
FeO	<i>a</i>	4.17	4.28	4.18	4.25	4.21	4.30, ^[30] 4.22 ^[31]
	Δ	0	0	0	2.57	3.24	2.4, ^[32] 2.4 ^[33]

experimental data. The bandgaps are strongly underestimated by all pure density functionals,^[26,34] while they are reasonably reproduced by the two hybrid functionals (B3LYP and PBE0).^[29,35] The experimental formation energy is reproduced best by the PBE0 functional; therefore, in these studies we have chosen this hybrid functional.

Band structure and projected density of states (PDOS) of pure ZnO are given in Figure S1 (Supporting Information). In particular, the unoccupied states are shifted to higher energies compared with the PBE functional by the exact exchange contribution, which results in the correct bandgap. At the same time, the bands belonging to 3d orbitals calculated with the PBE0 hybrid functional are also improved, being located at a deeper position compared to the PBE functional, which is consistent with the experimental data.^[36,37]

The calculated lattice parameters of FeO are slightly underestimated (Table 1). Moreover, the pure density functionals fail to correctly describe FeO as a Mott insulator.^[30] The calculated bandgap is improved, but overestimated, by the PBE0 hybrid functional; care has thus to be taken when using the PBE0 hybrid functional to calculate the electronic structure of FeO (see Table 1).

As the Fe-doped systems contain partially unoccupied 3d orbitals, we carried out spin-polarized calculations based on different FeO concentrations to evaluate how the spin polarization influences the stability of various configurations. The Fe atom concentration in Fe–ZnO NPs was set to 6.25, 12.50, and 18.75 at%. Formation energies of Fe–ZnO (alloying energies) were calculated as

$$E_{f,doped} = E_{doped} - n_{ZnO} E_{ZnO} - n_{FeO} E_{FeO} (E_{Fe_2O_3}) \quad (2)$$

where $E_{f,doped}$ is the formation energy, E_{doped} denotes the total energy of the Fe–ZnO, E_{ZnO} is the total energy of ZnO in

the wurtzite phase, and E_{FeO} is the total energy of FeO in the rocksalt structured phase. In Equation 2, the E_{FeO} is replaced by $E_{Fe_2O_3}$ for formation energy calculations of Fe³⁺ models. Overall, our validation calculations suggest that the PBE0 functional is the best choice and it will be used throughout this study. It performs best for ZnO, which dominates our structural models, and also gives reasonable results for FeO.

We have studied single, double, and triple Fe substitutions in ZnO, which result in 6.25, 12.50, and 18.75 at% concentrations of iron, respectively. For each concentration there are various possible distributions of the Fe atoms in the ZnO bulk structure. All sites of Zn atoms are equivalent for a single Fe dopant (1Fe_{subs}(a)). For double Fe dopants, we can distinguish four substitution models, which we call 2Fe_{subs}(a)–2Fe_{subs}(d) (see Figure 1 and **Table 2**). We further studied four models of triple Fe dopants, called 3Fe_{subs}(a)–3Fe_{subs}(d). To make all models easily comparable, the Zn site 1 was selected as a reference point in all configurations.

Additional composite defects (2Fe_{subs}-Zn_{vac} and 2Fe_{subs}-O_{int}) have been studied, built for double Fe dopants, to investigate other possible valence states of Fe in ZnO NPs. The interstitial O and Zn vacancies are arbitrarily chosen in 2Fe_{subs}(a)–2Fe_{subs}(d) to build 2Fe_{subs}-O_{int} and 2Fe_{subs}-Zn_{vac} models, respectively. This part of our work focuses on how composite defects influence thermodynamic stability and crystal structure.

ISEELS and X-ray absorption spectroscopy (XAS including X-ray absorption near-edge structure (XANES)) are well-known techniques to elucidate the electronic structure of the materials.^[38] Both are based on exciting a core electron to an unoccupied conduction band, thereby allowing the analysis of the local environment and oxidation state of the probed atoms in the compound. There are different

Table 2. Configurations and atomic percentage of Fe atoms substituted in ZnO NPs. Site 1 denotes a single Fe dopant (1Fe_{subs}); sites 1 to 5 represent double (2Fe_{subs}(a)–2Fe_{subs}(d)) and triple (3Fe_{subs}(a)–3Fe_{subs}(d)) Fe substitutions.

Configuration	1Fe _{subs}	2Fe _{subs}				3Fe _{subs}			
	a	a	b	c	d	a	b	c	d
FeO [at%]	6.25	12.50	12.50	12.50	12.50	18.75	18.75	18.75	18.75
substituted sites	1	1 + 2	1 + 4	1 + 3	1 + 5	1 + 2 + 3	1 + 2 + 4	1 + 3 + 4	1 + 2 + 5

theoretical approximations that can be employed to compute ISEELS spectra. For small momentum transfer, that is, the dipole limit, ISEELS and XANES can be described with the same formalism.^[39] In the present work, we have applied the multiple-scattering approach based on the FEFF9.0 code.^[40]

High-resolution transmission electron microscopy (HRTEM) studies were carried out using an FEI Titan 80/300 ST instrument equipped with a Cs corrector for spherical aberration of the objective lens, a high-angle annular dark field (HAADF) detector, a GATAN post-column imaging filter, and an EDAX energy-dispersive X-ray (EDX) spectrometer. In all investigations the microscope was operated at an acceleration voltage of 300 kV. EDX spectra were obtained using a dispersion of 10 eV channel⁻¹ and compositions were quantified using FEI's ES-Vision software delivered with the microscope. ISEELS spectra were acquired with the GIF using a dispersion of 0.5 or 0.1 eV channel⁻¹.

XRD measurements of ZnO or Fe–ZnO NPs were performed using a PANalytical X'Pert MPD PRO diffracting system equipped with Ni-filtered Cu_{Kα} ($\lambda = 0.154$ nm) radiation, 1/4° fixed divergence, a primary and secondary Soller slit with 0.04 rad aperture, a circular sample holder with 16 mm diameter, and X'Celerator detector, with application of a continuous scan in the 2θ range of 15–80°. The instrumental contribution to the peak broadening was corrected using LaB₆ as an instrumental standard. For microscopic measurements, ZnO or Fe–ZnO particles (2–5 mg) were dispersed in absolute ethanol followed by ultrasonification for 1 h. A drop from the resulting dispersed solution was placed on a TEM grid using an eye dropper and dried at room temperature. Energy-filtered TEM (EFTEM) images of pre- and post-edges of elemental mappings were obtained from the data by energy calibration and background subtraction. Zero-loss spectra were also obtained at each sampling point for energy calibration and to identify the homogeneity of the samples.

3. Results and Discussion

3.1. Structural and Energetic Stability

The NPs based on pure and Fe-doped ZnO were synthesized using the FSP technique and physicochemically characterized. The X-ray characterization and Rietveld refinement of the patterns of pure and Fe-doped ZnO revealed that the crystal disorder (the disorder of the crystalline NPs experienced when Fe atoms were incorporated into the ZnO crystal lattice) increases with increasing Fe loading. The crystal sizes are found to decrease with respect to Fe loading both from XRD and BET (Brunauer–Emmett–Teller) measurements from about 15–20 nm (d_{XRD} and d_{BET} for pure ZnO) to about 5–7 nm

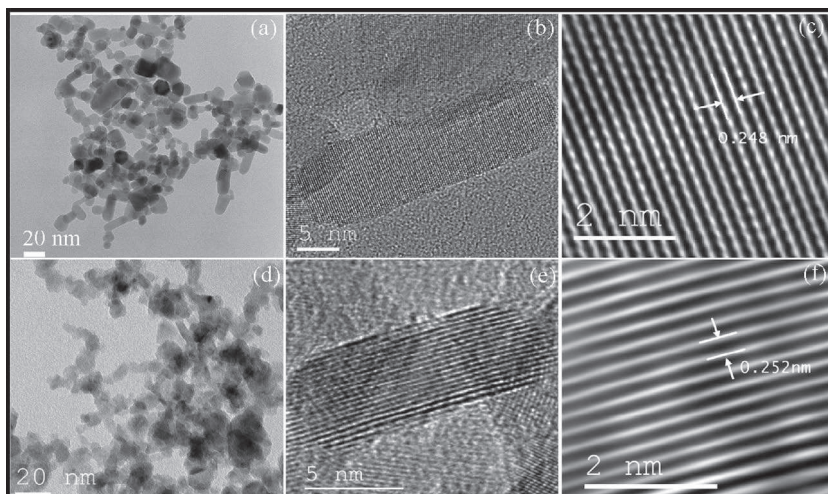


Figure 2. TEM investigation. a) Overview, b) HRTEM, and c) Fourier-filtered magnified HRTEM image of pure ZnO NPs; d) overview, e) HRTEM, and f) Fourier-filtered magnified HRTEM image of 10% Fe-doped ZnO NPs.

(d_{XRD} and d_{BET} for 10 at% Fe-doped ZnO).^[14] HRTEM images of single NPs of pure and Fe-doped ZnO reveal highly crystalline structures with lattice spacing of 0.248 nm for undoped and 0.252 nm for 10% doped ZnO (see **Figure 2** and **Figure 3**). The distribution of Fe atoms in the ZnO matrix was also investigated using EFTEM. The elemental maps of the parent and doped NPs show a homogeneous distribution of Fe in the ZnO matrix (see George et al.^[14] for details).

We have calculated the energetic and electronic properties of Fe-doped ZnO with Fe content of 6.25, 12.50, and 18.75 at%. Different concentrations of Fe in the ZnO matrix were investigated in either low-spin or high-spin configurations. The results show that the structures with high spin are more stable than those with low spin (see Table S1, Supporting Information) and this is consistent with the experimental findings.^[14] While the

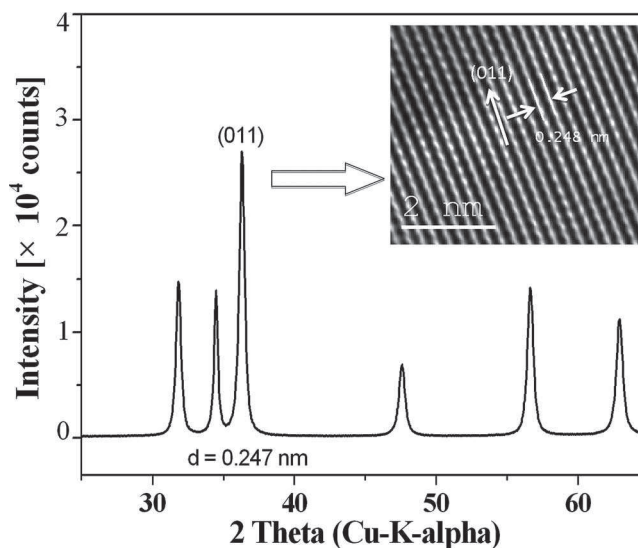


Figure 3. The lattice distances of pure ZnO and 10% Fe-doped ZnO are found to be 0.248 and 0.252 nm, respectively, in the (011) direction, which matches reasonably with the XRD pattern observed at the 2θ value of 36.17°.

Table 3. Computed formation energies per Fe atom for the different sites and structures. The symbols a–d represent variable configurations. See Tables S2 and S3 (Supporting Information) for details.

X	1Fe _{subs} (x)	2Fe _{subs} (x)	3Fe _{subs} (x)	2Fe _{subs} -Zn _{vac} (x)	2Fe _{subs} -O _{int} (x)
a	-0.97	-1.14	-1.20	-0.65	-0.38
b	-0.97	-1.10	-1.16	-0.70	-0.14
c	-0.97	-1.16	-1.18	-0.48	-0.13
d	-0.97	-1.16	-1.21	-0.65	0.44

oxidation state of Fe ions doped in ZnO depends on the synthesis method, Fe was previously found to be present as high-spin Fe²⁺ ions, which substitute Zn²⁺ ions at the lattice sites.^[14]

Our simulations indicate that increasing the Fe concentration in the ZnO NPs up to a level of 18.25 at% increasingly stabilizes the ZnO lattice. Fe atoms prefer to distribute homogeneously in the NPs and the generation of Fe islands inside ZnO NPs is energetically unfavorable. This is supported by the stability of different configurations: for example, in the case of ZnO with 12.5 at% Fe dopant, the most stable configurations are 2Fe_{subs}(c) and 2Fe_{subs}(d), where the distance between two Fe atoms is the largest possible for our supercell approach, namely 5.24 and 6.19 Å, respectively. This is consistent with experiment where, using pre- and post-edge elemental mapping as well as EELS in scanning TEM (STEM) mode, George et al.^[14] showed that both Fe and Zn are homogeneously distributed in the doped ZnO NPs.

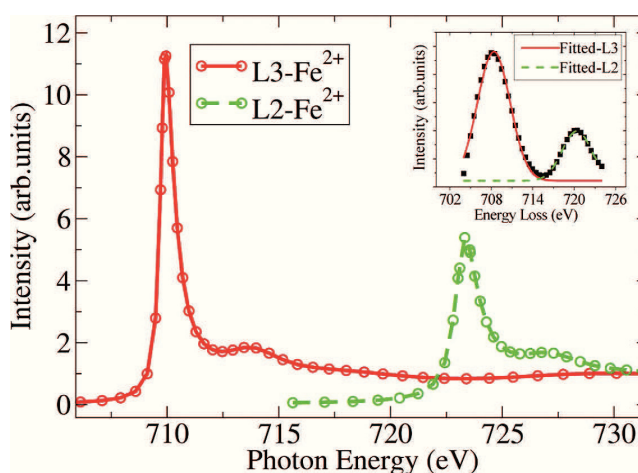
Table 3 lists the computed formation energies of the different Fe substitutions in ZnO reported per Fe atom. Interestingly, in all cases except for 2Fe_{subs}-O_{int}(d) the doping with FeO stabilizes the lattice. Following the energetics given by our first-principles calculations, substitutional doping is strongly favored and valence states other than Fe²⁺ would not be expected. Doping ZnO with Fe has very small effects on the ZnO structure where, for example, the lattice geometry changes by only 0.03 Å in bond lengths and by 0.2° in bond angles in the 1Fe_{subs} case. The most stable configurations (2Fe_{subs}(c) and 2Fe_{subs}(d)) have even smaller lattice deformations. Further increasing the Fe concentration to 18.75 at% again results in minor structural changes, that is, for the most stable configuration 3Fe_{subs}(d) by 0.03 Å in bond length and 0.5° in bond angle, compared with the lattice parameters of pure bulk ZnO. The binding energies of the various configurations for Fe-doped ZnO are visualized in Figure S3 (Supporting Information).

Both composite defects (2Fe_{subs}-Zn_{vac} and 2Fe_{subs}-O_{int}) are less stable than the 2Fe_{subs} systems. This is easily understood as both situations, with either a Zn vacancy or an interstitial O atom, introduce extra stress into the 2Fe_{subs} systems. We found that the 2Fe_{subs}-O_{int}(a) case is the most stable for interstitial O atoms, which implies that the two high-valence iron ions prefer to locate next to the interstitial oxygen in the ZnO matrix, which can be rationalized by stronger electrostatic interactions. But solely based on the energetics and structural data, we still cannot exclude the presence of interstitial O and Zn vacancies since the lattice parameters of 2Fe_{subs}-O_{int} and 2Fe_{subs}-Zn_{vac} are just slightly altered. Even the largest lattice deformation of 2Fe_{subs}-O_{int}(d) would be rather difficult to resolve in TEM experiments.

3.2. Core–Hole Spectroscopy (ISEELS Measurements and XANES Simulations)

We have calculated and measured the iron and oxygen ISEEL spectra of Fe–ZnO NPs to determine the valence state of Fe.

In our experiments, the L2 and L3 edges are split by approximately 12 eV in Fe–ZnO NPs, while our calculated value is 13 eV for 2Fe_{subs}(c) (Fe²⁺) (see **Figure 4**). On the other hand, the absolute energy position of the computed spectrum is about 2 eV higher than in the experiment, which is most likely due to modeling Fe–ZnO NPs as a periodic bulk system and using the LDA functional in the spectrum calculations with FEFF9.0. The small lattice deformations of around 1% do not induce a chemical shift of iron (see Figure S4, Supporting Information). In the following we will use the integrated intensity in the computed white line, that is, the principal sharp peak, from the different models of Fe–ZnO NPs to verify the oxidation state of Fe in the models; Fe²⁺ and Fe³⁺ differ in the number of unoccupied 3d states, which gives higher intensity in the white line of Fe³⁺ (2p→3d transition) but does not lead to a different peak energy (assuming the same environment). Having thus confirmed the character of Fe in the different models, we turn to the oxygen K-edge and show that partial hybridization with Fe³⁺ gives rise to a specific peak in the oxygen spectrum which, however, is not observed in the experiment. We can thus exclude any significant contribution of Fe³⁺ in the Fe–ZnO NPs.


Figure 4. Comparison between experimental and calculated L3 and L2 XANES of Fe–ZnO NPs in the 2Fe_{subs}(c) case. L3: red solid curve; L2: green dashed curve. The inset shows experimental data.

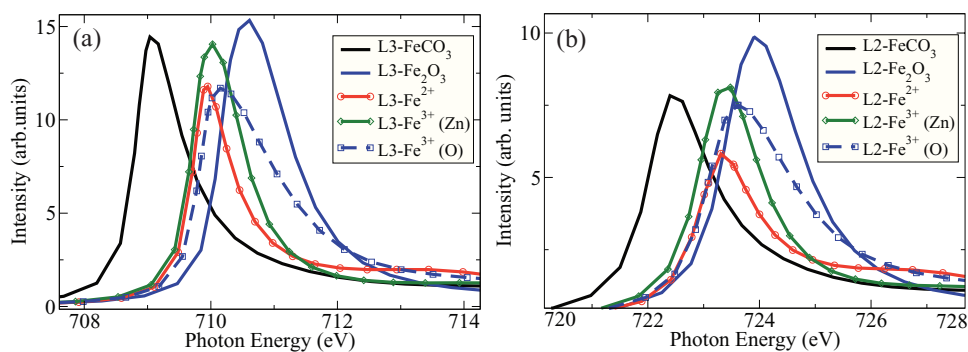


Figure 5. Comparison of a) L3 XANES and b) L2 XANES among Fe^{2+} and Fe^{3+} models in ZnO NPs. FeCO_3 : black, Fe_2O_3 : blue, $2\text{Fe}_{\text{subs}}(\text{c})$ (Fe^{2+}): red, $2\text{Fe}_{\text{subs}}\text{-Zn}_{\text{vac}}(\text{b})$ ($\text{Fe}^{3+}\text{-Zn}$): green, and $2\text{Fe}_{\text{subs}}\text{-O}_{\text{int}}(\text{a})$ ($\text{Fe}^{3+}\text{-O}$): blue dashed curves.

Two typical compounds, FeCO_3 and Fe_2O_3 , were selected for calibration for the Fe^{2+} and Fe^{3+} oxidation states, respectively (**Figure 5**). Large clusters containing 640 atoms for FeCO_3 and Fe_2O_3 , 864 atoms for $2\text{Fe}_{\text{subs}}(\text{c})$ (Fe^{2+}), 837 atoms for $2\text{Fe}_{\text{subs}}\text{-Zn}_{\text{vac}}(\text{b})$ (Fe^{3+}), and 891 atoms for $2\text{Fe}_{\text{subs}}\text{-O}_{\text{int}}(\text{a})$ (Fe^{3+}) were used to ensure reliable computed spectra. The shift of the white line at the L2 edge of Fe, upon going from FeCO_3 to Fe_2O_3 , in the experimental measurement is 1.8 eV although the FeCO_3 sample was not chemically pure.^[41] On the other hand, Benzerara et al.^[42] have obtained a shift of 1.7 eV by comparing pyroxene (Fe^{2+}) and Fe_2O_3 . Our calculated value is 1.6 eV, which is in good agreement with these values.

At both the L3 and L2 edges, the white lines from the $2\text{Fe}_{\text{subs}}(\text{c})$ (Fe^{2+}), $2\text{Fe}_{\text{subs}}\text{-Zn}_{\text{vac}}(\text{b})$ (Fe^{3+}), and $2\text{Fe}_{\text{subs}}\text{-O}_{\text{int}}(\text{a})$ (Fe^{3+}) models are essentially intermediate between those of FeCO_3 and Fe_2O_3 and the main differences are found in the shape and integrated intensities. Integrating the intensity over the L2 and L3 peaks of Fe_2O_3 and FeCO_3 we find a ratio of 1:0.75, while for the $2\text{Fe}_{\text{subs}}(\text{c})$, $2\text{Fe}_{\text{subs}}\text{-Zn}_{\text{vac}}(\text{b})$, and $2\text{Fe}_{\text{subs}}\text{-O}_{\text{int}}(\text{a})$ we obtain 0.67:1.00:0.98, thus confirming that the latter two models indeed represent Fe^{3+} , while $2\text{Fe}_{\text{subs}}(\text{c})$ corresponds to Fe^{2+} as per construction. The shifts in energy position are, however, clearly too small to justify conclusions on the Fe oxidation state. In FeCO_3 iron is typically characterized as Fe^{2+} , sixfold coordinated to O atoms at 2.14 Å distance. The fourfold coordination in $2\text{Fe}_{\text{subs}}(\text{c})$ (Fe^{2+}), on the other hand, has all bond lengths shrunk to approximately 1.98 Å (see **Figure 6**) which, however, does not result in a significant chemical shift as seen in **Figure 5**.

In Fe_2O_3 the Fe atoms are characterized as Fe^{3+} with six equivalent Fe–O bonds. If interstitial O is present in Fe–ZnO NPs ($2\text{Fe}_{\text{subs}}\text{-O}_{\text{int}}(\text{a})$, Fe^{3+}), Fe will be bonded to only five O atoms. The five Fe–O bonds are not identical, as expressed by their bond lengths ranging from 1.89 to 2.11 Å, which leads to a chemical shift of ≈ 0.5 eV compared to Fe_2O_3 . It thus appears that the structural environment has a stronger influence on the ISEELS data than the iron oxidation state. The positions of the L3 and L2 white line peaks in $2\text{Fe}_{\text{subs}}\text{-O}_{\text{int}}(\text{a})$ (Fe^{3+}) are consequently insufficient to draw final conclusions about the Fe oxidation states, and we instead turn to an analysis of the ISEELS at the oxygen K-edge.

The neighboring O atoms around Fe are helpful to calibrate the valence state of the substitutive atoms, as well as providing further information on the interaction between environment (O) and system (Fe) in the previous calculations. Thus, we performed XANES calculations of O in ZnO and in the $2\text{Fe}_{\text{subs}}(\text{c})$ (Fe^{2+}), $2\text{Fe}_{\text{subs}}\text{-Zn}_{\text{vac}}(\text{b})$ (Fe^{3+}), and $2\text{Fe}_{\text{subs}}\text{-O}_{\text{int}}(\text{a})$ (Fe^{3+}) models. Comparing the experimental ISEELS and calculated K-edge XANES of O atoms (**Figure 7**), we find an overall shift to higher energy by about 5 eV in the computed spectra; this is a multiple-scattering feature which should be most reliably reproduced by the FEFF9.0 code, and we take this to indicate that the computed spectra should be shifted down by ≈ 5 eV for comparison with experiment. With this in mind **Figure 7** shows that, if $2\text{Fe}_{\text{subs}}\text{-Zn}_{\text{vac}}(\text{b})$ (Fe^{3+}) is present in the Fe–ZnO NPs, the charge transfer between Fe and O is incomplete leaving empty 2p states on oxygen that give rise to a sharp peak below 530 eV, which was not observed in our measurement. This is a clear

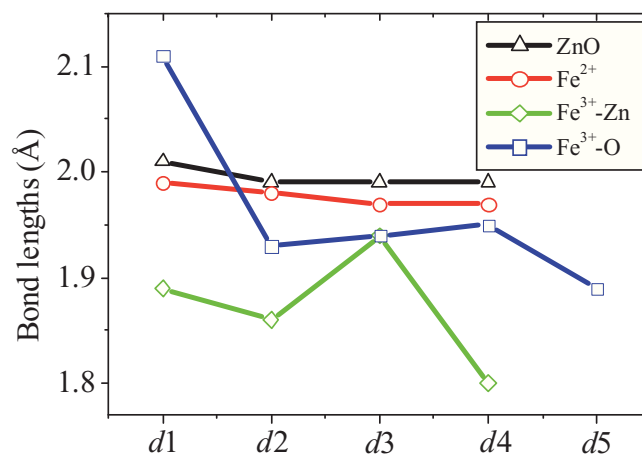


Figure 6. Comparison of calculated bond lengths [Å] in ZnO bulk, $2\text{Fe}_{\text{subs}}(\text{c})$ (Fe^{2+}), $2\text{Fe}_{\text{subs}}\text{-Zn}_{\text{vac}}(\text{b})$ ($\text{Fe}^{3+}\text{-Zn}$), and $2\text{Fe}_{\text{subs}}\text{-O}_{\text{int}}(\text{a})$ ($\text{Fe}^{3+}\text{-O}$); d_1 is the Zn–O bond length linking two adjacent layers; d_2 , d_3 , and d_4 are the bond lengths within the same layer, and d_5 is the bond length between the adsorbed O atom and Fe dopants.

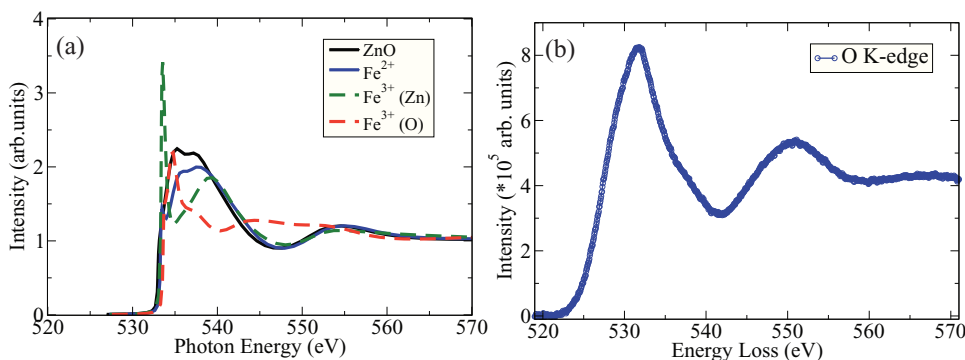


Figure 7. a) Comparison among calculated XANES of the oxygen K-shell; the Fe²⁺ model is described by 2Fe_{subs}(c), the Fe³⁺ (Zn) model is described by 2Fe_{subs}-Zn_{vac}(b), and the Fe³⁺ (O) model is described by 2Fe_{subs}-O_{int}(a). b) Measurement by ISEELS.

spectroscopic signal, the absence of which demonstrates that the content of 2Fe_{subs}-Zn_{vac}(b) (Fe³⁺) should be at most a trace in Fe–ZnO NPs. The same phenomenon occurs in 2Fe_{subs}-O_{int}(a), where in addition the minimum in the intensity in the range of 540–550 eV would be flattened by the presence of Fe³⁺. Therefore, we can conclude that the content of Fe³⁺ should be negligible in the Fe–ZnO NPs synthesized by George et al. using FSP.

The formation energy calculations together with the oxygen K-edge spectrum give a consistent picture of the negligible content of Fe in the Fe³⁺ oxidation state. For 2Fe_{subs}(c) (Fe²⁺), the formation energy is much lower than for 2Fe_{subs}-Zn_{vac}(b) (Fe³⁺) and 2Fe_{subs}-O_{int}(a) (Fe³⁺). The chemical reaction is not only primarily induced by thermodynamics but also by kinetics. The kinetic diffusion is strongly facilitated by the pyrolysis reaction in the synthesis process of NPs. Thus, the Fe–ZnO NPs can reach the most stable configuration in this process with the occurrence of at most very few Fe³⁺ defects and a homogeneous distribution of Fe²⁺ in the Fe–ZnO NPs.

3.3. Alternative Determination of Oxidation State

An empirical method for determination of the oxidation state of Fe has been presented by Cavé et al.^[43] They showed experimentally that the ratio of the intensities below the L2 and L3 white lines depends on the oxidation state. For that, the pre-edge background intensity was removed from the spectrum assuming an inverse power law. Then the pure intensity contained in the L3 and L2 peaks was isolated by removing the post-edge background using a double arctangent step function. Finally the L3/L2 ratio was determined. They found ratios of approximately 4.2 for Fe²⁺, 5.0 for Fe³⁺, and 5.6 for Fe⁴⁺ using an acceleration voltage of 200 kV. According to Leapman et al.,^[44] the intensity ratio only weakly depends on the acceleration voltage used, and one would expect a ratio of 4.1 for Fe²⁺ at the 300 kV used in our measurements. We evaluated our EEL spectra using the method of Cavé et al.^[43] and found an intensity ratio of 4.0 ± 0.4. This result is in agreement with Section 3.2, where the oxidation state was found to be Fe²⁺.

4. Conclusion

We have investigated the structures and formation energies of various defects, as well as the electronic properties, of Fe-doped ZnO NPs by using first-principles calculations employing the PBE0 hybrid functional, which has been thoroughly validated in this work. The computed energetics for different cases with Fe content of 6.25, 12.5, and 18.75 at% indicate that doping with Fe stabilizes the ZnO NPs. The lattice parameters were found to change negligibly upon Fe substitution, which is consistent with our experimental TEM findings. The geometrical configuration demonstrates that Fe prefers to distribute homogeneously in Fe–ZnO NPs.

XANES calculations and measurements were employed to explore the valence state of iron in the studied systems. The theoretical and experimental results are in very good agreement. Fe²⁺ dominates the valence state of iron in Fe-doped ZnO NPs, as can be observed directly in high-resolution ISEELS measurements through the lack of a signal indicating empty oxygen 2p character, which would be the consequence of substitutional Fe in the Fe³⁺ state. This was confirmed by an alternative determination of the oxidation state.

Supporting Information

Supporting Information is available from the Wiley Online Library or from the author.

Acknowledgements

The authors acknowledge fruitful discussions with K. T. Wikfeldt. J.X. acknowledges financial support by the Chinese Scholarship Council, A.K. and T.H. acknowledge financial support by the European Research Council (ERC, GA 256962). L.M. and T.H. thank the North German Supercomputing Alliance (HLRN) for a grant for computer time. S.P. and L.M. would like to thank the National Science Foundation and the Environmental Protection Agency under Cooperative Agreement Number DBI-0830117 for supporting this work. Key support was also provided by the US Public Health Service

Grants U19 ES019528 (UCLA Center for NanoBiology and Predictive Toxicology), RO1 ES016746, and RC2 ES018766.

- [1] K. Ueda, H. Tabata, T. Kawai, *Appl. Phys. Lett.* **2001**, *79*, 988.
- [2] P. V. Kamat, *J. Phys. Chem. B* **2002**, *106*, 7729.
- [3] C. Soci, A. Zhang, B. Xiang, S. A. Dayeh, D. P. R. Aplin, J. Park, X. Y. Bao, Y. H. Lo, D. Wang, *Nano Lett.* **2007**, *7*, 1003.
- [4] K. C. Hui, H. C. Ong, P. F. Lee, J. Y. Dai, *Appl. Phys. Lett.* **2005**, *86*, 152116.
- [5] J. P. Richters, T. Voss, L. Wischmeier, L. Röchmann, J. Gutowski, *Appl. Phys. Lett.* **2008**, *92*, 011103.
- [6] S. Guo, S. Dong, *Trends Anal. Chem.* **2008**, *28*, 96.
- [7] S. P. Singh, S. K. Arya, P. Pandey, B. D. Malhotra, S. Saha, K. Sreenivas, V. Gupta, *Appl. Phys. Lett.* **2007**, *91*, 063901.
- [8] O. Taratula, E. Galoppini, R. Mendelsohn, P. I. Reyes, Z. Zhang, Z. Duan, J. Zhong, Y. Lu, *Langmuir* **2009**, *25*, 2107.
- [9] A. Nel, T. Xia, L. Mädler, N. Li, *Science* **2006**, *311*, 622.
- [10] G. Oberdörster, E. Oberdörster, J. Oberdörster, *Environ. Health Perspect.* **2005**, *113*, 823.
- [11] A. Nel, *Science* **2005**, *308*, 804.
- [12] T. Cedervall, I. Lynch, S. Lindman, T. Berggård, E. Thulin, H. Nilsson, K. A. Dawson, S. Linse, *Proc. Natl. Acad. Sci. USA* **2007**, *104*, 2050.
- [13] A. A. Vertegel, R. W. Siegel, J. S. Dordick, *Langmuir* **2004**, *20*, 6800.
- [14] S. George, S. Pokhrel, T. Xia, B. Gilbert, Z. Ji, M. Schowalter, A. Rosenauer, R. Damoiseaux, K. A. Bradley, L. Mädler, A. E. Nel, *ACS Nano* **2010**, *4*, 15.
- [15] T. Xia, M. Kovichich, J. Brant, M. Hotze, J. Sempf, T. Oberley, C. Sioutas, J. I. Yeh, M. R. Wiesner, A. E. Nel, *Nano Lett.* **2006**, *6*, 1794.
- [16] A. D. Maynard, R. J. Aitken, T. Butz, V. Colvin, K. Donaldson, G. Oberdörster, M. A. Philbert, J. Ryan, A. Seaton, V. Stone, S. S. Tinkle, L. Tran, N. J. Walker, D. B. Warheit, *Nature* **2006**, *444*, 267.
- [17] T. Xia, M. Kovichich, M. Liong, L. Mädler, B. Gilbert, H. Shi, J. I. Yeh, J. I. Zink, A. E. Nel, *ACS Nano* **2008**, *2*, 2121.
- [18] W. J. Fan, J. B. Xia, P. A. Agus, S. T. Tan, S. F. Yu, X. W. Sun, *J. Phys. Chem. B* **2006**, *99*, 013702.
- [19] H. J. Monkhorst, J. D. Pack, *Phys. Rev. B* **1976**, *13*, 5188.
- [20] R. Dovesi, V. R. Saunders, C. Roetti, R. Orlando, C. M. Zicovich-Wilson, F. Pascale, B. Civalieri, K. Doll, N. M. Harrison, I. J. Bush, Ph. D'Arco, M. Llunell, *CRYSTAL09 User's Manual*, University of Torino, Torino **2009**.
- [21] J. E. Jaffe, A. C. Hess, *Phys. Rev. B* **1993**, *48*, 7903.
- [22] C. Gatti, V. R. Saunders, C. Roetti, *J. Chem. Phys.* **1994**, *101*, 10686.
- [23] G. Valerio, M. Catti, R. Dovesi, R. Orlando, *Phys. Rev. B* **1995**, *52*, 2422.
- [24] C. H. Bates, W. B. White, R. Roy, *Science* **1962**, *137*, 993.
- [25] D. C. Look, D. C. Reynolds, J. W. Hemsky, R. L. Jones, J. R. Sizelove, *Appl. Phys. Lett.* **1999**, *75*, 811.
- [26] O. Madelung, M. Schulz, H. Weiss, *Numerical Data and Functional Relationships in Science and Technology*, Vol. 17, Springer, Berlin **1982**.
- [27] J. A. Dean, *Lange's Handbook of Chemistry*, 14th ed., McGraw-Hill, New York **1992**.
- [28] M. Oshikiri, F. Aryasetiawan, *J. Phys. Soc. Jpn.* **2000**, *69*, 2123.
- [29] X. Feng, *J. Phys.: Condens. Matter* **2004**, *16*, 4251.
- [30] S. D. Jacobsen, H. J. Reichmann, H. A. Spetzler, S. J. Mackwell, J. R. Smyth, R. J. Angel, C. A. MacCammon, *J. Geophys. Res.* **2002**, *107*, 2037.
- [31] J. M. Jackson, S. V. Sinogeikin, S. D. Jacobsen, H. J. Reichmann, S. J. Mackwell, J. D. Bass, *J. Geophys. Res.* **2006**, *111*, B09203.
- [32] R. J. Lad, V. E. Henrich, *Phys. Rev. B* **1989**, *39*, 13478.
- [33] P. S. Bagus, C. R. Brundle, T. J. Chuang, K. Wandelt, *Phys. Rev. Lett.* **1977**, *39*, 1229.
- [34] S. B. Zhang, S. H. Wei, A. Zunger, *Phys. Rev. B* **2001**, *63*, 075205.
- [35] F. Labat, I. Ciofini, C. Adamo, *J. Chem. Phys.* **2009**, *131*, 044708.
- [36] K. Hümmer, *Phys. Status Solidi B* **1973**, *56*, 249.
- [37] D. C. Reynolds, D. C. Look, B. Jogai, C. W. Litton, G. Cantwell, W. C. Harsch, *Phys. Rev. B* **1999**, *60*, 2340.
- [38] J. Stöhr, *NEXAFS Spectroscopy*, Springer, Berlin **1992**.
- [39] J. J. Rehr, R. C. Albers, *Rev. Mod. Phys.* **2000**, *72*, 621.
- [40] A. L. Ankudinov, B. Ravel, J. J. Rehr, S. D. Conradson, *Phys. Rev. B* **1998**, *58*, 7565.
- [41] A. Isambert, T. De Resseguier, A. Gloter, B. Reynard, F. Guyot, J. P. Valet, *Earth Planetary Sci. Lett.* **2006**, *243*, 820.
- [42] K. Benzerara, T. H. Yoon, N. Menguy, T. Tylliszczak, G. E. Brown, Jr., *Proc. Natl. Acad. Sci. USA* **2005**, *102*, 979.
- [43] L. Cavé, T. Al, D. Loomer, S. Cogswell, L. Weaver, *Micron* **2005**, *37*, 301.
- [44] R. D. Leapman, L. A. Grunes, P. L. Fejes, *Phys. Rev. B* **1982**, *26*, 614.

Received: May 18, 2011

Published online: September 12, 2011

Contents

Figure S1. Comparison of band structure and PDOS of ZnO with PBE and PBE0 functional, red dashed line is Fermi level, the intensity of d orbitals of Zn is given by half amount, the energy of Fermi level is set to zero.

Figure S2. Comparison of band structure and DOS of FeO with PBE and PBE0 functional, red dashed line is Fermi level which is set to zero, blue curves are calculated result with PBE0 and dotted curves are calculated with PBE.

Figure S3. Calculated formation energies of Fe-ZnO NPs ($1Fe_{\text{subs}}$, $2Fe_{\text{subs}}$ and $3Fe_{\text{subs}}$). Only the open shell case was considered. The blue bar is most stable case.

Figure S4. Comparison of calculated L3-XANES between $2Fe_{\text{subs}}(c)$ with $2Fe_{\text{subs}}(c)'$, $2Fe_{\text{subs}}(c)$ in red curve and $2Fe_{\text{subs}}(c)'$ in blue curve. The $2Fe_{\text{subs}}(c)'$ is the system with same internal atomic configuration of $2Fe_{\text{subs}}(c)$ with lattice parameters of ZnO.

Figure S5. Comparison between calculated K-XANES of neighbor O around Fe in ZnO system with the content of Fe^{3+} , 1%, 3%, 5%, 7% and 9% ($2Fe_{\text{subs}}-Zn_{\text{vac}}(b)$), respectively, and experimental measurements in pink curve.

Table S1. Calculated formation energies of Fe-ZnO NPs ($1Fe_{\text{subs}}$, $2Fe_{\text{subs}}$ and $3Fe_{\text{subs}}$) with closed (low spin) and open shell (high spin) cases (eV).

Table S2. Calculated lattice parameters (in Å and in °) in composite defects $2Fe_{\text{subs}}-Zn_{\text{vac}}$ and $2Fe_{\text{subs}}-O_{\text{int}}$ compared with Fe-substitution ($2Fe_{\text{subs}}$). The formation energies (E_f) are given as well (in eV).

Table S3. Calculated lattice parameters (in Å and °) in Fe-ZnO NPs ($1Fe_{\text{subs}}$, $2Fe_{\text{subs}}$ and $3Fe_{\text{subs}}$) compared with ZnO wurtzite phase.

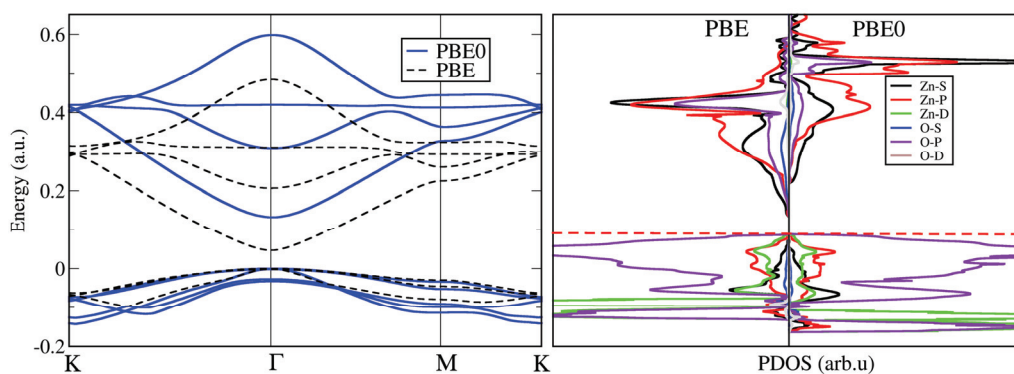


Figure S1. Comparison of band structure and PDOS of ZnO with PBE and PBE0 functional, red dashed line is Fermi level, the intensity of d orbital of Zn is given by half amount, the energy of Fermi level is set to zero.

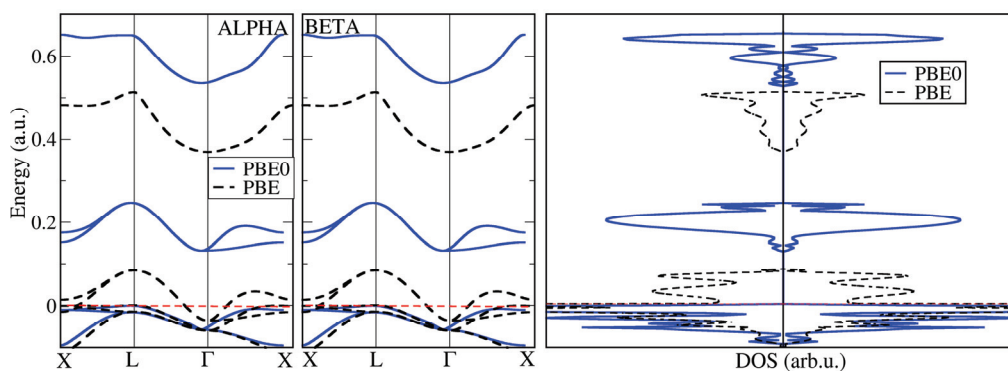


Figure S2. Comparison of band structure and DOS of FeO with PBE and PBE0 functional, red dashed line is Fermi level which is set to zero, blue curves are calculated result with PBE0 and dotted curves are calculated with PBE.

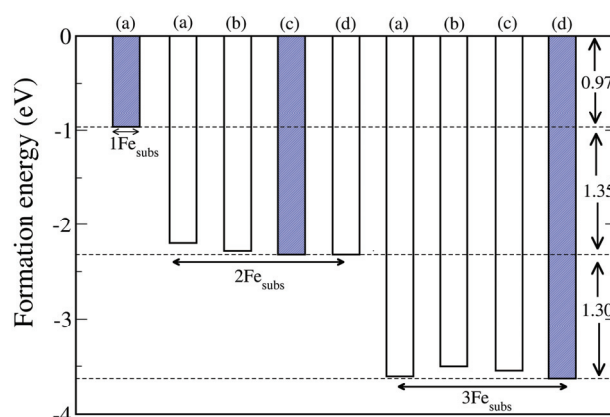


Figure S3 Calculated formation energies of Fe-ZnO NPs ($1Fe_{subs}$, $2Fe_{subs}$ and $3Fe_{subs}$). Only the open shell case was considered. The blue bar is most stable case.

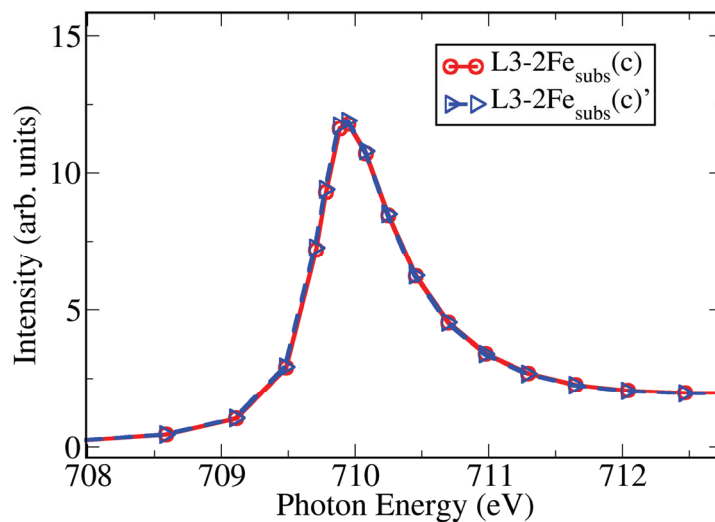


Figure S4. Comparison of calculated L3-XANES between $2Fe_{\text{subs}}(c)$ with $2Fe_{\text{subs}}(c)'$, $2Fe_{\text{subs}}(c)$ in red curve and $2Fe_{\text{subs}}(c)'$ in blue curve. The $2Fe_{\text{subs}}(c)'$ is the ZnO lattice with two Fe-Zn substitutions (frozen geometry). The structural information is given in Table S3.

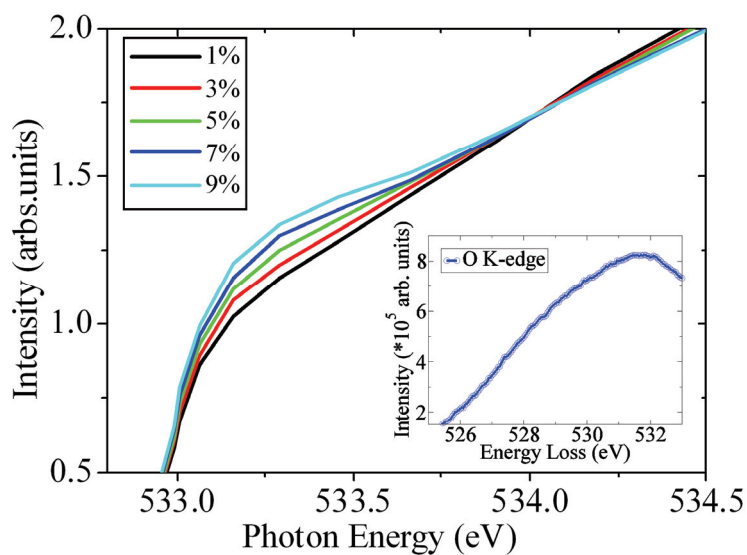


Figure S5. Comparison between calculated K-XANES of neighbor O around Fe in ZnO system with the content of Fe^{3+} , 1%, 3%, 5%, 7% and 9% ($2Fe_{\text{subs}}-Zn_{\text{vac}}(b)$), respectively, and experimental measurements in inset curve.

Table S1. Calculated formation energies of Fe-ZnO NPs ($1Fe_{subs}$, $2Fe_{subs}$ and $3Fe_{subs}$) with closed and open shell cases (eV).

	$1Fe_{subs}$	$2Fe_{subs}(a)$	$2Fe_{subs}(b)$	$2Fe_{subs}(c)$	$2Fe_{subs}(d)$	$3Fe_{subs}(a)$	$3Fe_{subs}(b)$	$3Fe_{subs}(c)$	$3Fe_{subs}(d)$
Closed shell	1.94	3.52	3.49	3.45	3.20	2.34	5.18	4.60	6.03
Open shell	-0.97	-2.28	-2.20	-2.32	-2.32	-3.61	-3.50	-3.55	-3.62

Table S2. Calculated lattice parameters (in Å and in °) in composite defects $2Fe_{subs}-Zn_{vac}$ and $2Fe_{subs}-O_{int}$ compared with Fe-substitution ($2Fe_{subs}$). The formation (E_f) and alloying energies (E_{all}), given in eV, are calculated according to Equations 1 and 2, respectively.

	$2Fe_{subs}$				$2Fe_{subs}-Zn_{vac}$				$2Fe_{subs}-O_{int}$				ZnO
	<i>a</i>	<i>b</i>	<i>c</i>	<i>d</i>	<i>a</i>	<i>b</i>	<i>c</i>	<i>d</i>	<i>a</i>	<i>b</i>	<i>c</i>	<i>d</i>	
<i>a</i>	6.50	6.56	6.52	6.52	6.52	6.52	6.51	6.55	6.46	6.58	6.58	6.54	6.50
<i>b</i>	6.51	6.48	6.48	6.48	6.51	6.51	6.51	6.53	6.54	6.56	6.50	6.51	6.50
<i>c</i>	10.35	10.36	10.36	10.36	10.22	10.25	10.23	10.14	10.54	10.37	10.54	10.42	10.34
α	89.36	89.3	90.0	90	89.9	90.3	90.0	90.2	90.9	90.2	88.8	90.1	90.0
β	90.5	90.0	89.5	89.5	89.8	90.0	90.0	90.0	90.0	90.0	90.0	90.0	90.0
γ	120.0	119.7	119.8	119.8	120.2	120.0	120.0	119.9	119.9	120.1	120.4	120.0	120.0
E_{all}/E_f	-2.28	-2.20	-2.32	-2.32	-1.30	-1.41	-0.97	-1.30	-0.77	-0.28	-0.26	0.88	-3.67

Table S3 Calculated lattice parameters (in Å and °) in Fe-ZnO NPs ($1Fe_{subs}$, $2Fe_{subs}$ and $3Fe_{subs}$) compared with ZnO wurtzite phase.

	1Fe dopant	2Fe dopants				3Fe dopants				ZnO
	$1Fe_{subs}$	$2Fe_{subs}(a)$	$2Fe_{subs}(b)$	$2Fe_{subs}(c)$	$2Fe_{subs}(d)$	$3Fe_{subs}(a)$	$3Fe_{subs}(b)$	$3Fe_{subs}(c)$	$3Fe_{subs}(d)$	
<i>a</i>	6.51	6.50	6.56	6.52	6.52	6.49	6.54	6.55	6.50	6.50
<i>b</i>	6.50	6.51	6.48	6.48	6.48	6.50	6.49	6.58	6.49	6.50
<i>c</i>	10.37	10.35	10.36	10.36	10.36	10.32	10.33	10.34	10.31	10.34
α	90.0	89.36	89.3	90.0	90	89.7	89.1	89.7	90.7	90.0
β	89.8	90.5	90.0	89.5	89.5	90.3	90.0	89.8	89.7	90.0
γ	119.9	120.0	119.7	119.8	119.8	119.6	120.2	120.2	119.5	120.0

APPENDIX B:

Fe-doped ZnO Nanoparticles: The iron oxidation number and local charge studied by ⁵⁷Fe Mößbauer spectroscopy and DFT,

Chem. Eur. J, 2013 (19), 3287-3291,

J. Xiao, A. Kuc, S. Pokhrel, L. Mädler, R. Pöttgen, F. Winter,

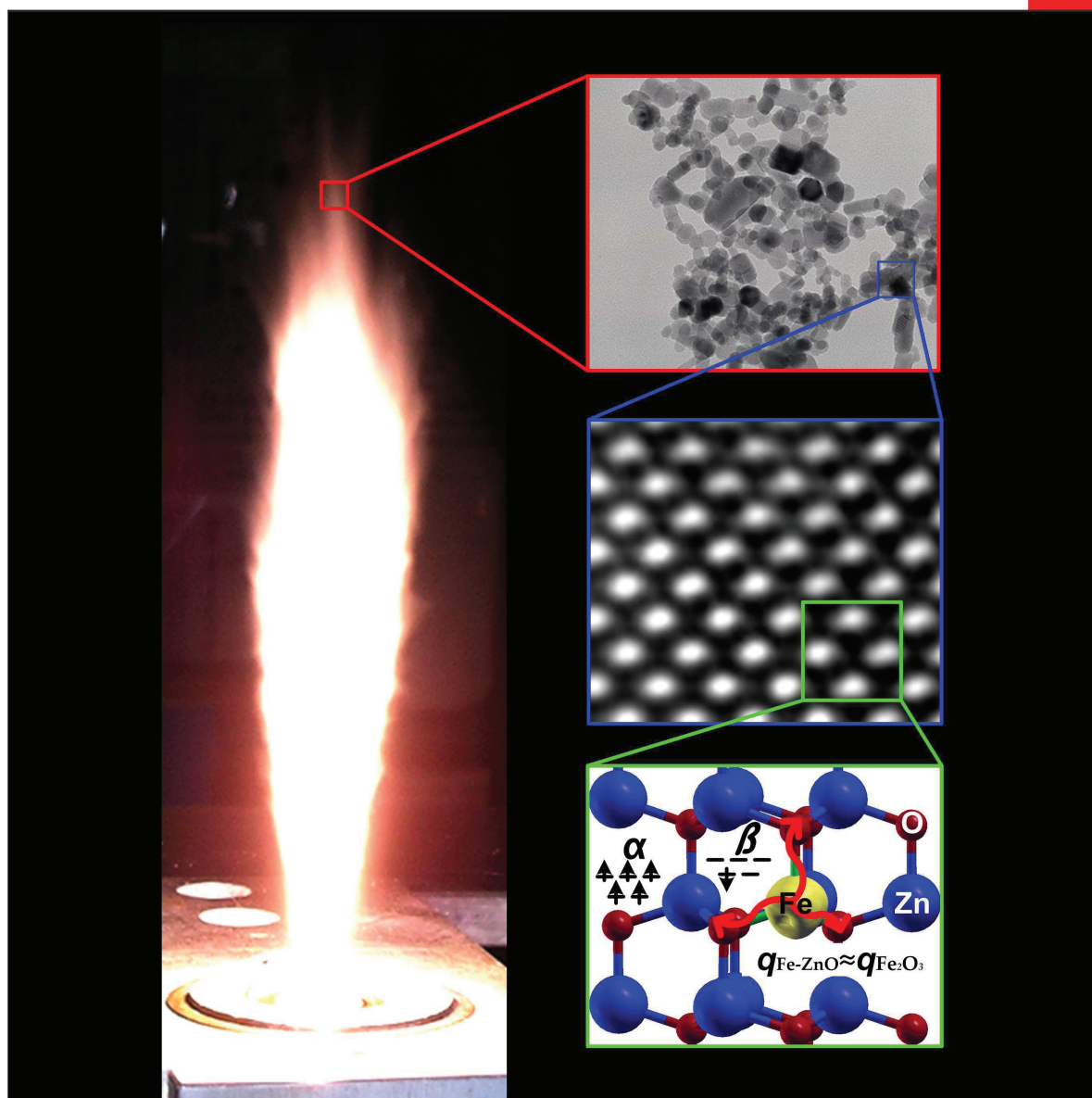
*T. Frauenheim and T. Heine**

CHEMISTRY

A EUROPEAN JOURNAL

19/10

2013



Concept

Catalytic Activation of Olefins by Metal Triflates and Triflimides:
Application to Fragrance Chemistry
E. Duñach and G. Lemière

WILEY-VCH

A Journal of



ChemPubSoc
Europe

Supported by
ACES

Fe-Doped ZnO Nanoparticles: The Oxidation Number and Local Charge on Iron, Studied by ^{57}Fe Mößbauer Spectroscopy and DFT Calculations

Jianping Xiao,^[a, b] Agnieszka Kuc,^[a] Suman Pokhrel,^[c] Lutz Mädler,^[c] Rainer Pöttgen,^[d] Florian Winter,^[d] Thomas Frauenheim,^[b] and Thomas Heine*^[a]

Mößbauer spectroscopy is a very valuable analytical tool that is based on the recoil-free resonance fluorescence of γ -photons^[1] in matter with Mößbauer-active elements, such as Fe. It is also one of the few techniques that is able to investigate electric monopole interactions on the resonant nucleus through hyperfine interactions.^[2] The sensitivity of the Coulomb charge interaction is due to the fact that the hyperfine interactions are seen by the method in two different nuclear states. The Mößbauer spectroscopy isomer shift (IS) is an important parameter that arises from the nuclear-energy shift that is caused by the Coulombic interaction between the nucleus and the electron density at the site of the nucleus. Because the valence state is always assumed to be tightly correlated with the charge density at the nucleus, the measured IS is often employed to determine the valence state of the embedded Fe element.^[3] In pure oxides, the upper limit of IS values for Fe^{3+} in tetrahedral coordination is around 0.25 mms^{-1} , whereas the lower limit for Fe^{3+} in octahedral coordination is approximately 0.29 mms^{-1} .^[4] In the case of Fe^{2+} , IS values within the range $1.20 > \text{IS} > 1.05 \text{ mms}^{-1}$ are generally attributed to the octahedron and IS values within the range $1.05 > \text{IS} > 0.90 \text{ mms}^{-1}$ are attributed to tetrahedral coordination.^[3] Hence, the IS values of Fe^{2+} and Fe^{3+} are significantly distinct from each other and Mößbauer spectroscopy has been generally accepted as the method of choice to determine the oxidation number.^[3] Although the IS values predictably decrease with increasing electron density at the nucleus, to the best of our knowl-

edge, IS signals close to approximately 0.3 mms^{-1} for Fe^{2+} in pure oxides have not yet been observed.

Recently, George et al.^[5] synthesized Fe-doped ZnO nanoparticles (Fe-ZnO NPs) with flame-spray pyrolysis (FSP); Fe concentrations of 10 atom % in ZnO NPs have been achieved without significant deformation of the ZnO structure. The Fe-ZnO NPs have been thoroughly characterized by TEM imaging, X-ray diffraction (XRD), and elemental mapping techniques. These results indicate that Fe is homogeneously distributed throughout the ZnO NPs with almost unchanged lattice parameters, without Fe-containing secondary phases. Furthermore, we have performed density functional theory (DFT) calculations to study the X-ray absorption near-edge structure (XANES) of the Fe and O elements, in comparison with experimental inner-shell electron-energy-loss spectroscopy (ISEELS). This comparison indicates that Fe^{2+} is predominantly present in the Fe-ZnO NPs,^[6] consistent with our DFT-based stability calculations, in which Fe^{2+} was found to be more stable than Fe^{3+} , and that Fe may substitute Zn directly at its lattice site without showing any structural defects. This result appears to be in contradiction to Fe-doped bulk ZnO, in which Fe has been reported to occur within domains and with the oxidation state III.^[7]

To resolve this apparent contradiction, we measured the Mößbauer IS for Fe in our Fe-ZnO NPs and compared the results with literature values of known phases that contained Fe^{2+} and Fe^{3+} . Our Fe-ZnO samples revealed an Fe-IS signal of 0.3 mms^{-1} , which was subjected to a quadrupole splitting (QS) of 0.83 mms^{-1} (Figure 1). At first sight, these values point to the presence of ionically bonded Fe^{3+} ,^[1] underlined by the IS values of 0.9 mms^{-1} for FeO ^[2] and 0.37 mms^{-1} for Fe_2O_3 ,^[2] which is in contradiction with our previous ISEELS analysis, reported in ref. [6].

Herein, by careful theoretical analysis of the electronic structure of the systems and by calculation of the Mößbauer IS and QS of doped Fe-ZnO nanoparticles, FeO, and Fe_2O_3 on the grounds of DFT calculations, we will show that this signal can indeed be attributed to Fe^{2+} within a ZnO matrix. We will demonstrate that, whilst the Mößbauer IS is related to the charge on the ion in the structure, there is not necessarily a correlation with its oxidation state. Hence, the Mößbauer IS cannot serve as a necessary determinant of the oxidation number of dopant atoms.

[a] M. Sc. J. Xiao, Dr. A. Kuc, Prof. Dr. T. Heine
School of Engineering and Science
Jacobs University Bremen
28759 Bremen (Germany)
E-mail: t.heine@jacobs-university.de

[b] M. Sc. J. Xiao, Prof. Dr. T. Frauenheim
Bremen Center for Computational Materials Science
Universität Bremen
28359 Bremen (Germany)

[c] Dr. S. Pokhrel, Prof. Dr.-Ing. L. Mädler
IWT Foundation Institute of Materials Science
Department of Production Engineering, Universität Bremen
28359 Bremen (Germany)

[d] Prof. Dr. R. Pöttgen, Dipl.-Chem. F. Winter
Institut für Anorganische und Analytische Chemie
Universität Münster
48149 Münster (Germany)

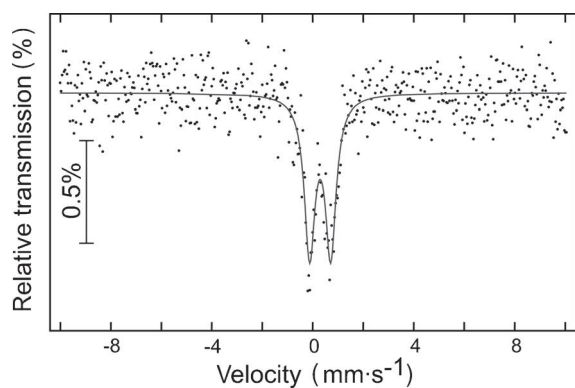
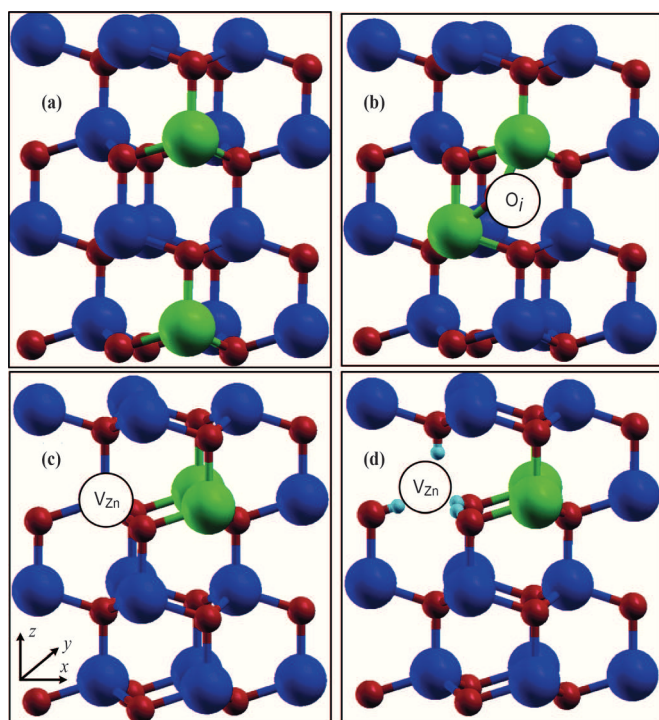


Figure 1. Mößbauer spectrum of Fe-doped ZnO NPs at 78 K. We have used the same samples as discussed in ref. [6].

We now consider two pure oxide phases, FeO and Fe₂O₃, in addition to a variety of model structures that might be expected in Fe-doped ZnO, as discussed below (Scheme 1).^[6]



Scheme 1. Fe-doped ZnO models of: a) Fe²⁺ (Fe_{Zn}) sites, b) Fe³⁺ (Fe_{Zn}+O_i) sites, c) Fe³⁺ (Fe_{Zn}+V_{Zn}) sites, and d) hydrogen-saturated V_{Zn} (Fe_{Zn}+V_{Zn}+nH, n=1–4) sites in ZnO NPs. The Zn, O, Fe, and H atoms are denoted by blue, red, green, and cyan spheres, respectively.

We define the oxidation number of Fe sites by analyzing the electronic structure at local sites, that is, by counting the electrons in the occupied Fe 3d orbitals. A d⁶ occupation indicates Fe²⁺ sites, whereas d⁵ occupation is compatible with Fe in oxidation state III. The Mößbauer IS of the Fe sites are calculated by using DFT (see the Computational Details section).

Figure 2 shows the projected electronic density-of-states (P-DOS) for Fe 3d orbitals in three exemplary Fe-doped ZnO models. As expected, for the Fe_{Zn} model, in which Zn lattice sites are substituted with Fe (Scheme 1 a), we observe

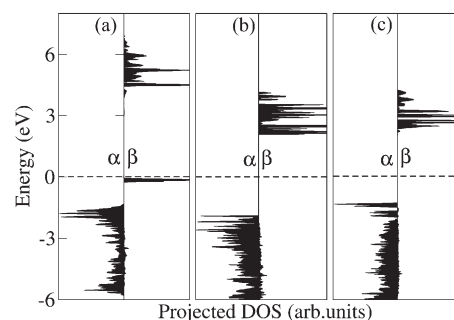


Figure 2. Projected DOS of Fe 3d orbitals in ZnO, which are represented in terms of the α and β spin of a) Fe²⁺ in Fe_{Zn}, b) Fe³⁺ in Fe_{Zn}+V_{Zn}, and c) Fe³⁺ in Fe_{Zn}+O_i. The energy scale is given with respect to the Fermi level (dashed line).

the d⁶ electronic configuration that characterizes this site as Fe²⁺ (Figure 2 a). Again, as expected, two models that should represent Fe³⁺, that is, the zinc vacancy (Fe_{Zn}+V_{Zn}) and interstitial oxygen (Fe_{Zn}+O_i; Scheme 1 b), have d⁵ occupation (Figure 2 b, c).

Table 1 shows the Mößbauer ISs for these models compared to the pure iron-oxide phases. Our results for the pure phases reproduce the measured^[2] and other calculated values^[8] very well. All of the model structures that incorporate Fe³⁺ sites, as determined from the Fe 3d occupation, show IS values that are close to the expected values for Fe³⁺. Surprisingly, the substitutional Fe site, which we identified as Fe²⁺ according to its d⁶ occupation, shows an IS of 0.3 mm s⁻¹, well within the range that is usually assigned as Fe³⁺ nuclei, but also very close to the measured IS for our Fe-doped ZnO NPs (Figure 1). Apparently, Mößbauer IS cannot be related to the oxidation number in the case of doped oxides.

Mößbauer spectroscopy directly probes the charge on the nucleus site. Evidently, this charge is sensitive to the local

Table 1. Calculated Mößbauer isomer shifts (IS) and quadrupole splitting (QS) of Fe²⁺ in FeO (rocksalt phase) and Fe³⁺ in Fe₂O₃ (corundum phase), as well as Fe-doped ZnO models, by using the PBE0 functional, with respect to body-centered cubic bulk Fe. Available literature values for pure oxides are given in parentheses.^[a]

System	IS [mm s ⁻¹]	QS [mm s ⁻¹]
FeO	0.90 (0.90, 0.81) ^[b]	0.32
Fe ₂ O ₃	0.32 (0.37, 0.37) ^[b]	1.40
Fe _{Zn}	0.33	0.81
Fe _{Zn} +V _{Zn}	0.32	1.91
Fe _{Zn} +O _i	0.25	2.50
Fe _{Zn} +V _{Zn} +1H	0.36	1.65
Fe _{Zn} +V _{Zn} +2H	0.36	1.81
Fe _{Zn} +V _{Zn} +3H	0.56	2.74
Fe _{Zn} +V _{Zn} +4H	0.82	4.44

[a] The nuclear constant was referenced to -0.25 a.u.³ mm s⁻¹; see reference [8]. [b] Values of FeO and Fe₂O₃ are taken from references [2, 8].

environment of the atom, both structurally and chemically. In Figure 3, the change in the Mößbauer IS is plotted as function of the Fe–O bond length in FeO and Fe₂O₃. The unperturbed pure FeO crystal has Fe–O distances of

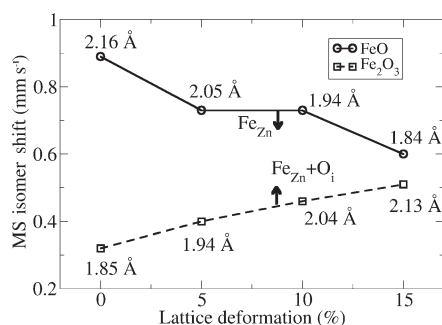


Figure 3. Calculated Mößbauer isomer shift of Fe sites in FeO and Fe₂O₃ with respect to uniform expansion (Fe₂O₃) or compression (FeO) of the lattice. Equilibrium geometries refer to 0% lattice deformation. Fe–O distances are indicated for the individual data points; the positions of the arrows mark the Fe–O bond length of Fe_{Zn} (pointing down) and Fe_{Zn}+O_i (pointing up) in Fe-doped ZnO.

2.16 Å,^[9] whereas, in pure unperturbed Fe₂O₃, the Fe–O bond is about 10% shorter (1.85 Å for corundum-Fe₂O₃). Next, we uniformly compressed the FeO and expanded the Fe₂O₃ lattices and monitored the Mößbauer IS values. Both phases showed the expected increase in IS upon expansion, roughly by 0.1 mm s⁻¹ per 5% bond stretching. At about 15% lattice deformation in both phases, FeO and Fe₂O₃ showed very similar Mößbauer signals. Indeed, the predicted Fe–O bond lengths for our doped Fe–ZnO nanoparticle models correspond to about 8% compressed FeO or about 8% stretched Fe₂O₃. Quantitatively, the IS of Fe²⁺ in the FeO structure decreases to 0.73 mm s⁻¹ with shortening of the Fe–O bond length to 1.97 Å. When the Fe–O bond length is elongated to 2.00 Å, the IS value of Fe³⁺ in Fe₂O₃ increases significantly up to 0.43 mm s⁻¹, thus showing a strong sensitivity towards the local crystal structure. Obviously, those IS values cannot be observed for the pure oxides, because they would be destroyed by such strong deformations. However, such deformed bond lengths are present in our Fe-doped ZnO models, for which we have recently shown that solid solutions of Fe in ZnO exhibit extraordinary stability.^[6]

The difference in the IS values is attributed to the electron density at the nucleus. There should be a direct linear relationship between that value and the charge on the ion in the structure. We calculated the Bader charges^[10] on Fe²⁺ and Fe³⁺ in ZnO to compare with those in the FeO and Fe₂O₃ phases. One critical and surprising finding was that the Bader charge on Fe²⁺ in the ZnO NPs was close to that on Fe³⁺ in Fe₂O₃, rather than to that of Fe²⁺ in FeO. To ensure the reliability of our explanation, we further investigated a series of Fe_{Zn}+V_{Zn}-based models (Scheme 1d), namely, Fe_{Zn}+V_{Zn} models with certain hydrogen-saturation V_{Zn} sites (Fe_{Zn}+V_{Zn}+nH, n=1–4), to mimic the reduction

process of Fe³⁺ into Fe²⁺ in ZnO NPs. The Bader charges are linearly correlated with the IS values, similar to the correlation between the IS values and the electron density at the nucleus (Figure 4). This result indicates that there are

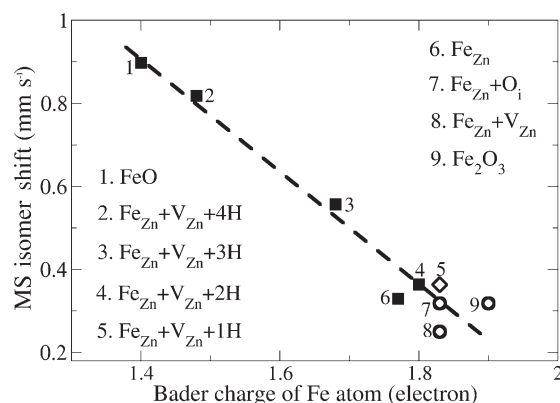


Figure 4. Correlation between the calculated Mößbauer isomer shift and the Bader charge on the Fe sites; ○ denote Fe³⁺ (d⁵), ■ denote Fe²⁺ (d⁶), and ◇ denotes a mixture of Fe²⁺ (d⁶) and Fe³⁺ (d⁵) species.

significant changes in atomic charge (Bader charge) and electron density at the nucleus (IS) for Fe in these models. However, we would emphasize that the valence state of the Fe element in the Fe_{Zn}+V_{Zn}+nH (n=2–4) models does not change at all. This result confirms the fact that the Mößbauer IS depends on the charge at the nucleus, but not on the electron distribution over the ionic states, that is, on the valence state or on the oxidation number of Fe in Fe-doped ZnO NPs. A similar correlation is known in metal–organic chemistry, for example, for organic {Fe₄S₄}ⁿ⁺ complexes.^[11]

The Mößbauer QS reflects the interactions between the nuclear-energy levels and the surrounding electric-field gradient (EFG). We calculated the QS of these Fe_{Zn}, Fe_{Zn}+V_{Zn}, and Fe_{Zn}+O_i models by referring to the nuclear quadrupole moment of 0.16 barn.^[12] It is evident that the QS provides more details to distinguish between the different doping sites of Fe in a ZnO matrix, because their values differ by about 4 mm s⁻¹ compared to about 0.5 mm s⁻¹ for the IS. The calculated QS splitting in the Fe_{Zn} model (about 0.81 mm s⁻¹) is in excellent agreement with our measured value of 0.83 mm s⁻¹. However, the calculated QS of the Fe_{Zn}+V_{Zn} and Fe_{Zn}+O_i models are 1.90 mm s⁻¹ and 2.50 mm s⁻¹, respectively. We can now confirm, with comprehensive evidence, through Mößbauer IS and QS analysis, that the samples contain substitutional Fe²⁺ ions on the Zn²⁺ positions of the wurtzite structure.

In summary, we have shown that the oxidation number can be probed by considering the electronic configuration of Fe cations in solid matrices. However, spectroscopic methods, such as Mößbauer spectroscopy, that relate to the electron density at the nucleus or the ionic charge are not adequate for determining the oxidation number in mixed phases as in Fe-doped ZnO. A joint experimental/theoretical Mößbauer IS and QS analysis, as presented herein, is a pow-

erful tool for distinguishing between the possible dopant sites of Fe in metal-oxide matrices.

The Mößbauer IS of 0.3 mms^{-1} and QS of 0.83 mms^{-1} for Fe in Fe-doped ZnO nanoparticles^[5,6] are compatible with the presence of substitutional doped Fe²⁺ ions in these phases. This result is caused by charge depletion on the ZnO matrix, supported by the compression of the Fe–O bond lengths of the tetrahedral Fe site in the wurtzite ZnO lattice.

Computational Details

All calculations of Mößbauer IS and QS were performed by using DFT (PBE0 functional) with the augmented plane wave plus local orbitals (APW+lo) method, as implemented in the WIEN2K code.^[13] In this method, the electronic wave functions are expanded in spherical harmonics inside non-overlapping atomic spheres of radius R_{MT} and in plane waves in the remaining interstitial region. The parameter $R_{\text{MT}}K_{\text{max}}$, which controls the size of the basis sets, was set to seven. The R_{MT} value of the Fe element was fixed at 1.80–1.81 for all models. The R_{MT} values for Zn, O, and H atoms were specified within the ranges 1.74–1.88, 1.11–1.60, and 0.60–0.64, respectively. The electronic wave functions within the interstitial regions were expanded in plane waves with a cutoff energy of 22 Ry. Electronic states that lay more than 7 Ry below the Fermi level were treated as the core states. The APW+lo method was employed for the valence electrons, because it allowed faster convergence at the same high level of accuracy as the LAPW+lo approach. For the valence states, relativistic effects were taken into account in a scalar relativistic treatment^[14] and core states were considered by a fully relativistic treatment.^[15]

For calibration calculations by using Fe, FeO, and Fe₂O₃, we fixed the lattice constant to the experimental value and only relaxed the internal atomic coordinates. The convergence of the quantities of interest (electron density at the nucleus) was checked with respect to the number of k points. The Brillouin zones of FeO and Fe₂O₃ oxides were sampled by a regular mesh that contained 40–80 irreducible k points, whereas, for metallic Fe, 200–600 irreducible k points were specified per Brillouin zone. Three DFT functionals of the generalized gradient approximation (GGA) level were considered to confirm the reliability and reproducibility of our calculations, namely, the Perdew–Burke–Ernzerhof (PBE),^[16] Wu–Cohen (WC),^[17] and Perdew et al. (PBE_sol) functionals.^[18] We chose the hybrid functional PBE0,^[19] in accordance with our calculations in ref. [6], because it provides an excellent description of electronic interactions. Further validation calculations included tests using the GGA+ U method, which incorporated explicit electron–electron correlation. With U values of 4–6 eV, we obtained almost-quantitative agreement for the IS. For the Fe–ZnO doped models, namely, Fe_{Zn}, Fe_{Zn}+V_{Zn}, Fe_{Zn}+O_i, and Fe_{Zn}+V_{Zn}+ n H ($n=1-4$), the Brillouin zones were sampled with 8–32 k points to confirm the convergence of electron density at the nucleus (Table 2).

Experimental Details

Metallorganic precursors, zinc naphthenate (8% Zn; Strem Chemicals, 99.9%) and iron naphthenate (12% Fe; Strem Chemicals, 99.9%) were used for the synthesis of Fe-doped ZnO nanoparticles by flame-spray pyrolysis (FSP). Briefly, a 0.5 M solution of zinc naphthenate in xylene (50 mL; Strem Chemicals, 99.95%) was mixed with 0.5 M solutions of iron naphthenate in xylene (0.6–6.5 mL) to provide 1–10 wt.% Fe doping. These precursors were dissolved in the organic solvent (xylene) to keep the metal concentration at 0.5 M. Each liquid precursor was delivered to the flame nozzle of the FSP reactor by using a syringe pump at a flow rate of 5 mL min^{-1} by atomizing the precursor solution with an O₂

Table 2. Validation calculations of the Mößbauer isomer shifts [mms^{-1}] by using different functionals and comparison with previously reported experimental and calculated values.

	PBE	WC	PBE_sol	PBE0	Exptl ^[a]	Calcd ^[b]
FeO	0.89	0.87	0.87	0.89	0.90	0.81
Fe ₂ O ₃	0.35	0.33	0.33	0.32	0.37	0.37

[a] See reference [2]. [b] See reference [8].

dispersant and by maintaining a pressure drop of 1.5 bar at the nozzle tip. Combustion of the dispersed droplets was initiated by the co-delivery of CH₄ and O₂ (1.5 L min^{-1} and 3.2 L min^{-1} , respectively) to create a flame.

A ⁵⁷Co/Rh source was used for the ⁵⁷Fe Mößbauer spectroscopic investigation. The sample was placed in a thin-walled poly(methyl methacrylate) (PMMA) container, which was sealed with an epoxy resin. The measurements were performed in the usual transmission geometry at 78 K. Fitting of the spectra was performed by using the NORMOS-90 program system. The spectrum was well-reproduced, with a single signal at $\delta=0.29(1) \text{ mms}^{-1}$, subjected to a QS of $\Delta E_0=0.83(1) \text{ mms}^{-1}$, and an experimental line-width parameter of $0.51(3) \text{ mms}^{-1}$. The IS refers to α -iron.

Acknowledgements

Financial support from the Chinese Scholarship Council (CSC) and the Deutsche Forschungsgemeinschaft (SPP 1613) is gratefully acknowledged. S.P. and L.M. thank the National Science Foundation and the Environmental Protection Agency under cooperative agreement number DBI-0830117. Key support was provided by the US Public Health Service (U19ES019528 (UCLA Center for NanoBiology and Predictive Toxicology), RO1ES016746, and RC2ES018766).

Keywords: density functional calculations • iron • Mößbauer spectroscopy • nanoparticles • zinc

- [1] a) E. Kuzmann, S. Nagy, A. Vértes, *Pure Appl. Chem.* **2003**, *75*, 801–858; b) Y.-L. Chen, D.-P. Yang, *Mössbauer Effect in Lattice Dynamics: Experimental Techniques and Applications*, Wiley-VCH, Weinheim, **2007**; c) P. Gülich, E. Bill, A. X. Trautwein, *Mössbauer Spectroscopy and Transition Metal Chemistry: Fundamentals and Applications*, Springer, Berlin, **2011**.
- [2] M. D. Dyar, D. G. Agresti, M. W. Schaefer, C. A. Grant, E. C. Sklute, *Annu. Rev. Earth Planet. Sci.* **2006**, *34*, 83–125.
- [3] E. Murad, J. H. Johnston in *Mössbauer Spectroscopy Applied to Inorganic Chemistry* (Ed.: G. J. Long), Plenum, New York, **1987**, pp. 507–582.
- [4] R. G. Burns, T. C. Solberg in *Spectroscopic Characterization of Minerals and Their Surfaces (Am. Chem. Soc. Symp. Ser.)* (Eds.: L. M. Coyne, D. F. Blake, S. W. S. McKeever), Oxford University Press, Oxford, **1998**, pp. 262–283.
- [5] S. George, S. Pokhrel, T. Xia, B. Gilbert, Z. Ji, M. Schowalter, A. Rosenauer, R. Damoiseaux, K. A. Bradley, L. Mädler, A. E. Nel, *ACS Nano* **2010**, *4*, 15–29.
- [6] J. Xiao, A. Kuc, S. Pokhrel, M. Schowalter, S. Porlapalli, A. Rosenauer, T. Frauenheim, L. Mädler, L. G. M. Pettersson, T. Heine, *Small* **2011**, *7*, 2879–2886.
- [7] F. Wolf, B. H. Freitag, W. Mader, *Micron* **2007**, *38*, 549–552.
- [8] A. M. Mudarra Navarro, C. E. R. Torres, L. A. Errico, *Hyperfine Interact.* **2011**, *202*, 117–121.
- [9] H. Fjellvag, F. Groenvold, S. Stoelen, B. C. Hauback, *J. Solid State Chem.* **1996**, *124*, 52–57.

- [10] R. F. W. Bader, *Atoms in Molecules: A Quantum Theory*, Clarendon Press, Oxford, **1994**.
- [11] F. Neese, *Inorg. Chim. Acta* **2002**, *337*, 181–192.
- [12] P. Dufek, P. Blaha, K. Schwarz, *Phys. Rev. Lett.* **1995**, *75*, 3545–3548.
- [13] a) E. Sjöstedt, L. Nordström, D. J. Singh, *Solid State Commun.* **2000**, *114*, 15–20; b) G. K. H. Madsen, P. Blaha, K. Schwarz, E. Sjöstedt, L. Nordström, *Phys. Rev. B* **2001**, *64*, 195134; c) K. Schwarz, P. Blaha, G. K. H. Madsen, *Comput. Phys. Commun.* **2002**, *147*, 71–76; d) P. Blaha, K. Schwarz, G. K. H. Madsen, K. Kvasnicka, J. Luitz, computer code WIEN2K, Vienna University of Technology, Vienna, **2001**.
- [14] D. D. Koelling, B. N. Harmon, *J. Phys. C* **1977**, *10*, 3107–3114.
- [15] J. P. Desclaux, *Comput. Phys. Commun.* **1970**, *1*, 216–222.
- [16] J. P. Perdew, S. Burke, M. Ernzerhof, *Phys. Rev. Lett.* **1996**, *77*, 3865–3868.
- [17] Z. Wu, R. E. Cohen, *Phys. Rev. B* **2006**, *73*, 235116.
- [18] J. P. Perdew, Z. Ruzsinszky, G. I. Csonka, O. A. Vydrov, G. E. Scuseria, L. A. Constantin, X. Zhou, K. Burke, *Phys. Rev. Lett.* **2008**, *100*, 136406.
- [19] C. Adamo, V. Barone, *J. Chem. Phys.* **1999**, *110*, 6158–6170.

Received: December 4, 2012
Published online: February 10, 2013

APPENDIX C:

Activation mechanism of carbon monoxide on α -Fe₂O₃(0001) surface studied by using first principle calculations,

App. Phys. Lett. 2012 (101), 041603,

J. Xiao and T. Frauenheim,*

Activation mechanism of carbon monoxide on α -Fe₂O₃ (0001) surface studied by using first principle calculations

Jianping Xiao^{1,2,a)} and Thomas Frauenheim¹

¹Bremen Center for Computational Materials Science, Universität Bremen, Am Fallturm 1, 28359 Bremen, Germany

²School of Engineering and Science, Jacobs University Bremen, Campus Ring 1, 28759 Bremen, Germany

(Received 9 May 2012; accepted 12 July 2012; published online 27 July 2012)

We have employed first principle methods to investigate carbon monoxide (CO) adsorption on oxygen terminated α -Fe₂O₃ (0001) surface. We have found that the CO can be adsorbed and oxidized as long as the CO surface coverage reaches up to two thirds monolayer. Simultaneously, the bent CO₂ are activated and dimerized. Furthermore, oxygen vacancy can dissociate water and produce carboxylic group by means of reactions with the activated CO₂ dimer. Our calculations have reproduced experimental *in situ* observations of nanocrystalline α -Fe₂O₃. In this letter, we also propose a significant strategy to improve reactivity of α -Fe₂O₃ (0001) continuous film, to convert more efficiently CO into organic species. © 2012 American Institute of Physics. [<http://dx.doi.org/10.1063/1.4739935>]

Carbon monoxide (CO) is a very toxic gas in the atmosphere. Catalytic oxidation of CO to carbon dioxide (CO₂) is a good solution to solve such serious environmental problem.¹ Currently, the oxidation process is catalyzed over noble metals, e.g., platinum and gold. However, the expensive cost of noble metals does not make it feasible any more in future.

On the other hand, activating CO₂ is a significant topic with fundamental and applied interests in heterogeneous catalytic chemistry, environmental, and electrochemistry.²⁻⁴ There were numerous investigations to activate CO₂ on metal-oxide surfaces^{5,6} and metal complexes.⁷ Transition metal surface, α -Fe₂O₃, appears to be an active catalytic material for producing styrene.⁸ This was then substantiated in terms of studying reactivity of single crystalline hematite model.⁹ Hence it renders an important issue to do fundamental studies for understanding physical and chemical properties of α -Fe₂O₃ surfaces.

For clean α -Fe₂O₃ (0001) surfaces, Wang *et al.*¹⁰ found that there are two distinct surfaces domains, namely, Fe-O₃-Fe and O₃-Fe-Fe (hereafter, we will use the same nomenclature as in the work of Wang *et al.*¹⁰). These terminations are stable in certain chemical potential of oxygen. Bergermayer *et al.*¹¹ had also obtained evidences with first principle thermodynamics calculations by considering temperature effects. In addition, Bergermayer *et al.* proposed another configuration of α -Fe₂O₃ surfaces with ferryl species. The theoretical prediction was also validated by the following experimental works.¹²

Recently, it has also been drawn attentions to obtain fundamental insight into the reactivity of the α -Fe₂O₃ surface. Deng *et al.*¹³ had investigated comparatively the reactivity of α -Fe₂O₃ nanocrystals and continuous films with *in situ* x-ray photoelectron spectroscopy. The continuous films behave inert under the same conditions studied for nanocrystalline α -Fe₂O₃. Neither adsorbed CO nor hydroxyl group was

observed on the continuous films in their experimental studies. The reactivity difference indicates there are not active sites on perfect oxygen terminated α -Fe₂O₃ (0001) surface.

In this letter, we have performed theoretical studies to interpret mechanism of relevant reactions on α -Fe₂O₃ nanocrystals and also propose efficient solutions to improve the reactivity of continuous α -Fe₂O₃ (0001) surface. The realistic α -Fe₂O₃ surfaces with adsorbates will exchange adsorbates with their chemical reservoirs. Therefore, we need to analyze Gibbs free energy and its dependence on chemical potentials of adsorbates. The chemical potential can be affected by partial pressure of CO molecules, as well as surface coverage. The studied surface coverage is in the range from one third monolayer (θ_1) to two thirds monolayer (θ_2) and single monolayer (θ_3). Ferromagnetic (FM), antiferromagnetic (AFM), and paramagnetic (PM) ordering of Fe cations were also assigned in studied models, respectively, as the same way as the work of Bergermayer *et al.*¹¹

We have employed the density functional theory (DFT) method implemented in CRYSTAL09 code,¹⁴ to perform static calculations (H: 5-11G*,¹⁵ C: 6-21G*,¹⁶ O: 6-31d,¹⁷ Fe: 86-411d,¹⁸ Perdew-Burke-Ernzerhof functional¹⁹). All calculations are performed with slab approaches, with surfaces modeled as an infinite and periodic thin slabs consisting of 18 atomic layers along [0001] direction. There are different terminations, namely, Fe and O, for perfect α -Fe₂O₃ (0001) surfaces. Hence, we have fixed partial atomic layers and only relaxed the first 6 layers on surface. The opposite Fe termination is passivated by hydrogen to avoid undesired electronic states. The Monkhorst-Pack scheme²⁰ grid (10 × 10 × 1) was utilized for k-sampling.

The relative energetic stability of the α -Fe₂O₃ (0001) surfaces with adsorbed molecules is determined by their respective binding energy, defined as $E_{binding} = [E_{tot} - E_{clean} - n\mu]/A$, where E_{tot} is the total energy of CO adsorbed surface, E_{clean} is the energy of clean Fe₂O₃ (0001) surfaces (O₃-Fe-Fe), μ is chemical potential of adsorbed CO molecule, which accounts for experimental conditions with different partial pressure of CO and some uncontrollable variable, and

^{a)}Electronic mail: xiao@bccms.uni-bremen.de. Tel.: +49 (0) 421 218 2886. Fax: +49 (0) 421 218 62770.

n is the number of adsorbed CO on studied surface area, A . In our case, A corresponds to the area of primitive (1×1) unit cell, which is also observed periodicity,⁹ containing three oxygen atoms in the first layer.

Furthermore, first principle molecular dynamics (MD) were performed to study thermal stability of adsorbate CO modified surfaces. We have employed projector augmented wave (PAW) formalism²¹ and Perdew-Burke-Ernzerhof functional¹⁹ implemented in the Vienna Ab-Initio Simulation Package (VASP).²² The vacuum space was specified with 30 \AA between two images. Initially, we ran couples of trials (NVE, $T = 0 \rightarrow 300 \text{ K}$) to get different initial configurations. Then, we performed calculations with these initial configurations (NVT, $T = 300 \text{ K}$) to equilibrate our simulated systems. The simulated systems were equilibrated within 2 ps with Nosé thermostat and a time step of 2 fs. The MD simulated results are comparable and reproducible with random assignment of initial velocity.

In Fig. 1, we show phase diagram of $\alpha\text{-Fe}_2\text{O}_3$ (0001) surfaces with different CO coverage and magnetic ordering of Fe cations. The chemical potential boundary (-0.15 eV) corresponds to chemical potential of CO in the condition of CO poor. In low CO content case (θ_1), the single CO molecule does not favor to be stably adsorbed on the $\text{O}_3\text{-Fe-Fe}$ surface. The weak binding (0.2 eV/\AA^2) could explain inert CO adsorption observed in experiment.¹³ However, as long as the CO surface coverage reaches up to two thirds monolayer (θ_2) (Fig. 1), the FM spin ordering becomes more preferable. Meanwhile, the two adjacent CO molecules are oxidized into CO_2 . Since the carbon-oxygen bonds are unsaturated (Fig. 2(b)), it results in an additional carbon-carbon covalent bond formed and bent CO_2 dimer. Hence, the binding energy (0.8 eV/\AA^2) is much stronger in comparison with the case of low CO surface coverage (θ_1). Wang *et al.*⁶ had observed similar activation mechanism of CO_2 on ZnO (1010) surface with tridentate surface carbonate. This reveals

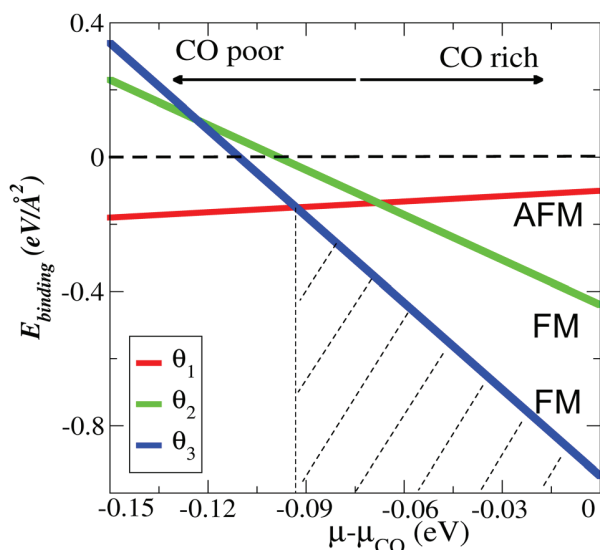


FIG. 1. Phase diagram of $\alpha\text{-Fe}_2\text{O}_3$ (0001) surfaces with different CO surface coverage (θ_1 : one third monolayer, θ_2 : two thirds monolayer, and θ_3 : single monolayer) and different magnetism (FM: ferromagnetic, AFM: antiferromagnetic). The black and bold dashed line is to note clean surface. The shadow area is proposed to activate CO on $\alpha\text{-Fe}_2\text{O}_3$ (0001) surface.

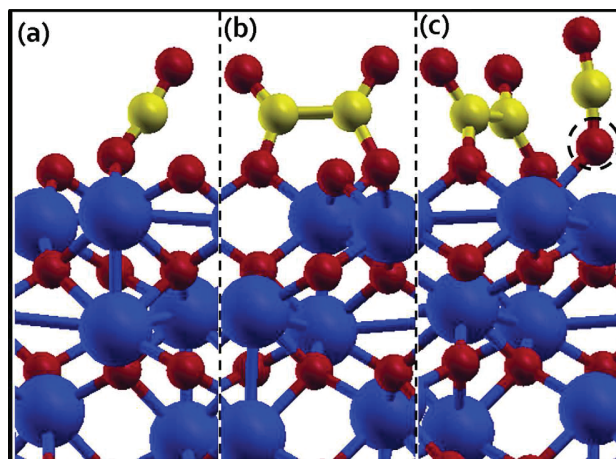


FIG. 2. Configurations of adsorbed CO on $\alpha\text{-Fe}_2\text{O}_3$ (0001) surfaces with all studied coverage (a) one third monolayer (θ_1), (b) two thirds monolayer (θ_2), and (c) single monolayer (θ_3). The V_O site is clarified by dashed circle. Fe: blue, O: red, C: yellow.

that bending CO_2 is a significant approach in heterogeneous catalytic chemistry to activate CO_2 molecule. Further, we have also obtained similar bent CO_2 dimer (Fig. 2(c)) in the single monolayer CO coverage (θ_3). However, the experimental work found inert continuous films of $\alpha\text{-Fe}_2\text{O}_3$ (0001) surfaces with experimental pressure of 200 mTorr and temperature up to 466 K.¹³ According to our calculations, we would propose that CO molecules can be adsorbed and activated on $\alpha\text{-Fe}_2\text{O}_3$ (0001) surface in higher CO pressure, to increase probability of CO_2 dimerization, as well as lower temperature to reduce desorption of CO molecules.

In order to convert activated CO_2 dimer into organic species, on the one hand, it requires to adsorb other organic species in the vicinity. Thus, we need to activate oxygen site next to CO_2 dimer. On the other hand, the thermal stability could propose us experimental temperature. Thus, we carried out further MD simulations to study thermal stability of all studied surface configurations.

We have found CO_2 emission in the low CO surface coverage (θ_1). The adsorbed CO molecule is oxidized by $\text{O}_3\text{-Fe-Fe}$ surface and desorbs in the form of CO_2 monomer at room temperature (300 K). The results are reproducible with random assignment of initial velocity in all MD simulations. Thus, an oxygen vacancy (V_O) can be created by CO_2 emission. In contrast, there is significantly distinct that the adsorbed CO could form extremely stable bent CO_2 dimer (Fig. 2(b)) in the higher CO surface coverage cases (θ_2 and θ_3). For the single monolayer (θ_3) case, the MD simulations indicate it is a simple combination of CO_2 monomer (θ_1) and CO_2 dimer (θ_2). This is also consistent with our static DFT calculations. We have also observed oxidation of CO monomer and CO_2 emission. Thus, the most interesting finding is that an active defect (V_O) can be easily created in the vicinity of CO_2 dimer at room temperature (Fig. 2(c)). The perfect $\alpha\text{-Fe}_2\text{O}_3$ (0001) surface is a typical polar surface proposed by Tasker²³ (Tasker type 3). There is nonzero macroscopic dipole moment perpendicular to the surface. The macroscopic dipole moment destabilizes intensively the $\alpha\text{-Fe}_2\text{O}_3$ (0001) surface. The defects (V_O) formation on surface can efficiently cancel the macroscopic dipole moment and

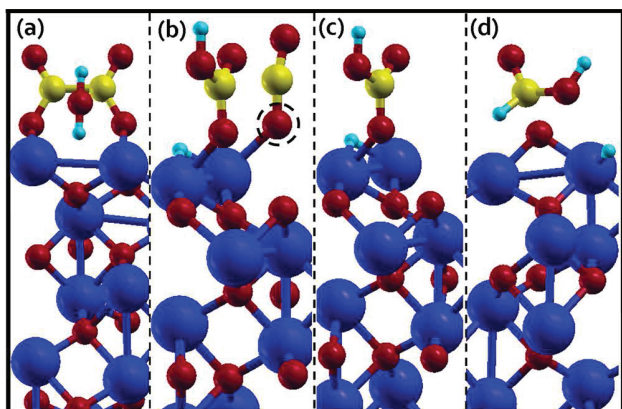


FIG. 3. α -Fe₂O₃ (0001) surfaces with (a) water adsorbed on V_O site, (b) dissociated water, (c) CO₂ monomer emission, and (d) desorbed formic acid. The V_O site is clarified by dashed circle. Fe: blue, O: red, C: yellow, H: green.

stabilize surface.²⁴ This can explain rationality of our simulated results.

Water is the most usual candidate to react with activated CO₂ dimer in order to produce carboxyl. We have found the adsorbed water can be dissociated by oxygen vacancy (Fig. 3(b)). This is exactly consistent with the experimental work of Deng *et al.*¹³ In addition, we have found the desired carboxyl species formed on the α -Fe₂O₃ surface. The adsorbed formate group was also detected in the experiment with *in situ* x-ray photoelectron spectroscopy.¹³ Furthermore, the CO₂ monomer in Fig. 3(b) is produced accompanying with water dissociation. The stability of the CO₂ monomer should be similar to that in Fig. 2(c). The MD simulations have also validated our expectations. Thus, one could create further active site in the vicinity of carboxyl group.

In summary, we have investigated the CO adsorbed on oxygen terminated α -Fe₂O₃ (0001) surface. The CO molecules are oxidized and activated in the form of bent CO₂ dimer. An oxygen vacancy can be created by releasing CO₂ monomer at room temperature (300 K). The oxygen vacancy can dissociate water and generate carboxyl group. The reactivity of the oxygen vacancy was validated in the previous experiment, where both adsorbed hydroxyl and carboxyl

groups were detected. Thus, there are similar mechanisms of chemical reactions for nanocrystals and continuous films. Our theoretical work can propose a strategy to improve reactivity of α -Fe₂O₃ continuous film.

J.X. would acknowledge financial support by the Chinese Scholarship Council (CSC) and computational resources of hardware and software supported by Bremen Center for Computational Materials Science, Universität Bremen.

¹K. S. A. Halim, M. H. Khedr, M. I. Nasr, and A. M. El-Mansy, *Mater. Res. Bull.* **42**, 731 (2007).

²H.-J. Freund and M. W. Roberts, *Surf. Sci. Rep.* **25**, 225 (1996).

³F. Solymosi, *J. Mol. Catal.* **65**, 337 (1991).

⁴S. Schenk, J. Notni, U. Köhn, K. Wermann, and E. Anders, *Dalton Trans.* **35**, 4191 (2006).

⁵H. Noei, C. Wöll, M. Muhler, and Y. Wang, *J. Phys. Chem. C* **115**, 908 (2011).

⁶Y. Wang, R. Kováčik, B. Meyer, K. Kotsis, D. Stodt, V. Staemmler, H. Qiu, F. Tranziska, D. Langenberg, M. Muhler, and C. Wöll, *Angew. Chem. Int. Ed.* **46**, 5624 (2007).

⁷A. Behr, *Carbon Dioxide Activation by Metal Complexes* (Verlag Chemie, Weinheim, Germany, 1988).

⁸T. Hirano, *Appl. Catal.* **26**, 81 (1986).

⁹W. Weiss, D. Zscherpel, and R. Schlögl, *Catal. Lett.* **52**, 215 (1998).

¹⁰X.-G. Wang, W. Weiss, Sh. K. Shaikhutdinov, M. Ritter, M. Petersen, F. Wagner, R. Schlögl, and M. Scheffler, *Phys. Rev. Lett.* **81**, 1038 (1998).

¹¹W. Bergermayer, H. Schweiger, and E. Wimmer, *Phys. Rev. B* **69**, 195409 (2004).

¹²C. Lemire, S. Bertarione, A. Zecchina, D. Scarano, A. Chaka, S. Shaikhutdinov, and H.-J. Freund, *Phys. Rev. Lett.* **94**, 166101 (2005).

¹³X. Deng, J. Lee, C. Wang, C. Matranga, F. Aksoy, and Z. Liu, *J. Phys. Chem. C* **114**, 22619 (2010).

¹⁴R. Dovesi, V. R. Saunders, C. Roetti, R. Orlando, C. M. Zicovich-Wilson, F. Pascale, B. Civalleri, K. Doll, N. M. Harrison, I. J. Bush, Ph. D'Arco, and M. Llunell, *CRYSTAL09, User's Manual* (University of Torino, Torino, 2009).

¹⁵R. Dovesi, E. Ermondi, E. Ferrero, C. Pisani, and C. Roetti, *Phys. Rev. B* **29**, 3591 (1983).

¹⁶M. Catti, A. Pavese, R. Dovesi, and V. C. Saunders, *Phys. Rev. B* **47**, 9189 (1993).

¹⁷C. Gatti, V. R. Saunders, and C. Roetti, *J. Chem. Phys.* **101**, 10686 (1994).

¹⁸M. Catti, G. Valerio, and R. Dovesi, *Phys. Rev. B* **51**, 7441 (1995).

¹⁹J. P. Perdew, K. Burke, and M. Ernzerhof, *Phys. Rev. Lett.* **77**, 3865 (1996).

²⁰H. J. Monkhorst and J. D. Pack, *Phys. Rev. B* **13**, 5188 (1976).

²¹P. E. Blöchl, *Phys. Rev. B* **50**, 17953 (1994).

²²G. Kresse and D. Joubert, *Phys. Rev. B* **59**, 1758 (1999).

²³P. W. Tasker, *J. Phys. C: Solid State Phys.* **12**, 4977 (1979).

²⁴C. Noguera, *J. Phys.: Condens. Matter* **12**, 367 (2000).

APPENDIX D:

*Activity and Synergy Effects on a Cu/ZnO(0001) Surface Studied Using First-
Principle Thermodynamics,*

J. Phys. Chem. Lett. 2012 (3), 2638-2642,

J. Xiao and T. Frauenheim,*

Activity and Synergy Effects on a Cu/ZnO(0001) Surface Studied Using First-Principle Thermodynamics

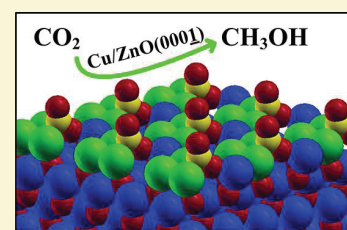
Jianping Xiao^{*,†,‡} and Thomas Frauenheim[†]

[†]Bremen Center for Computational Materials Science, Universität Bremen, Am Fallturm 1, 28359 Bremen, Germany

[‡]School of Engineering and Science, Jacobs University Bremen, Campus Ring 1, 28759 Bremen, Germany

S Supporting Information

ABSTRACT: Using first-principle thermodynamics, we have studied surface phase diagrams of Cu substitutional ZnO(0001) surfaces under industrial conditions. On the one hand, the Cu substituted on Zn sites can promote efficient formation of oxygen vacancies on the ZnO(0001) surface. It can improve the activity on the Cu/ZnO(0001) surface. On the other hand, metallic monolayers containing certain Cu and Zn atoms can be also formed, accompanied by the oxygen vacancies formation. We have further investigated CO₂ adsorption and reduction on these metallic monolayers. These metallic monolayers prefer to have an intermediate binding strength with the CO₂ molecule. The intermediate binding strength was expected to be optimized for subsequent CO₂ reduction. We have performed further studies and demonstrated successfully the improved catalysis for the subsequent CO₂ reduction on these metallic monolayers. The relevant mechanism can be interpreted with the second synergy effect. The d-band states of these metallic monolayers, supported on the ZnO(0001) surface, are tuned to shift upward, that is, more close to Fermi level. Therefore, these metallic monolayers indeed exhibit promoted catalysis, in comparison with reported metallic surfaces in the literature.



SECTION: Surfaces, Interfaces, Porous Materials, and Catalysis

CO₂ reduction is a crucial issue for sustainable development in both environmental and energy fields. However, no material is known to be able to catalyze CO₂ reduction to fuel efficiently. Cu/ZnO/Al₂O₃ is an important industrial catalyst used to synthesize methanol with a gaseous H₂, CO, and CO₂ mixture. This catalytic system is also of interest for the potential capability of CO₂ capture and reduction. However, the catalysis mechanism of this catalyst is not understood yet. Hence, it is not feasible to utilize directly a Cu/ZnO-based catalyst for CO₂ reduction now.

The controversy arises regarding the nature of the methanol synthesis and the active sites on Cu/ZnO/Al₂O₃ catalysts. It was suggested first that ionic Cu⁺ sites are the active catalytic center.^{1,2} However, on the other hand, it has also been reported that the catalyst activity is a linear scaling with the metallic Cu surface area.³ Further evidence supporting metallic Cu as the active sites was provided by experiments on single-crystalline Cu(100) and Cu(110) surfaces and polycrystalline Cu films.⁴ These experiments indicate that the methanol synthesis reactions are quite sensitive to surfaces. Recently, Behrens et al.⁵ reported a combinatorial study with experimental evidence and density functional calculations. It has been found there is quite different activity between pure Cu surfaces and the industrial Cu/ZnO/Al₂O₃ catalyst. They claimed that most Cu surfaces are not active at all; however, only a small fraction of the catalyst's surface, consisting of Zn-decorated Cu(211) steps, mainly contributes to the activity of the industrial catalyst. In addition, it has been speculated for a long time the ZnO support can influence the activity of the catalyst. However,

synergistic effects between metallic Cu and the ZnO support have never been identified thoroughly. Frost⁶ suggested that the Schottky junction effects between the metallic Cu particles and ZnO surfaces may increase the number of oxygen vacancies (V_O). However, these defects sites are also active sites when ZnO alone is used as a catalyst; there are no key reaction intermediates observed on ZnO surfaces with the presence of metallic Cu particles. Thus, the Schottky junction effects cannot explain the synergy effects sufficiently.

Moreover, Chinchin et al.⁷ performed isotope labeling experiments and strongly claimed that the CO₂ is the main carbon source for methanol synthesis. However, the CO₂ adsorption and dissociation on the Cu(100) surface are not as good as expected, in comparison with other transition-metal surfaces, namely, Fe, Co and Ni(100), and homogeneous catalysts.⁸ There, they claimed that the Cu(100) surface is not likely to capture the CO₂ molecule at all. Thus, there must be significant synergy effects on the heterogeneous interface between metallic Cu particles and the ZnO support.

Furthermore, the main challenge for understanding a microscopic mechanism of heterogeneous reactions is the identification of the geometry and composition of the catalyst's surface and in situ observations of the various chemical reactions under the equivalent industrial conditions.⁹ Unfortunately, most experimental techniques in surface science are

Received: August 5, 2012

Accepted: August 31, 2012

Published: September 1, 2012

difficult to perform directly at a pressure with a magnitude larger than 50 bar and a temperature higher than 500 K. However, these above experimental conditions are typically applied in industrial catalysis of the methanol synthesis.¹⁰ Thus, what is considered to be important reaction mechanisms on the catalysts' surfaces have usually been concluded, according to chemical intuitions and extensive knowledge from experiments performed at low pressure and low temperature. However, several studies revealed the unreliability of this approach.¹¹ In order to improve the reliability by means of bridging the gap between these experimental temperatures and pressures and industrial ones, it is necessary to consider sufficiently these factors in first-principle calculations.

Recently, Behrens et al.⁵ found that most metallic Cu surfaces are not active at all. Thus, an appropriate surface model is a critical issue for first-principle calculations to study reaction mechanisms. Fortunately, the structural evolution during activation of Cu/ZnO-based catalysts has been characterized thoroughly with several in situ experimental techniques.¹² First, Cu atoms were present in the form of substitutional Cu²⁺ in Cu/ZnO solid solution as determined with in situ resonant X-ray diffraction and electron energy loss spectroscopy. Then, the Cu atoms were extracted from the Cu/ZnO solid solution under the reductive atmosphere, forming metallic Cu crystallites. The Cu crystallites could be reoxidized by heating in air and redispersed in the Cu/ZnO solid solution, in the form of substitutional Cu²⁺ on the Zn lattice sites again. Although there was no further evidence to clarify which ZnO surfaces were involved in the above reactions, the oxygen-terminated surface should be considered first, namely, the ZnO(000 $\bar{1}$) surface. This is due to the fact that this surface is the most reducible ZnO surface. As is well-known, the oxygen vacancy formation can efficiently stabilize ZnO polar surfaces by means of suppressing the macroscopic dipole moment.

In this work, we first performed first-principle thermodynamics calculations to determine the phase diagram of Cu/ZnO(000 $\bar{1}$) surfaces under industrial temperature and pressure. We found that the Cu/ZnO(000 $\bar{1}$) surfaces with metallic monolayers containing Cu and Zn atoms can be formed and stable. Then, CO₂ adsorption was studied thoroughly on these metallic monolayers of all reduced Cu/ZnO(000 $\bar{1}$) surfaces. Because there is an intermediate binding strength between CO₂ and these metallic monolayers, we expected that the CO₂ dissociation and reduction on these metallic monolayers should be improved significantly, compared with that of pure metallic Cu surfaces. Furthermore, we investigated the CO₂ reduction on these metallic monolayers. Calculated results indicate that these metallic monolayers are indeed more active and almost optimal for CO₂ reduction, in comparison with reported surfaces in the literature, for example, Cu(100) and CuZn(211). This behavior is also quite reasonably interpreted with the d-band model. Thus, we have found two important synergy effects between the metallic monolayers and their support, namely, the ZnO(000 $\bar{1}$) surface. Finally, we would propose the feasibility of CO₂ reduction on the Cu/ZnO(000 $\bar{1}$) surfaces under industrial conditions.

The Cu/ZnO solid solutions were simulated with a Cu substitutional ZnO wurtzite structure. All surface structures were described by periodically repeated slabs using an extended (2 × 2) unit cell along the [000 $\bar{1}$] direction (Figure 1a). The thickness of these slabs was specified to be four Zn–O double layers with hydrogen saturated on the Zn termination. The

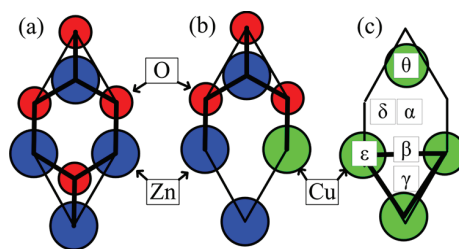


Figure 1. Top view of the studied Cu/ZnO(000 $\bar{1}$) surface: (a) the perfect ZnO(000 $\bar{1}$) surface, (b) Zn₃Cu₁ with an *s*V_O defect, and (c) the Cu₄ surface with a *q*V_O defects and all studied active sites of CO₂ adsorption (noted with α , β , γ , θ , δ , and ϵ). Bold lines indicate bonds between Cu (green), Zn (blue), and O (red) atoms.

upper four atomic layers were allowed to relax, while the atoms in the remaining layers were fixed at their bulk structures.¹³

We have considered five uniform Cu concentration gradients on the Cu/ZnO(000 $\bar{1}$) surface, in the range of 0–100 atom %, denoted by the stoichiometry of the first cationic layer, namely, Zn₄, Zn₃Cu₁, Zn₂Cu₂, Zn₁Cu₃, and Cu₄, respectively. For all of these surfaces, we further considered uniform concentration gradients of oxygen vacancy (V_O) defects at 25, 50, 75, and 100%, corresponding to the nomenclature of *s*V_O, *d*V_O, *t*V_O, and *q*V_O (Figure 1), respectively. Calculated partial pressures of gaseous CO (10 bar), CO₂ (10 bar), H₂ (40 bar), and H₂O (1 bar) and the temperature (600 K) were referred to the industrial conditions.⁵ Then, the formation energies of these V_O defects were calculated to determine the surface phase diagrams of the Cu/ZnO(000 $\bar{1}$) surfaces. The four stable *q*V_O surfaces were selected for further studies of CO₂ adsorption and reduction. Studied active sites for CO₂ adsorption are represented in Figure 1c.

The surface phase diagram is a critical factor to understand the geometry and composition on the Cu/ZnO(000 $\bar{1}$) surface. As the Cu/ZnO(000 $\bar{1}$) surface exchanges oxygen with its surroundings, we need to determine the chemical potential of surface oxygen first. The chemical potential of surface oxygen, μ_{O} , varies due to the change of temperature and oxygen partial pressure, as well as the partial pressure of other reductive gases (H₂ and CO). Particularly, oxygen vacancy formation is quite sensitive to the μ_{O} under varying conditions. For first-principle calculations, the high-temperature and high-pressure effects can be achieved by taking into account explicitly the chemical potential change in terms of thermodynamics.¹⁴ At a given temperature, *T*, and partial pressures, *p*, formation energies of oxygen vacancies, $\gamma(T, p)$, can be defined as

$$\gamma(T, p) = \frac{1}{A} [G(T, p)_{\text{d}} + \sum n_{\text{O}} \mu_{\text{O}}(T, p) - G(T, p)_{\text{p}}] \quad (1)$$

where $G(T, p)_{\text{p}}$ and $G(T, p)_{\text{d}}$ are the Gibbs free energies of perfect and defected Cu/ZnO(000 $\bar{1}$) surfaces with respect to surface area, *A*, *n*_O is the number of oxygen vacancies, and $\mu_{\text{O}}(T, p)$ is the chemical potential of oxygen at a specific temperature, *T*, and pressure, *p*. The negative formation energies correspond to stable surface structures with certain numbers of oxygen vacancies. The Gibbs free energies of solid surfaces were replaced by the corresponding total energies, which were calculated with density functional theory (DFT) methods. In addition, we employed the ideal gas approximation to estimate chemical potentials of all gases. The chemical potential of surface oxygen can be expressed by

$$\mu_{\text{O}}(T, p) = \mu_{\text{O}}(T, p_0) + k_{\text{B}}T \ln\left(\frac{p}{p_0}\right) \quad (2)$$

where p_0 and k_{B} are the pressure in standard conditions and the Boltzmann constant. Three reactions in thermodynamic equilibrium between Cu/ZnO(000 $\bar{1}$) surfaces and CO (CO₂), H₂ (H₂O), and O₂ reservoirs were considered. The $\mu_{\text{O}}(T, p_0)$ values were calculated in terms of thermal contributions and zero-point energy corrections. Moreover, the CO₂ adsorption and hydrogenation reactions were described with the following expression

$$\Delta G(T, p) = G(T, p)_{\text{a}} - G(T, p)_{\text{c}} - \sum n_i \mu_i(T, p) \quad (3)$$

Here, $G(T, p)_{\text{c}}$ are the Gibbs free energies of the clean Cu/ZnO(000 $\bar{1}$) surfaces with various studied metallic monolayers, namely, the Zn₃Cu₁, Zn₂Cu₂, Zn₁Cu₃, and Cu₄ surfaces with qV_{O} defects. $G(T, p)_{\text{a}}$ are the Gibbs free energies of these surfaces with adsorbed CO₂ and H₂ molecules, and n_i is the number of adsorbates. On the one hand, the Gibbs free energies of solid surfaces are still replaced by the corresponding total energies obtained from DFT calculations. On the other hand, the chemical potential, μ_i , of gases was calculated at a certain temperature, T , and pressure, p .

For pure ZnO (Zn₄), the qV_{O} defect is not stable under the condition with a high chemical potential of surface oxygen, namely, the oxygen-rich condition. Even under industrial conditions, only the case with the lowest concentration of V_{O} defects (sV_{O}) can be stable. However, the V_{O} defects can be easily stabilized as long as the Cu concentration on the ZnO(000 $\bar{1}$) surface is increased (see Figure 2). The detailed

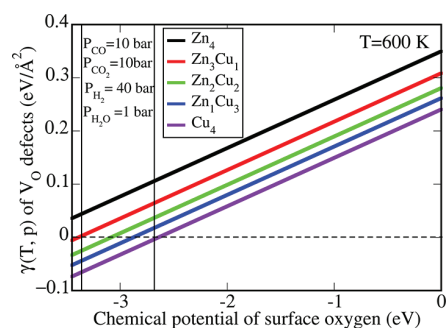


Figure 2. Surface phase diagrams of all metallic monolayers supported by the ZnO(000 $\bar{1}$) surface, namely, the Zn₄, Zn₃Cu₁, Zn₂Cu₂, Zn₁Cu₃, and Cu₄ surfaces with qV_{O} defects, under industrial temperature and partial pressures. The dashed line refers to perfect surfaces.

$\gamma(T, p)$ data can be found in Table S2 in the Supporting Information. In Figure 3, we show the atomic structures of the metallic monolayer on all qV_{O} surfaces. It indicates that only the metallic Zn₄ monolayer is not stable under industrial conditions. The V_{O} defects have been identified to be active sites for methanol synthesis on the pure ZnO(000 $\bar{1}$) surface.¹⁵ Thus, the Cu can promote significantly the activity on the ZnO(000 $\bar{1}$) surface by creating more V_{O} defects. Theoretical calculations indicate that the Cu substituted on the sites of Zn in the ZnO wurtzite structure is divalent with the electronic configuration of Cu (d⁹).¹⁶ The valence state of substituted Cu had been also validated in the subsequent experiment.¹² As the Cu (d⁹) is not the most stable electronic structure, the Cu dopants prefer to be present as Cu⁺ with less coordinated

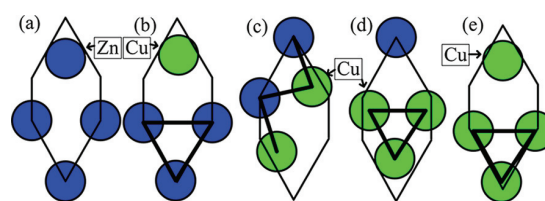


Figure 3. Top view of these metallic monolayers supported by ZnO(000 $\bar{1}$) surfaces, namely, (a) Zn₄, (b) Zn₃Cu₁, (c) Zn₂Cu₂, (d) Zn₁Cu₃, and (e) Cu₄ surfaces with qV_{O} defects. Bold lines indicate bonds between Cu (green) and Zn (blue) atoms.

oxygen on the surface. In contrast, Zn²⁺ is quite stable with the electronic structure of Zn (d¹⁰). Hence, it costs more energy to create active V_{O} defects by breaking Zn²⁺–O bonds on a Cu/ZnO(000 $\bar{1}$) surface, in comparison with breaking Cu²⁺–O bonds. Therefore, we have found the first synergy effect, that is, the Cu dopants can promote the activity of the ZnO(000 $\bar{1}$) surface in way of stabilizing V_{O} defects. Accompanied by the qV_{O} formation, metallic monolayers containing certain Zn and Cu atoms are formed and exposed to gas phases. As there is charge transfer from these metallic monolayers to the sublayer (O), the metallic Cu₄ monolayer, as well as the Zn₃Cu₁, Zn₂Cu₂, and Zn₁Cu₃ surfaces, differs significantly from pure metallic Cu surfaces. We will analyze their activity and relevant electronic structure in detail in the next paragraphs.

The binding strength between CO₂ and Cu surfaces determines the ability of the Cu surfaces acting as a catalyst. During catalysis, the Cu surfaces form chemical bonds with CO₂ and break one of the C–O bonds for its subsequent hydrogenation. The maximum in the catalytic rate requires an intermediate Cu–O bond strength, which is the optimal compromise between having a lower activation barrier for CO₂ dissociation (prefers a stronger Cu–O bond), and also the ability to activate further reactions with the adsorbed hydrogen (prefers a weaker Cu–C bond). The catalytic rate is a function of adsorption energy, which is reflected in terms of the volcano curve.¹⁷ In the remainder, we will show that these metallic monolayers (Zn₃Cu₁, Zn₂Cu₂, Zn₁Cu₃, and Cu₄) supported with a ZnO(000 $\bar{1}$) surface are indeed optimized surfaces, close to the peak of volcano curve, in comparison with reported metallic Cu surfaces.^{5,8}

Liu et al.⁸ have done comparative studies for CO₂ conversion on transition-metal (Fe, Co, Ni, and Cu) surfaces. They claimed that the CO₂ adsorption on the Cu(100) surface is too weak (+0.75 eV) and that the corresponding activation energy is very high. In addition, there is a stronger adsorption ability between CO₂ and the Ni(100) surface (–0.05 eV), as well as Co(100) surfaces (–0.42 eV). The activation energies for CO₂ dissociation are lower too. In contrast, the CO₂ is likely to overbind with the Fe (100) surface (–1.45 eV), and it results in an undesired thermodynamic sink. The activation energy for CO₂ dissociation rises for the Fe(100) surface. According to the classical volcano curve, as a consequence, the optimal adsorption energy for CO₂ conversion should be between –0.42 and –1.45 eV. All metallic monolayers on these surfaces (Zn₃Cu₁, Zn₂Cu₂, Zn₁Cu₃, and Cu₄) and six possible active sites (see Figure 1c) have been considered to investigate CO₂ adsorption thoroughly. The CO₂ adsorption on the metallic Cu₄ monolayer is considerably optimized (–1.31 eV) in comparison with above pure metallic surfaces. There are also consistent findings for metallic Zn₁Cu₃ (–0.82 eV), Zn₂Cu₂ (–1.09 eV), and Zn₁Cu₃ (–1.33 eV) monolayers. The detailed

$\Delta G(T,p)$ data for all studied active sites are available in Table S3 in the Supporting Information.

The reactions of CO_2 dissociation and hydrogenation on these metallic monolayers of $\text{Cu}/\text{ZnO}(000\bar{1})$ surfaces can be expected by analyzing relevant electronic structures. According to the d-band model, for the $\text{Cu}(100)$ surface, when the CO_2 approaches the surface, the C-2p and O-2p orbitals interact first with Cu-4s orbitals and then switch upon coupling to the Cu-3d orbitals. As all transition metals have a half-filled 4s state in the metallic state, they do not differ significantly from one metal to another. The leading difference in this interaction is attributed to the d-band states because it is more localized. The interaction between the O-2p (and C-2p) and Cu-3d states gives rise to separated bonding and antibonding states (see Figure 4). The strength of Cu–O and Cu–C bonds is directly

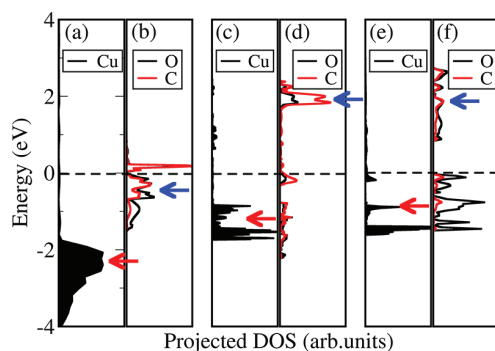


Figure 4. Projected DOS of the Cu d-band on (a) a metallic $\text{Cu}(100)$ surface, (c) a metallic Zn_1Cu_3 monolayer, and (e) a metallic Cu_4 monolayer; the C-2p and O-2p states of adsorbed CO_2 are shown on (b) the $\text{Cu}(100)$ surface, (d) a metallic Zn_1Cu_3 monolayer, and (f) a metallic Cu_4 monolayer. The red and blue arrows indicate the d-band center and antibonding states, respectively.

affected by the relative occupancy of bonding and antibonding states. In other words, the position of the d-band center with respect to the Fermi level determines whether the interaction is likely to be attractive or repulsive. In Figure 4, it indicates that the antibonding states of Cu–O and Cu–C interactions are considerably occupied for the $\text{Cu}(100)$ surface. For the metallic Cu_4 and Zn_1Cu_3 monolayers, however, as the d-band centers are tuned to shift upward, it results in fewer occupied antibonding states (see Figure 4). As a result, the CO_2 adsorption on these metallic monolayers exhibits more attractive features. Therefore, these metallic monolayers with a $\text{ZnO}(000\bar{1})$ support have indeed optimized the adsorption energy close to the peak of the volcano curve, compared with that of the pure $\text{Cu}(100)$ surface.

Besides, Behrens et al.⁵ claimed that the Zn-decorated $\text{Cu}(211)$ surface is more active rather than the pure $\text{Cu}(211)$ surface (hereafter, we will use $\text{CuZn}(211)$ to refer to the Zn-decorated $\text{Cu}(211)$ surface, unless otherwise stated). We also performed further investigations of CO_2 dissociation and hydrogenation to methanol on the metallic Cu_4 monolayer in order to compare the whole process with that on the $\text{CuZn}(211)$ surface.⁵ We have obtained considerably consistent conclusions, as expected by the d-band model. The calculated results for the hydrogenation processes are shown in Figure 5. For the Cu_4 case, all reaction steps are exothermic with respect to the clean Cu_4 surface and gaseous CO_2 and H_2 phases. The second step of CO_2 hydrogenation, namely, from $\text{HCOO}^* +$

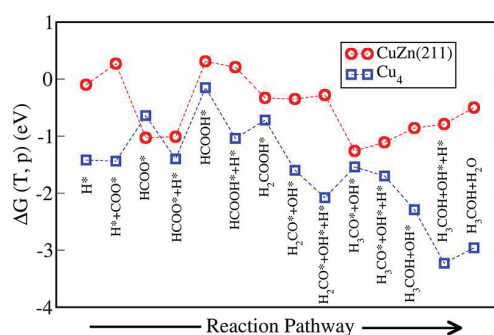


Figure 5. CO_2 reduction on a metallic Cu_4 monolayer under industrial pressure and temperature conditions is compared with reported results on a $\text{CuZn}(211)$ surface.⁵ The $\Delta G(T,p)$ scale is referred to the clean surface and gaseous CO_2 and H_2 . The asterisk is to clarify the adsorbed species.

H^* to HCOOH^* species, is the most endothermic reaction for both $\text{CuZn}(211)$ and the metallic Cu_4 monolayer. Obviously, the reaction on the metallic Cu_4 monolayer is more energetically favorable. Furthermore, the critical step of CO_2 dissociation is improved effectively on the metallic Cu_4 monolayer too (from H_2COOH^* to $\text{H}_2\text{CO}^* + \text{OH}^*$). Besides, there are also more exothermic reactions for the hydrogenation process, that is, from the $\text{H}_2\text{CO}^* + \text{OH}^*$ species to $\text{CH}_3\text{OH} + \text{H}_2\text{O}$. Instead, there are more endothermic reactions on the $\text{CuZn}(211)$ surface. This is exactly in agreement with the d-band model analysis.

On the one hand, the industrial catalyst is mostly prepared with a coprecipitation technique;¹² the pure Cu-covered monolayer (Cu_4) is not usually the dominant surface. On the other hand, the metallic Zn_3Cu_1 monolayer is relatively less stable in comparison with other surfaces. Therefore, the active sites of the industrial catalyst can be also contributed from the metallic Zn_2Cu_2 and Zn_1Cu_3 surfaces. We performed further investigations for the metallic Zn_2Cu_2 and Zn_1Cu_3 surfaces. It has been found that there are analogous activities for CO_2 reduction on the two surfaces too. The reaction energies of CO_2 hydrogenation are given in Table S4 of the Supporting Information. In the work of Behrens et al.,⁵ they did not observe these surfaces in high-resolution transition electron microscopy (HRTEM). However, the HRTEM measurements were performed under conventional vacuum conditions, instead of conditions with a gaseous H_2 and CO_2 atmosphere. Therefore, these surfaces that we proposed are definitely reconstructed under vacuum conditions. This can explain why these surfaces that we proposed were not imaged. According to the above analyses, the CO_2 reduction is indeed feasible with the modified Cu/ZnO -based catalyst. The critical issue is to activate the modified Cu/ZnO -based catalyst before its industrial application.

In conclusion, we have employed first-principle thermodynamics to study phase diagrams and CO_2 reduction on the $\text{Cu}/\text{ZnO}(000\bar{1})$ surfaces. The calculated results suggest two synergy effects on the $\text{Cu}/\text{ZnO}(000\bar{1})$ surface. As the Cu could promote the formation of oxygen vacancies on the ZnO surface, the activity of the $\text{ZnO}(000\bar{1})$ surface can be improved significantly. Meanwhile, these metallic monolayers on the $\text{ZnO}(000\bar{1})$ surfaces have more localized d-band states, and also the Cu d-band states are tuned to shift considerably upward. This is the second synergy effect on the $\text{Cu}/\text{ZnO}(000\bar{1})$ surfaces. The CO_2 adsorption energies on these

metallic monolayers of Cu/ZnO(000 $\bar{1}$) surfaces are optimized values, expected by the d-band model, close to the peak of volcano curve. The comparative studies of CO₂ adsorption and reduction have also demonstrated the optimized activity. It is in excellent agreement with the expectations of the d-band model.

■ ASSOCIATED CONTENT

📄 Supporting Information

The computational details, formation energies of various studied defects on all surface models, and reaction energies of hydrogenation. This material is available free of charge via the Internet at <http://pubs.acs.org>.

■ AUTHOR INFORMATION

Corresponding Author

*E-mail: xiao@bccms.uni-bremen.de.

Author Contributions

The manuscript was written through contributions of all authors. All authors have given approval to the final version of the manuscript. All authors have contributions equally to this work.

Notes

The authors declare no competing financial interest.

■ ACKNOWLEDGMENTS

J.X. acknowledges financial support by the Chinese Scholarship Council (CSC) and computational resources of hardware and software by BCCMS (Bremen Center for Computational Materials Science), Universität Bremen.

■ REFERENCES

- (1) Klier, K. Methanol Synthesis. *Adv. Catal.* **1982**, *31*, 243–313.
- (2) Szanyi, J.; Goodman, D. W. Methanol Synthesis on Cu(100) Catalyst. *Catal. Lett.* **1991**, *10*, 383–390.
- (3) Chinchen, G. C.; Waugh, K. C.; Whan, D. A. The Activity and State of the Copper Surface in Methanol Synthesis Catalysts. *Appl. Catal.* **1986**, *25*, 101–107.
- (4) Yoshihara, J.; Parker, S. C.; Schafer, A.; Campbell, C. T. Methanol Synthesis and Reverse Water–Gas Shift Kinetics over Clean Polycrystalline Copper. *Catal. Lett.* **1995**, *31*, 313–324.
- (5) Behrens, M.; Studt, F.; Kasatkin, I.; Kühl, S.; Hävecker, M.; Pedersen, F. A.; Zander, S.; Girsig, F.; Kurr, P.; Kniep, B. L.; Tovar, M.; Fischer, R. W.; Nørskov, J. K.; Schlögl, R. The Active Site of Methanol Synthesis over Cu/ZnO/Al₂O₃ Industrial Catalysts. *Science* **2012**, *336*, 893–897.
- (6) Frost, J. C. Junction Effect Interactions in Methanol Synthesis Catalysts. *Nature* **1998**, *334*, 577–580.
- (7) Chinchen, G. C.; Denny, P. J.; Parker, D. G.; Spencer, M. S.; Whan, D. A. Mechanism of Methanol Synthesis from CO₂/CO/H₂ Mixtures over Copper/Zinc Oxide/Alumina Catalysts: Use of ¹⁴C-Labelled Reactants. *Appl. Catal.* **1987**, *30*, 333–338.
- (8) Liu, C.; Cundari, T. R.; Wilson, A. K. CO₂ Reduction on Transition Metal (Fe, Co, Ni, and Cu) Surfaces: In Comparison with Homogeneous Catalysis. *J. Phys. Chem. C* **2012**, *116*, 5681–5688.
- (9) Reuter, K.; Scheffler, M. First-Principles Atomistic Thermodynamics for Oxidation Catalysis: Surface Phase Diagrams and Catalytically Interesting Regions. *Phys. Rev. Lett.* **2003**, *90*, 046103/1–046103/4.
- (10) Lee, S. Methanol Synthesis Technology; CRC Press: Boca Raton, FL, 1989.
- (11) Stampfl, C.; Ganduglia-Pirovano, M. V.; Reuter, K.; Scheffler, M. Catalysis and Corrosion: The Theoretical Surface-Science Context. *Surf. Sci.* **2002**, *500*, 368–394.
- (12) Andreasen, J. W.; Rasmussen, F. B.; Helveg, S.; Molenbroek, A.; Ståhl, K.; Nielsen, M. M.; Feidenhansl, R. Activation of a Cu/ZnO Catalyst for Methanol Synthesis. *J. Appl. Crystallogr.* **2006**, *39*, 209–221.
- (13) Kiss, J.; Frenzel, J.; Nair, N. N.; Meyer, B.; Marx, D. Methanol Synthesis on ZnO(0001). III. Free Energy Landscapes, Reaction Pathways, And Mechanistic Insights. *J. Chem. Phys.* **2011**, *134*, 064710/1–064710/4.
- (14) Reuter, K.; Scheffler, M. Composition, Structure, And Stability of RuO₂(110) as a Function of Oxygen Pressure. *Phys. Rev. B* **2002**, *65*, 035406/1–035406/11.
- (15) Kurtz, M.; Strunk, J.; Hinrichsen, O.; Muhler, M.; Fink, K.; Meyer, B.; Wöll, Ch. Active Sites on Oxide Surfaces: ZnO-Catalyzed Synthesis of Methanol from CO and H₂. *Angew. Chem., Int. Ed.* **2005**, *44*, 2790–2794.
- (16) Lupan, O.; Pauporté, T.; Bahers, T. L.; Viana, B.; Ciofini, I. Wavelength-Emission Tuning of ZnO Nanowire-Based Light-Emitting Diodes by Cu Doping: Experimental and Computational Insights. *Adv. Funct. Mater.* **2011**, *21*, 3564–3572.
- (17) Nilsson, A.; Pettersson, L. G. M.; Hammer, B.; Bligaard, T.; Christensen, C. H.; Nørskov, J. K. The Electronic Structure Effect in Heterogeneous Catalysis. *Catal. Lett.* **2005**, *100*, 111–114.

Contents

Computational details,

Table S1. Validation of our L_4 (four bilayers) model, in comparison with L_6 and L_8 models.

Table S2. Calculated formation energies, $\gamma(T, p)$, of oxygen vacancies, namely, sV_O , dV_O , tV_O and qV_O defects on all studied Zn_4 , Zn_3Cu_1 , Zn_2Cu_2 , Zn_1Cu_3 and Cu_4 surfaces, respectively ($meV/\text{\AA}^2$). The temperature and pressure were referred to industrial conditions.

Figure S1. Geometries of metallic monolayers on (a) Zn_3Cu_1 , (b) Zn_2Cu_2 , (c) Zn_1Cu_3 and (d) Cu_4 surfaces with qV_O defects, respectively. Cu: green, Zn: red and O: blue.

Table S3. Calculated adsorption energies, $\Delta G(T, p)$, of CO_2 molecules on various adsorbed sites of the metallic monolayers of Zn_3Cu_1 , Zn_2Cu_2 , Zn_1Cu_3 and Cu_4 surfaces, respectively (eV/CO_2). The temperature and pressure were referred to industrial conditions.

Figure S2. Projected DOS of Cu d-band on (a) metallic Cu (100) surface, (c) metallic Zn_3Cu_1 monolayer, (e) metallic Zn_2Cu_2 monolayer; and C-2p and O-2p states of adsorbed CO_2 shown on (b) Cu (100) surface, (d) metallic Zn_3Cu_1 monolayer, (f) metallic Zn_2Cu_2 monolayer. The red and blue arrows indicate d-band centre and antibonding states, respectively.

Table S4. Reaction energies of CO_2 hydrogenation with respect to the clean Zn_2Cu_2 and Zn_1Cu_3 surfaces and gaseous CO_2 and H_2 phases, are given with corrections of thermal contributions of gaseous molecules and zero point energy correction. (eV/CO_2)

Computational Details

For Cu/ZnO (0001) surfaces, the irreducible Brillouin zones were sampled with (4×4×1) space grids. All-electron Kohn-Sham equations were solved by employing the linear combination of atomic orbitals (LCAO) method, implemented in CRYSTAL09 code,¹ with local Gaussian-type basis functions for all elements Zn,² Cu,³ O,⁴ C⁵ and H,⁶ respectively. We used the Perdew-Burke-Ernzerhof (PBE) functional⁷ at the level of the Generalized Gradient Approximation (GGA) for electronic exchange-correlation interactions. In addition, we used periodic slab model with (3×3) supercell containing five atomic layers, to investigate CO₂ adsorbent on Cu (100) surface and its electronic structures. The irreducible Brillouin zone was sampled with (4×4×1) space grids. The same functional was used, as well as basis sets for Cu, C and O elements. Moreover, in order to compare the *d*-band states of these metallic monolayers with that of Cu (100) surface, we have employed periodic slab model with (3×3) supercell containing five atomic layers.

As the ZnO (0001) surface is a typical polar surface, it is quite difficult to design a perfect slab model with converged sufficiently surface energy. In this work, thus, we fixed partial layers in their bulk structure, and only optimized the first two Zn-O bilayers. We have firstly validated the reliability of our model (L₄), in comparison with models of six Zn-O bilayers (L₆) and eight Zn-O bilayers (L₈), respectively. The energetic difference is approximately 0.04 eV.

Table S1. Validation of our L₄ (four bilayers) model, in comparison with L₆ and L₈ models.

Models	$E_{relaxed} - E_{non-relaxed}$
L ₄	-0.68 eV
L ₆	-0.71 eV
L ₈	-0.72 eV

Table S2. Calculated formation energies, $\gamma(T, p)$, of oxygen vacancies, namely, sV_O, dV_O, tV_O and qV_O defects on various studied Zn₄, Zn₃Cu₁, Zn₂Cu₂, Zn₁Cu₃ and Cu₄ surfaces, respectively (meV/Å²). The temperature and pressure were referred to industrial conditions.

Surfaces	sV _O	dV _O	tV _O	qV _O
Zn ₄	-3	<i>12</i>	<i>24</i>	<i>36</i>
Zn ₃ Cu ₁	-40	-27	-13	-5
Zn ₂ Cu ₂	-36	-61	-32	-33
Zn ₁ Cu ₃	-35	-63	-47	-52
Cu ₄	-46	-76	-72	-73

Note: the stable V_O defects are marked in blue and unstable V_O defects in red and italic.

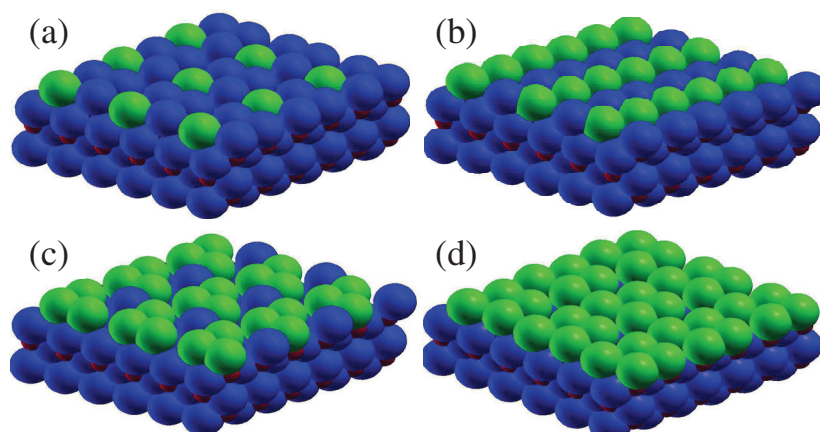


Figure S1. Geometries of metallic monolayers on (a) Zn_3Cu_1 , (b) Zn_2Cu_2 , (c) Zn_1Cu_3 and (d) Cu_4 surfaces with qVo defects, respectively. Cu: green, Zn: blue and O: red.

Table S3. Calculated adsorption energies, $\Delta G(T, p)$, of CO_2 molecules on various adsorbed sites of the metallic monolayers of Zn_3Cu_1 , Zn_2Cu_2 , Zn_1Cu_3 and Cu_4 surfaces, respectively (eV/ CO_2). The temperature and pressure were referred to industrial conditions.

	α	β	γ	ϵ	δ	θ
Zn_3Cu_1	<i>-0.14</i>	<i>-0.32</i>	<i>0.71</i>	-0.73	-0.82	<i>0.69</i>
Zn_2Cu_2	-1.09	-0.88	-0.87	<i>-0.18</i>	-1.04	-0.46
Zn_1Cu_3	-0.56	-0.79	-0.78	<i>-0.33</i>	-1.33	<i>-0.34</i>
Cu_4	-0.81	-1.33	<i>0.19</i>	<i>-0.34</i>	-1.25	<i>0.15</i>

Note: the optimized adsorption energies between -0.42 and -1.45 eV are marked in blue and other values in red and italic.

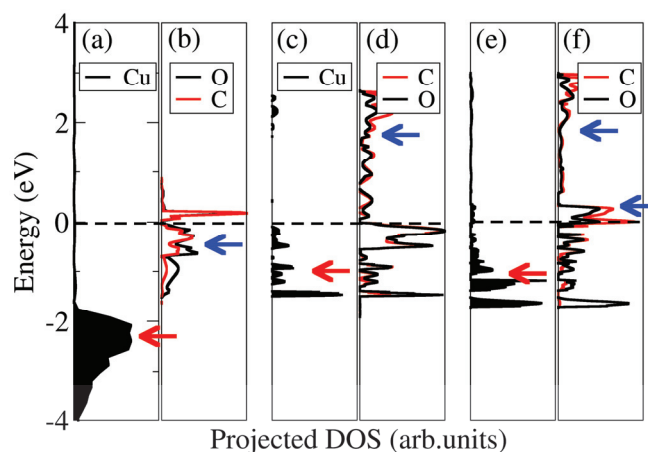


Figure S2. Projected DOS of Cu d-band on (a) metallic Cu (100) surface, (c) metallic Zn_3Cu_1 monolayer, (e) metallic Zn_2Cu_2 monolayer; and the C-2p and O-2p states of adsorbed CO_2 shown on (b) Cu (100) surface, (d) metallic Zn_3Cu_1 monolayer, (f) metallic Zn_2Cu_2 monolayer. The red and blue arrows indicate the d-band centre and antibonding states, respectively.

Table S4. Reaction energies of CO₂ hydrogenation with respect to the clean Zn₂Cu₂ and Zn₁Cu₃ surfaces and gaseous CO₂ and H₂ phases, are given with corrections of thermal contributions of gaseous molecules and zero point energy correction, (eV/CO₂).

	+1H	+2H	+3H	+4H	+5H	+6H	Finals
	*COOH	*COH+*OH	*COH ₂ +*OH	*COH ₃ +*OH	*CH ₃ OH+*OH	*CH ₃ OH+*H ₂ O	CH ₃ OH+H ₂ O
Zn ₂ Cu ₂	-0.39	-0.75	-0.13	-1.75	-2.13	-2.41	-1.43
Zn ₁ Cu ₃	0.02	-0.96	-0.68	-2.00	-1.97	-2.14	-1.67

[1] Dovesi, R.; Saunders, V. R.; Roetti, C.; Orlando, R.; Zicovich-Wilson, C. M.; Pascale, F.; Civalleri, B.; Doll, K.; Harrison, N. M.; Bush, I. J.; D'Arco, Ph.; Llunell, M. CRYSTAL09, **2009**, User's Manual, University of Torino, Torino.

[2] Jaffe, J. E.; Hess, A. C. Hartree-Fock Study of Phase Changes in ZnO at High Pressure. *Phys. Rev. B* **1993**, 48, 7903-7909.

[3] Gatti, C.; Saunders, V. R.; Roetti, C.; Crystal field effects on the topological properties of the electron density in molecular crystals: The case of urea. *J. Chem. Phys.* **1994**, 101, 10686-10696.

[4] Corno, M.; Busco, C.; Civalleri, B.; Ugliengo, P. Periodic ab initio study of structural and vibrational features of hexagonal hydroxyapatite Ca₁₀(PO₄)₆(OH)₂. *Phys. Chem. Chem. Phys.* **2006**, 8, 2464-2472.

[5] Gatti, C.; Saunders, V. R.; Roetti, C. Crystal-field effects on the topological properties of the electron-density in molecular-crystals - the case of urea. *J. Chem. Phys.* **1994**, 101, 10686-10696.

[6] Dovesi, R.; Ermondi, E.; Ferrero, E.; Pisani, C.; Roetti, C. Hartree-Fock study of lithium hydride with the use of a polarizable basis set. *Phys. Rev. B* **1983**, 29, 3591-3600.

[7] Perdew, J. P.; Burke, K.; Ernzerhof, M. Generalized Gradient Approximation Made Simple. *Phys. Rev. Lett.* **1996**, 77, 3865-3868.

APPENDIX E:

Theoretical insights into CO₂ activation and reduction on the Ag(111) monolayer supported on a ZnO(0001) substrate,

J. Phys. Chem. C **2013** (117) 1804-1808,

J. Xiao and T. Frauenheim,*

Theoretical Insights into CO₂ Activation and Reduction on the Ag(111) Monolayer Supported on a ZnO(0001) Substrate

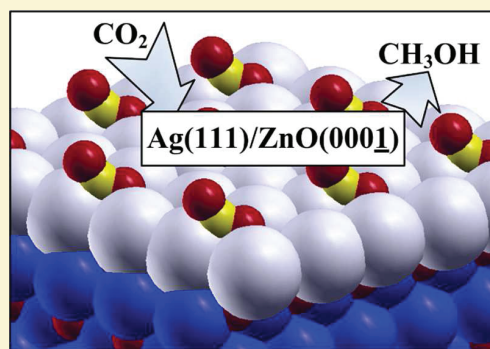
Jianping Xiao^{*,†,‡} and Thomas Frauenheim[†]

[†]Bremen Center for Computational Materials Science, Universität Bremen, Am Fallturm 1, 28359 Bremen, Germany

[‡]School of Engineering and Science, Jacobs University Bremen, Campus Ring 1, 28759 Bremen, Germany

Supporting Information

ABSTRACT: First principles calculations are performed to investigate CO₂ adsorption and reduction on Ag(111)/ZnO(0001) surfaces and interfaces. First, the pristine Ag(111) surface turns out to be quite noble for CO₂ adsorption, as its d-band states are located well below the Fermi level. The d-band states of the Ag(111) surface are subject to a tensile strain slightly shifting toward the Fermi level. However, the d-band center is still far away from the Fermi level. A critical change of the d-band states is obtained when the stretched Ag(111) monolayer is supported on the ZnO(0001) substrate. The binding ability between the supported Ag(111) monolayer and CO₂ molecule is an intermediate strength. Thus, the CO₂ reduction in the subsequent hydrogenation process is optimized as well. Furthermore, we demonstrate that the stretched Ag(111) monolayer supported on the ZnO(0001) substrate is indeed stable under H₂-rich conditions. This surface can even maintain the improved ability for CO₂ adsorption and reduction in the presence of Zn impurities.



INTRODUCTION

CO₂ chemistry has become a very attractive field with not only environmental concerns but also the potential utilization of CO₂ as an alternative and economical feedstock for fuel production.¹ CO₂ reduction is an important approach to recycle the anthropogenic CO₂ emission. However, it is still a challenging task to activate CO₂ due to its robust stability.

Over the past several decades, our understanding why particular catalysts are good for specific reactions has been improved. The current challenge is to answer the inverted problem; given that we need to catalyze a certain reaction under a set of specified conditions, which material should we choose? Theoretical descriptors are becoming more and more important for computational design of catalysts. Therefore, the d-band model was developed and served as an important descriptor for understanding and predicting the reactivity of catalysts.² The variation in adsorption energy from one metal to another is determined by the interaction between the adsorbate and the surface. It turns out that, for transition metal surfaces, the interaction is mainly affected by their d-band states. The rule is that the higher in energy the d-band states are relative to the Fermi energy of the metal surface, the stronger is the interaction with the adsorbate states. The relevant mechanism is that when the d-band states are close to the Fermi energy, antibonding states can be pushed above the Fermi energy. This response decreases the Pauli repulsion and increases the bond strength between the adsorbate and the metal surfaces. For these metals with the same d-orbitals occupancy, the coupling matrix element between the adsorbate and the d-orbitals of

metal surfaces determines their reactivity. The larger the adsorbate–metal d coupling matrix element is, the stronger is the Pauli repulsion. Therefore, the noble metals are always located at the right corner in the periodic table. In the group IB, a close-packed Ag(111) surface possesses the deepest-lying d-band states of -4.30 eV relative to its Fermi energy, in comparison with Cu (-2.67 eV) and Au (-3.56 eV).³ However, a small adsorbate–metal d coupling matrix element between the Ag(111) surface and adsorbates, e.g., carbon and nitrogen, cannot push antibonding states above its Fermi energy. Hence, it results in the extremely noble Ag(111) surface. Even the Ag(111) surface is slightly more noble than the Au(111) surface for carbon and nitrogen adsorbates. It sounds unwise if one wants to make extremely stable CO₂ molecule activated on the Ag(111) surface.

For most chemical reactions, we need an intermediate interaction between the adsorbate and metal surfaces. It is reflected in the well-known volcano curve.⁴ The first step of CO₂ reduction is to break a C–O bond where a strong bond between the CO₂ adsorbate and catalyst is needed. In contrast, a weak CO₂ adsorbate–catalyst bond is preferred for the subsequent hydrogenation process. Thus, the intermediate adsorption strength is required in order to achieve optimized CO₂ dissociation and the subsequent hydrogenation. Liu et al.⁵ have found a significant trend, on the basis of a comparative study for 3d series transition metals (Fe, Co, Ni, and Cu(100)

Received: November 24, 2012

Published: December 17, 2012

surfaces), where calculated adsorption energies exhibit in the order of Fe (−1.45 eV) < Co (−0.42 eV) < Ni (−0.05 eV) < Cu (+0.75 eV). The developed Brøsted–Evans–Polanyi (BEP) relationship⁵ was also in agreement with such trend. This trend is quite consistent with the d-band model analysis, too. According to the volcano curve, the CO₂ adsorption energy for an optimal catalyst can be obtained between −0.42 and −1.45 eV. Although the reactivity of metal surfaces is contributed from both structural and electronic properties, the optimal adsorption energy values are varying from one surface to another. This energetic range can be still served as a significant reference for computational design of catalyst for CO₂ conversion.

For heterogeneous catalyst, a lot of attention has been focused not only on pure metals but also on oxides supported catalysts.⁶ As the activity of supported catalysts can be improved sufficiently through the strong metal–support interaction (SMSI),⁷ in comparison with metal surfaces alone, there are numerous successful applications in this field,⁶ e.g., the industrial Cu/ZnO/Al₂O₃ catalyst.⁸ However, the chemical mechanism of the SMSI is not understood thoroughly to date. It can also differ from one supported catalyst to another. In addition, the optimal catalysis is usually obtained by ways of manipulating their electronic structures. As the lattice constant of a metal surface mismatch with its support, it can result in an interface strain. The interface strain, therefore, leads to upshifts or downshifts of its d-band states. Mavrikakis et al.⁹ have demonstrated that a small tensile strain can cause upshifts of the d-band states for a Ru(0001) surface. As a result, the dissociative energy of CO molecule on the stretched Ru(0001) surface can be reduced. Zinc oxide (ZnO) possesses a hexagonal structure, in the crystal plane perpendicular to the ZnO [0001] direction, with a larger lattice constant with respect to the Ag(111) surface. Thus, the tensile strain in the Ag(111)/ZnO(0001) interface can probably tune the d-band states of the Ag(111) surface. However, the critical issue is whether the SMSI effect can improve the reactivity of the Ag(111)/ZnO(0001) surfaces to capture an extremely stable CO₂ molecule; it is an open question so far.

In this article, we have first studied the CO₂ adsorption on the pristine Ag(111) surface as a reference. Meanwhile, the CO₂ activity on the Ag(111) surface subject to a tensile strain of 14% was investigated, too. The d-band states of the stretched Ag(111) surface are shown to be shifted upward slightly. The CO₂ activity on the stretch Ag(111) surface is similar to that on the pristine one. Then, we made further investigations with the stretched Ag(111) surfaces supported on the ZnO(0001) substrate. Here, it still remains an identical tensile strain compared with the previously stretched Ag(111) surface. In order to understand the extension of the SMSI effect, we have already considered trilayers, bilayers, and monolayer of the Ag(111) surfaces supported on the same ZnO(0001) substrate. Hereafter, these abbreviations, that is, *m*-Ag/ZnO, *b*-Ag/ZnO, and *t*-Ag/ZnO surfaces, are adopted to refer to the Ag(111) monolayer, bilayers, and trilayers supported on the ZnO(0001) surface. On the one hand, we found the CO₂ adsorption on the *m*-Ag/ZnO surface is an intermediate binding strength. Calculated results indicate this surface can serve as a catalyst for the subsequent CO₂ reduction. On the other hand, in order to obtain an optimized efficiency of Ag utilization, we next turn to investigate the stability of Ag-doped ZnO(0001) surface, that is, the precursor of the *m*-Ag/ZnO surface, under H₂-rich condition, as well as this surface with a certain amount of Zn

impurities. In addition, we have also studied the CO₂ adsorption and reduction on the *m*-Ag/ZnO surface with certain Zn impurities. Calculated results show the reactivity of the *m*-Ag/ZnO surface to be quite stable in the presence of Zn impurities. This can propose a strategy to optimize the efficiency of Ag utilization.

COMPUTATIONAL SECTION

The pristine and stretched Ag(111) surfaces have been investigated using infinite periodic thin slab models with the relevant [111] orientation and lattice constants of 2.89 and 3.29 Å, respectively. These studied active sites for CO₂ adsorption are represented in Figure 1a. For Ag(111)/ZnO(0001) models,

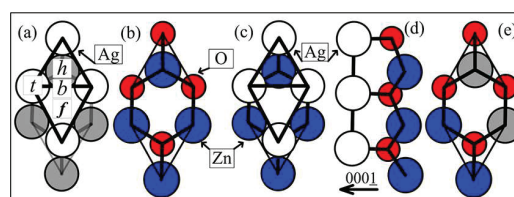


Figure 1. Top views of the (a) pristine Ag(111) surface, (b) perfect ZnO(0001) surface, (c) *m*-Ag/ZnO surface, and (e) perfect Ag₂Zn₂ surface. (d) Side view of the *m*-Ag/ZnO surface. Zn: blue; O: red. The Ag atoms on surface and subsurface are denoted in white and gray spheres, respectively. All studied active sites of CO₂ adsorption are represented in the letters of *t* (top), *h* (hcp), *b* (bridge), and *f* (fcc). Chemical bonds are denoted in bold lines.

the *m*-Ag/ZnO(0001) surface is exemplified to be shown in Figure 1c,d. Last but not least, the Ag-doped ZnO(0001) surface models were constructed to study the activation of the catalyst precursor under H₂-rich conditions. Hereafter, we will use AgO/ZnO to abbreviate the Ag-doped ZnO nanoparticles. For AgO/ZnO(0001) surfaces, we have first considered five uniform concentration gradients of Zn impurities, namely, in the range of 0–100 atom %, corresponding to the stoichiometry of the first cationic layer, namely, Ag₄, Ag₃Zn₁, Ag₂Zn₂, Ag₁Zn₃, and Zn₄. The Ag₂Zn₂ case is exemplified to be shown in Figure 1e. Furthermore, we took four oxygen vacancy (V_O) concentrations, that is, *s*V_O (25%), *d*V_O (50%), *t*V_O (75%), and *q*V_O (100%), into account for all studied AgO/ZnO(0001) surfaces. For all models, these studied active sites for CO₂ adsorption are equivalent with those on the pristine Ag(111) surface.

Kohn–Sham equations were solved by using the linear combination of atomic orbitals (LCAO) method, implemented in CRYSTAL09 code,¹⁰ with local Gaussian-type basis functions for all elements Zn,¹¹ Ag,¹² O,¹³ C,¹⁴ and H,¹⁵ respectively. We used the Perdew–Burke–Ernzerhof (PBE) functional¹⁶ at the level of the generalized gradient approximation (GGA) for electronic exchange–correlation interactions. Computational details are given in the Supporting Information.

RESULTS AND DISCUSSION

The adsorption energies were calculated by

$$E_{\text{ad}} = E_{\text{total}} - E_{\text{clean}} - \mu_{\text{CO}_2} \quad (1)$$

where the energies of the pristine and stretched Ag(111) surfaces, the *t*-Ag/ZnO, *b*-Ag/ZnO, and *m*-Ag/ZnO surfaces are defined by E_{clean} , and E_{total} indicates the total energies of

CO₂ adsorbed on the corresponding surfaces. The chemical potential of CO₂ was referred to its gaseous molecule. A negative value of the adsorption energies indicates an attractive interaction. The calculated adsorption energies indicate the binding between CO₂ molecule and the pristine Ag(111) surface is quite weak (−0.28 eV/CO₂). This is in agreement with experimental observations,¹⁷ where measured electron energy loss spectra (EELS) indicate a CO₂ molecule is just physisorbed on the Ag(111) surface. It can also be interpreted with the projected d-band states shown in Figure 2a. The d-

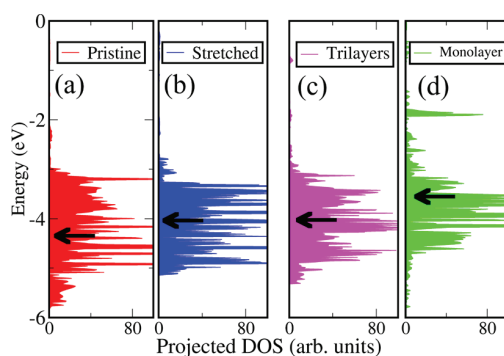


Figure 2. Projected d-band states are shown for the Ag atoms on (a) the pristine Ag(111) surface, (b) the Ag(111) surface with a tensile strain of 14%, (c) the *t*-Ag/ZnO surface, and (d) the *m*-Ag/ZnO surface. The Fermi level was specified to 0 eV for all models.

band center (−4.2 eV) is well below the Fermi level, which results in a remarkable occupied antibonding states. Thus, the d-band states of the pristine Ag(111) surface prefer to repulse dramatically the CO₂ molecule. For metal surfaces subject to certain strains, the overlap of d-band states at neighboring sites will either increase or decrease. The strains also influence its d-band widths. The d-band states move in energy to maintain a constant occupancy. Therefore, for the Ag(111) surface subject to a tensile strain, the tensile strain leads to upshifts of the d-band center. This is evident in the calculated P-DOS represented in Figure 2b. However, the d-band states shift of the stretched Ag(111) surface is only slight (0.2 eV). The binding strength of the CO₂ molecule with the stretched Ag(111) surface is not essentially improved (−0.40 eV/CO₂). Calculated adsorption energies for all studied surfaces are shown in Table 1. In addition, there is a similar behavior for the

Table 1. Calculated Adsorption Energies of CO₂ Molecule, E_{ad} , Are Given for All Studied Surfaces Including the Pristine and Stretched Ag(111) Surfaces, the *t*-Ag/ZnO, *b*-Ag/ZnO, and *m*-Ag/ZnO (Ag₄) Surfaces, and the *m*-Ag/ZnO Surfaces with a Certain Amount of Zn Impurities, Namely, Ag₃Zn₁, Ag₂Zn₂, and Ag₁Zn₃ (eV/CO₂)

surfaces	hcp	fcc	top	bridge
pristine Ag(111)	−0.10	−0.18	0.06	−0.28
stretched Ag(111)	−0.37	−0.38	−0.40	−0.38
<i>t</i> -Ag/ZnO	0.03	−0.26	0.12	−0.26
<i>b</i> -Ag/ZnO	−0.05	−0.21	0.10	−0.27
<i>m</i> -Ag/ZnO (Ag ₄)	−0.49	−0.20	−0.70	−0.96
Ag ₃ Zn ₁	−0.05	0.64	−0.75	−0.84
Ag ₂ Zn ₂	−0.92	−0.41	−0.64	−0.93
Ag ₁ Zn ₃	−0.99	−0.72	−0.49	−1.24

b-Ag/ZnO and *t*-Ag/ZnO surfaces. The d-band center of the *t*-Ag/ZnO surface is just slightly shifted toward the Fermi level, which is comparable with the stretched Ag(111) surface without a ZnO(0001) substrate. Significant and positive changes of the d-band states were observed in the *m*-Ag/ZnO interface. Partial d-states were shifted significantly up to the energy level of −2.0 eV. There are also more localized d-states appearing between the Fermi level and its d-band center (Figure 2d). Hence, the SMSI effect between the Ag(111) surface and the ZnO(0001) surface is not an extended interaction, but just confined at the interface. Calculated CO₂ adsorption energies and geometries are also in agreement with the d-band states features shown in Table 1 and Figure S2 of the Supporting Information. Because the adsorption energies are quite intermediate in strength around −1.0 eV/CO₂, we performed further calculations to investigate the subsequent CO₂ reduction on the *m*-Ag/ZnO surface.

In Figure 3, the reaction energies of hydrogenation process from CO₂ to methanol are shown. The CO₂ molecule can be

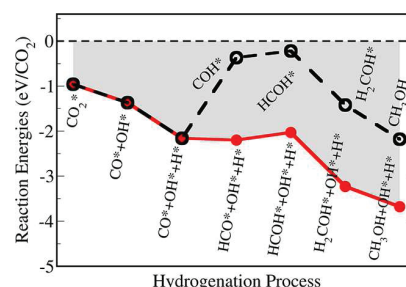


Figure 3. Reaction energies of hydrogenation process from CO₂ to methanol on the *m*-Ag/ZnO surface. The red and black curves correspond to the humid and dry conditions, respectively. The reaction energies are referred to the clean *m*-Ag/ZnO surface and gaseous CO₂, H₂O, and H₂ molecules. The asterisk is to clarify the adsorbed species.

cleaved at the first step of hydrogenation with the reaction energy of −1.37 eV/CO₂, with respect to the clean *m*-Ag/ZnO surface and gaseous CO₂, H₂O, and H₂ molecules. Its reaction barrier can be estimated with the fitted BEP relationship by Liu et al.⁵ It is in agreement with the previous analysis of CO₂ adsorption, too. Thus, the CO₂ activity on the *m*-Ag/ZnO surface is close to that on the Co(100) surface.⁵ Furthermore, the CO₂ dissociation is a hydrogen-assisted reaction on the *m*-Ag/ZnO surface. Therefore, this process can be improved significantly by means of tuning the experimental pressure of H₂ gas. After the second step of hydrogenation, the whole *m*-Ag/ZnO surface is rich of adsorbed hydroxyl and hydrogen groups. It can be expected there is an essential difference in a humid and dry environment (see Figure 3). The two curves from COH* to CH₃OH are almost parallel for both dry and humid conditions. The energetic difference is exactly the energy gain from H₂O dissociation on the *m*-Ag/ZnO surface. The humid condition does not improve the CO₂ activation directly but stabilizes the *m*-Ag/ZnO surface by H₂O dissociation. Therefore, this is an important and indirect improvement for CO₂ reductions. In the remainder, we will analyze this influence for the AgO/ZnO based catalysts in the presence of H₂ gas.

In previous experiments, the magnetron sputtering technique is available to deposit an Ag(111) film on the ZnO(0001) substrate.¹⁸ The layered Ag/ZnO interface is free of defects.

But it contains many heterophase interfaces, which generate dramatic strains due to the lattice mismatch as we have analyzed. Therefore, the formation of a coherent (1×1) Ag/ZnO interface with thick Ag overlayers is expected to be difficult since it would be highly unstable. Indeed, the coherent (1×1) interface had not been observed in any previous experiment. In addition, it does not make sense either because the thick Ag overlayers are not active for CO₂ adsorption. However, we found the *m*-Ag/ZnO, *b*-Ag/ZnO, and *t*-Ag/ZnO interfaces are indeed stable because the Ag overlayers are extremely thin (see Table S4). Mulliken charges analysis indicates there is charge transfer of 0.12 electron at these interfaces, accompanied by forming strong Ag–O bonds. However, there are no any interface interactions propagating to the second and third overlayers. In short, the optimized catalysis can be achieved on an extremely dispersed Ag(111) monolayer supported on the ZnO(000 $\bar{1}$) substrate.

For realistic *m*-Ag/ZnO systems, the *m*-Ag/ZnO is finite with some edge states. Thanks to high energetic edge states, the *m*-Ag/ZnO surface can be reconstructed. The observed tensile strain in experiment should be smaller than 14% in our theoretical model. However, we would point out that the tensile strain of 14% is not necessary for activating the Ag(111) surface (Table 1). In contrast, the calculated *m*-Ag/ZnO is active for CO₂ adsorption, but the stretched one is not. That suggests the activation is not due to stretching but the oxygen-terminated support. Therefore, the CO₂ activity on the reconstructed *m*-Ag/ZnO surfaces should not be influenced.

On the one hand, for the industrial Cu/ZnO/Al₂O₃ catalyst, it is prepared by a coprecipitation technique.¹⁹ The structural evolution during activation of the catalyst has been characterized thoroughly with several *in situ* experimental techniques, where the Cu atoms first were present in the form of substitutional Cu²⁺ in the CuO/ZnO solid solution, as determined with *in situ* resonant X-ray diffraction and EELS techniques. Then, the Cu atoms were extracted from the CuO/ZnO solid solution under the reductive atmosphere, accompanied by forming metallic Cu crystallites. On the other hand, Li et al.²⁰ had performed first principles calculations to determine the local Ag-derived structures in Ag-doped ZnO nanowires. Calculated formation energies are very low for Ag dopants at substitutional-Zn sites under both cases of low and high Ag dopants concentration, but rather high at substitutional-O and interstitial sites under O₂-rich conditions. It was also validated in the latest combinational calculations and measurements that the dominant Ag dopants are substitution for the Zn sites.²¹ Therefore, we considered further a similar strategy to improve the dispersion of Ag atoms on the ZnO(000 $\bar{1}$) surface. The critical issue is if the AgO/ZnO-based precursor can be activated spontaneously in practice. Moreover, we have to consider the *m*-Ag/ZnO with a certain amount of Zn impurities in this experimental technique. In this work, we assume the CO₂ reduction is performed in the presence of gaseous H₂ atmosphere. Then, we performed calculations to investigate the stability of AgO/ZnO(000 $\bar{1}$) surfaces. Formation energies of V_O defects on AgO/ZnO(000 $\bar{1}$) surfaces are defined by

$$E_f = \frac{1}{A} [E_d + \sum n_O \mu_O - E_p] \quad (2)$$

where E_p and E_d indicate energies of perfect AgO/ZnO(000 $\bar{1}$) surfaces and these surfaces with V_O defects, with respect to

surface area, A , respectively. Chemical potentials of surface oxygen are estimated under the O₂-rich and H₂-rich conditions.

For the Ag₄ (*m*-Ag/ZnO) case, it prefers to be reduced completely, accompanied by a number of V_O defects formed under H₂-rich condition (see Figure 4). That means the AgO/

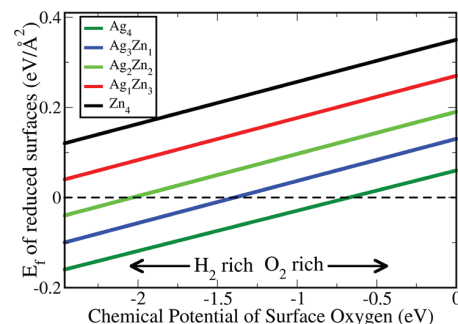


Figure 4. Phase diagram of full reduced AgO/ZnO(000 $\bar{1}$) surfaces, namely, the AgO/ZnO(000 $\bar{1}$) surfaces with qV_O defects, under the H₂-rich and O₂-rich conditions. The dashed line indicates the perfect AgO/ZnO(000 $\bar{1}$) surfaces.

ZnO based catalyst can be activated in the Ag₄ case to generate the *m*-Ag/ZnO surface. Herein, the Ag₄ surface is equivalent completely to the above *m*-Ag/ZnO surface. The detailed structures of all reduced AgO/ZnO (000 $\bar{1}$) surfaces are given in Figure S3. In the presence of Zn impurities, the Ag₃Zn₁ and Ag₂Zn₂ surfaces with qV_O defects are also stable under H₂-rich condition. However, for the Zn₄ case, it does not prefer to be reduced completely to produce a metallic Zn monolayer. Because the Ag element possesses full occupied d-orbitals (d¹⁰), hence, the Ag¹⁺ is more stable rather than Ag²⁺ cation. However, the Ag substitution for Zn atoms can introduce Ag²⁺, instead of Ag¹⁺, into the ZnO wurtzite structure. Therefore, the Ag dopants are more favorable on surfaces with less coordination, in way of the V_O defects formation. This mechanism is consistent with the synergistic effects recently found on the Cu/ZnO(000 $\bar{1}$) surface.²² In addition, accompanied by the reduction of the AgO/ZnO(000 $\bar{1}$) surface, one of the reduced products, H₂O, is likely to be adsorbed and dissociated on the Ag₄ (*m*-Ag/ZnO) surface. In Figure 3, the calculated two reaction paths indicate the humid condition provides a quite improved condition for subsequent hydrogenation from the CO* species to methanol. Hence, the AgO/ZnO(000 $\bar{1}$) surface can indeed serve as an optimized precursor of catalyst for CO₂ reduction in the presence H₂ gas. Moreover, there are a comparable adsorption ability with the Ag₄ surface (−0.96 eV/CO₂), namely, −0.84 eV/CO₂ for the Ag₃Zn₁ surface and −0.93 eV/CO₂ for the Ag₂Zn₂ surface. Further calculations for the subsequent hydrogenation indicate the Zn impurities do not result in a negative influence for CO₂ reduction. All hydrogenation steps are quite preferable on both Ag₃Zn₁ and Ag₂Zn₂ surfaces. Detailed reaction energies of hydrogenation on the Ag₃Zn₁ and Ag₂Zn₂ surfaces are given in Table S6. As a consequence, for the AgO/ZnO-based catalysts, the efficiency of Ag utilization can be improved further, in comparison with a deposited Ag(111) monolayer on the ZnO(000 $\bar{1}$) substrate. In short, the Ag dopants can facilitate the V_O defects formation and generate certain metallic monolayers. Meanwhile, the d-band states of these metallic monolayers are quite optimized for CO₂ adsorption and reduction. Therefore,

the catalysis of the Ag(111)/ZnO(000 $\bar{1}$) surfaces is improved by the synergetic effects.

CONCLUSION

In conclusion, we have first studied the d-band states of pristine Ag(111) surface and the same surface subject to a certain tensile strain. It has been found slight upshifts of the d-band states occurs for the stretched surface, in comparison with the pristine one, as expected with the d-band model. However, the CO₂ adsorption on the stretched surface is still too weak to initiate the subsequent CO₂ conversion. Because of the strong metal–support interaction, the stretched Ag(111) monolayer supported on the ZnO(000 $\bar{1}$) substrate can bind with a CO₂ molecule at an intermediate strength. Therefore, we have further investigated the CO₂ reduction on the Ag(111) monolayer with the ZnO support. It was demonstrated that this surface can serve as an optimized catalyst for CO₂ reduction. Furthermore, we have studied the phase diagram for Ag-doped ZnO(000 $\bar{1}$) surface under H₂-rich and O₂-rich conditions, respectively. The fully reduced Ag-doped ZnO(000 $\bar{1}$) surface, which is equivalent to the above *m*-Ag/ZnO surface, is shown to be indeed stable in the presence of a gaseous H₂ atmosphere. The reactivity of CO₂ adsorption and reduction on the surfaces does not turn out to be influenced by the Zn impurities. Instead, the efficiency of Ag utilization can be improved significantly using Ag-doped ZnO as a catalyst precursor.

ASSOCIATED CONTENT

Supporting Information

Computational details, stability of full reduced Ag-doped ZnO surface, and detailed reaction energies of hydrogenation. This material is available free of charge via the Internet at <http://pubs.acs.org>.

AUTHOR INFORMATION

Corresponding Author

*E-mail xiao@bccms.uni-bremen.de.

Notes

The authors declare no competing financial interest.

ACKNOWLEDGMENTS

J. Xiao acknowledges financial supporting by the Chinese Scholarship Council (CSC) and providing computational resources of hardware and software by BCCMS (Bremen Center for Computational Materials Science), Universität Bremen.

REFERENCES

- (1) Maginn, E. J. What to Do with CO₂. *J. Phys. Chem. Lett.* **2010**, *1*, 3478–3479.
- (2) (a) Nørskov, J. K.; Bligaard, T.; Rossmeisl, J.; Christensen, C. H. Towards the Computational Design of Solid Catalysts. *Nat. Chem.* **2009**, *1*, 37–46. (b) Hammer, B.; Nørskov, J. K. Why Gold Is the Noblest of All the Metals. *Science* **1995**, *376*, 238–240. (c) Nørskov, J. K.; Abild-Pedersen, F.; Studt, F.; Bligaard, T. Density Functional Theory in Surface Chemistry and Catalysis. *Proc. Natl. Acad. Sci. U. S. A.* **2011**, *108*, 937–943.
- (3) Hammer, B.; Nørskov, J. K. Theoretical Surface Science and Catalysis - Calculations and Concepts. *Adv. Catal.* **2000**, *45*, 71–129.
- (4) Nørskov, J. K.; Bligaard, T.; Hvolbæk, B.; Abild-Pedersen, F.; Chorkendorff, L.; Christensen, C. H. The Nature of the Active Site in Heterogeneous Metal Catalysis. *Chem. Soc. Rev.* **2008**, *37*, 2163–2171.

- (5) Liu, C.; Cundari, T. R.; Wilson, A. K. CO₂ Reduction on Transition Metal (Fe, Co, Ni, and Cu) Surfaces: In Comparison with Homogeneous Catalysis. *J. Phys. Chem. C* **2011**, *116*, 5681–5688.

- (6) (a) Green, I. X.; Tang, W.; Neurock, M.; Yates, J. T., Jr. Spectroscopic Observation of Dual Catalytic Sites during Oxidation of CO on a Au/TiO₂ Catalyst. *Science* **2011**, *333*, 736–739. (b) Qiao, B.; Wang, A.; Yang, X.; Allard, L. F.; Jiang, Z.; Cui, Y.; Liu, J.; Li, J.; Zhang, T. Single-Atom Catalysis of CO Oxidation Using Pt₁/FeO_x. *Nat. Chem.* **2011**, *3*, 634–641. (c) Ma, C. Y.; Mu, Z.; Li, J. J.; Jin, Y. G.; Cheng, J.; Lu, G. Q.; Hao, Z. P.; Qiao, S. Z. Mesoporous Co₃O₄ and Au/Co₃O₄ with High Catalytic Activities for Oxidation of Trace Ethylene. *J. Am. Chem. Soc.* **2010**, *132*, 2608–2613. (d) Fu, Q.; Saltsburg, H.; Flytzani-Stephanopoulos, M. Active Nonmetallic Au and Pt Species on Ceria-Based Water-Gas Shift Catalysts. *Science* **2003**, *301*, 935–938.

- (7) (a) Tauster, S. J. Strong Metal-Support Interactions. *Acc. Chem. Res.* **1987**, *20*, 389–394. (b) Haller, G. L.; Resasco, D. E. Metal-Support Interaction: Group VIII Metals and Reducible Oxides. *Adv. Catal.* **1989**, *36*, 173–235. (c) Chen, M. S.; Goodman, D. W. The Structure of Catalytically Active Gold on Titania. *Science* **2004**, *306*, 252–255. (d) Fu, Q.; Wagner, T. Interaction of Nanostructured Metal Overlayers with Oxide Surface. *Surf. Sci. Rep.* **2007**, *62*, 431–498.

- (8) Satterfield, C. N. *Heterogeneous Catalysis in Practice*; McGraw-Hill: New York, 1980.

- (9) Mavrikakis, M.; Hammer, B.; Nørskov, J. K. Effect of Strain on the Reactivity of Metal Surfaces. *Phys. Rev. Lett.* **1998**, *81*, 2819–2822.

- (10) Dovesi, R.; Saunders, V. R.; Roetti, C.; Orlando, R.; Zicovich-Wilson, C. M.; Pascale, F.; Civalieri, B.; Doll, K.; Harrison, N. M.; Bush, I. J.; D'Arco, Ph.; Llunell, M. CRYSTAL09, User's Manual, University of Torino, Torino, 2009.

- (11) Jaffe, J. E.; Hess, A. C. Hartree-Fock Study of Phase Changes in ZnO at High Pressure. *Phys. Rev. B* **1993**, *48*, 7903–7909.

- (12) Aprà, E.; Stefanovich, E.; Dovesi, R.; Roetti, C. An Ab Initio Hartree-Fock Study of Silver Chloride. *Chem. Phys. Lett.* **1991**, *186*, 329–335.

- (13) Corno, M.; Busco, C.; Civalieri, B.; Ugliengo, P. Periodic Ab Initio Study of Structural and Vibrational Features of Hexagonal Hydroxyapatite Ca₁₀(PO₄)₆(OH)₂. *Phys. Chem. Chem. Phys.* **2006**, *8*, 2464–2472.

- (14) Gatti, C.; Saunders, V. R.; Roetti, C. Crystal-Field Effects on the Topological Properties of the Electron-Density in Molecular-Crystals - the Case of Urea. *J. Chem. Phys.* **1994**, *101*, 10686–10696.

- (15) Dovesi, R.; Ermondi, E.; Ferrero, E.; Pisani, C.; Roetti, C. Hartree-Fock Study of Lithium Hydride with the Use of a Polarizable Basis Set. *Phys. Rev. B* **1983**, *29*, 3591–3600.

- (16) Perdew, J. P.; Burke, K.; Ernzerhof, M. Generalized Gradient Approximation Made Simple. *Phys. Rev. Lett.* **1996**, *77*, 3865–3868.

- (17) Sakurai, M.; Okano, T.; Tuzi, Y. Vibrational Excitation of Physisorbed CO₂ on a Ag(111) Surface. *J. Vac. Sci. Technol., A* **1987**, *5*, 431–434.

- (18) Barthel, E.; Kerjan, O.; Nael, P.; Nadaud, N. Asymmetric Silver to Oxide Adhesion in Multilayers Deposited on Glass by Sputtering. *Thin Solid Films* **2005**, *473*, 272–277.

- (19) Andreasen, J. W.; Rasmussen, F. B.; Helveg, S.; Molenbroek, A.; Ståhl, K.; Nielsen, M. M.; Feidenhansl, R. Activation of a Cu/ZnO Catalyst for Methanol Synthesis. *J. Appl. Crystallogr.* **2006**, *39*, 209–221.

- (20) Li, Y.; Zhao, X.; Fan, W. Structural, Electronic, and Optical Properties of Ag-Doped ZnO Nanowires: First Principles Study. *J. Phys. Chem. C* **2011**, *115*, 3552–3557.

- (21) Thomas, M. A.; Sun, W. W.; Cui, J. B. Mechanism of Ag Doping in ZnO Nanowires by Electrodeposition: Experimental and Theoretical Insights. *J. Phys. Chem. C* **2012**, *116*, 6383–6391.

- (22) Xiao, J.; Frauenheim, T. Activity and Synergy Effects on a Cu/ZnO(000 $\bar{1}$) Surface Studied Using First-Principle Thermodynamics. *J. Phys. Chem. Lett.* **2012**, *3*, 2638–2642.

Contents

Computational details.

Table S1. Calculated surface energies of full optimized Ag(111) slab models of five (L_5), six (L_6), and seven (L_7) atomic layers are relative to metallic Ag bulk, respectively.

Table S2. Calculated CO₂ adsorption energies at the bridge site of the pristine Ag(111) surface are given with respect to the clean and pristine Ag(111) surface and gaseous CO₂ molecule.

Table S3. Energy differences between relaxed and non-relaxed ZnO(0001) surface models are given for four bilayers (L_4), six bilayers (L_6) and eight bilayers (L_8) slabs, respectively ($eV/\text{\AA}^2$).

Table S4. Calculated formation energies of Ag/ZnO interfaces are given for the m-Ag/ZnO, b-Ag/ZnO, and t-Ag/ZnO models, respectively ($eV/\text{\AA}^2$).

Figure S1. Schematic illustrations of the m-Ag/ZnO, b-Ag/ZnO, and t-Ag/ZnO interfaces are represented in white (Ag), blue (Zn), and red (O) spheres, respectively.

Figure S2. Side views of geometries of adsorbed CO₂ molecule on (a) the pristine Ag(111) surface, (b) the stretched Ag(111) surface, (c) the t-Ag/ZnO surface, (d) the m-Ag/ZnO surface are indicated in yellow (C), white (Ag), and red (O) spheres, respectively. The average distances between CO₂ and these surfaces are given in angstrom (\AA).

Table S5. Calculated cleavage energies differences between the pure ZnO(0001) surface and AgO/ZnO(0001) surfaces are given in eV/unit cell.

Table S6. Calculated formation energies, E_f , in the varying concentrations of oxygen vacancies defects, namely, sV_O, dV_O, tV_O and qV_O on various studied Zn₄, Ag₁Zn₃, Ag₂Zn₂, Ag₃Zn₁, and Ag₄ surfaces, are given under H₂-rich condition ($meV/\text{\AA}^2$).

Figure S3. Top view of full reduced AgO/ZnO(0001) surfaces, that is, these surfaces with qV_O defects, are represented in white (Ag) and blue (Zn) spheres for (a) Zn₄, (b) Ag₁Zn₃, (c) Ag₂Zn₂, (d) Ag₃Zn₁, (e) Ag₄ surfaces, respectively. Bold lines indicate chemical bonds.

Table S7. Reaction energies of CO₂ hydrogenation are calculated with respect to the clean Ag₂Zn₂ and Ag₃Zn₁ surfaces and gaseous CO₂ and H₂ phases (eV/CO_2).

Computational Details

For the pristine and stretched Ag(111) surfaces, we have employed (2×2) slab models with five atomic layers. Calculated surface energies of slab models with five, six, and seven layers are given in **Table S1**. The surface energies differences are comparable with the accuracy of DFT method.

Table S1. Calculated surface energies of full optimized Ag(111) slab models of five (L_5), six (L_6), and seven (L_7) atomic layers are relative to metallic Ag bulk, respectively.

Models	$E_{\text{surface}} - E_{\text{bulk}}$ (eV/Å ²)
L_5	0.62
L_6	0.61
L_7	0.61

The CO₂ adsorption energy convergence was also tested using different k-point sampling (**Table S2**). Finally, the irreducible Brillouin zones were always sampled with (4×4×1) space grids for all models in this work.

Table S2. Calculated CO₂ adsorption energies at the bridge site of the pristine Ag(111) surface are given with respect to the clean and pristine Ag(111) surface and gaseous CO₂ molecule.

K points	E_{ad} (eV/CO ₂)
4×4×1	-0.28
10×10×1	-0.27
16×16×1	-0.25

In addition, we have used periodic (2×2) slab models of four bilayers to simulate ZnO(000 $\bar{1}$) surfaces (see **Table S3**). We have optimized the first two Zn-O bilayers and fixed the remaining layers in their bulk structure. The opposite Zn termination, namely, the ZnO(0001) surface, was always saturated by hydrogen atoms. As the ZnO(000 $\bar{1}$) surface is a typical polar surface, it is quite difficult to construct a perfect slab model with converged sufficiently surface energy. The four bilayers model of the ZnO(000 $\bar{1}$) surface has an acceptable accuracy at DFT calculation level to account for surface relaxation. Please see the comparisons for different models in **Table S3**.

Table S3. Energy differences between relaxed and non-relaxed ZnO(000 $\bar{1}$) surface models are given for four bilayers (L_4), six bilayers (L_6) and eight bilayers (L_8) slabs, respectively (eV/Å²).

Models	$E_{\text{relaxed}} - E_{\text{non-relaxed}}$
L_4	-0.07
L_6	-0.08
L_8	-0.08

The stretched Ag(111) surfaces supported on the ZnO(0001) substrate are shown in **Figure S1**. All overlayers and the first two atomic layers (denoted in the dashed box in **Figure S1**) of the ZnO (0001) surface were allowed to relax in this work.

The formation energies of Ag/ZnO interfaces are defined by

$$E_{\text{interface}} = E_{\text{total}} - E_{\text{overlayers}} - E_{\text{substrate}}$$

Where E_{total} is the total energies of Ag/ZnO interface models, $E_{\text{overlayers}}$ corresponds to the energies of the isolated Ag(111) monolayer, bilayers, and trilayers, and $E_{\text{substrate}}$ is the energy of isolated ZnO(0001) substrate. A negative value indicates a stable Ag/ZnO interface. The geometries and formation energies of Ag/ZnO interfaces are given in **Table S4** and **Figure S1**.

Table S4. Calculated formation energies of Ag/ZnO interfaces are given for the *m*-Ag/ZnO, *b*-Ag/ZnO, and *t*-Ag/ZnO models, respectively ($\text{eV}/\text{\AA}^2$).

Models	$E_{\text{interface}}$
<i>m</i> -Ag/ZnO	-0.05
<i>b</i> -Ag/ZnO	-0.22
<i>t</i> -Ag/ZnO	-0.15

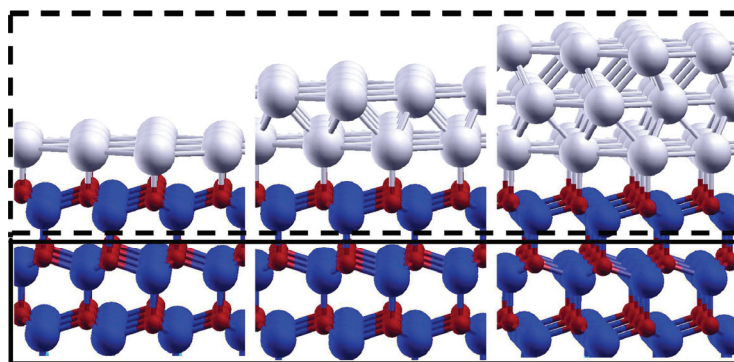


Figure S1. Schematic illustrations of the *m*-Ag/ZnO, *b*-Ag/ZnO, and *t*-Ag/ZnO interfaces are represented in white (Ag), blue (Zn), and red (O) spheres, respectively.

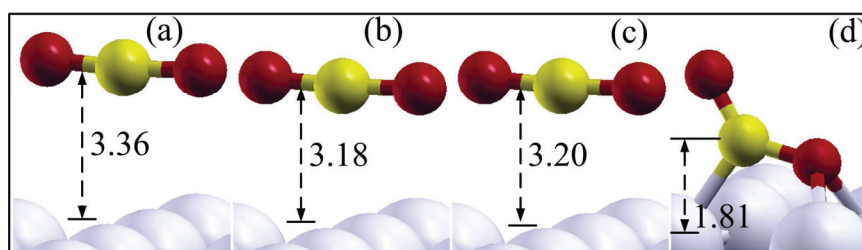


Figure S2. Side views of geometries of adsorbed CO₂ molecule on (a) the pristine Ag(111) surface, (b) the stretched Ag(111) surface, (c) the *t*-Ag/ZnO surface, (d) the *m*-Ag/ZnO surface are denoted in yellow (C), white (Ag), and red (O) spheres, respectively. The average distances between CO₂ and these surfaces are given in angstrom (\AA).

In order to identify the Ag distribution in the AgO/ZnO matrix, the cleavage energy of the pure ZnO and AgO/ZnO bulk was defined in this work by

$$E_{\text{cleavage}} = E_{\text{surface}} - E_{\text{bulk}}$$

The cleavage energies differences, ΔE , are described in the following equations

$$\Delta E = E_{\text{cleavage}}^{\text{AgO/ZnO}} - E_{\text{cleavage}}^{\text{ZnO}}$$

A negative value of ΔE indicates that the Ag dopants are favorable to distribute on the ZnO(0001) surface, instead in ZnO bulk. The calculated ΔE values shown in **Table S5** suggest the Ag atoms prefer to locate on the Ag₄ and Ag₃Zn₁ surfaces.

Table S5. Calculated cleavage energies differences between the pure ZnO(0001) surface and AgO/ZnO(0001) surfaces are given in eV/unit cell.

Models	ΔE (eV/unit cell)
Ag ₄	-0.29
Ag ₃ Zn ₁	-0.10
Ag ₂ Zn ₂	0.03
Ag ₁ Zn ₃	0.22
Zn ₄	0.00

The oxygen vacancies formation energies are given in **Table S6**. It indicates the defective Ag₂Zn₂, Ag₃Zn₁, and Ag₄ surfaces are stable under H₂-rich condition. The corresponding geometries for these full reduced surfaces are illustrated in **Figure S3**.

Table S6. Calculated formation energies, E_f , in the varying concentrations of oxygen vacancies defects, namely, sV_O, dV_O, tV_O and qV_O on various studied Zn₄, Ag₁Zn₃, Ag₂Zn₂, Ag₃Zn₁, and Ag₄ surfaces, are given under H₂-rich condition (meV/Å²).

Surfaces	sV _O	dV _O	tV _O	qV _O
Zn ₄	12	50	86	120
Ag ₁ Zn ₃	21	4	17	38
Ag ₂ Zn ₂	-5	-20	-39	-36
Ag ₃ Zn ₁	-36	-66	-103	-97
Ag ₄	-61	-114	-149	-163

Note: the stable V_O defects are marked in italic and blue.

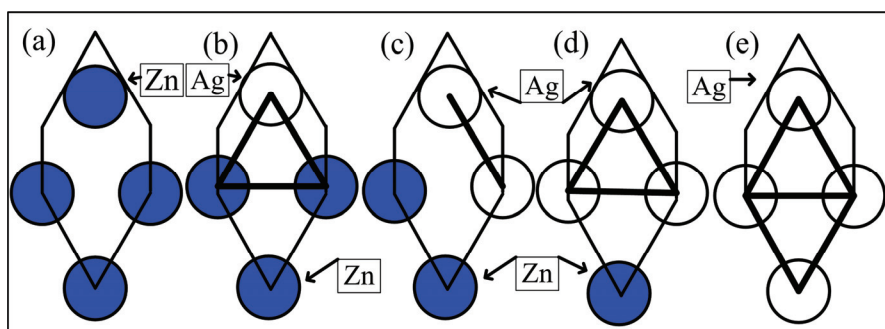


Figure S3. Top views of full reduced AgO/ZnO (0001) surfaces, that is, these surfaces with qV_o defects, are represented in white (Ag) and blue (Zn) spheres for (a) Zn_4 , (b) Ag_1Zn_3 , (c) Ag_2Zn_2 , (d) Ag_3Zn_1 , (e) Ag_4 surfaces, respectively. Bold lines indicate chemical bonds.

We performed further investigations for hydrogenation on the Ag_2Zn_2 and Ag_3Zn_1 surfaces. The energetic evolution processes are listed in **Table S7**. It indicates the hydrogenation processes are also preferable on the two surfaces too.

Table S7. Reaction energies of CO_2 hydrogenation are calculated with respect to the clean Ag_2Zn_2 and Ag_3Zn_1 surfaces and gaseous CO_2 and H_2 phases (eV/ CO_2).

	+1H	+2H	+3H	+4H	+5H	+6H
	*COOH	*HCOOH	*H ₂ COOH	*CH ₃ O+*OH	*CH ₃ OH+*OH	CH ₃ OH+*OH+H*
Ag_2Zn_2	-1.34	-1.75	-3.04	-4.26	-3.94	-3.88
Ag_3Zn_1	-2.41	-1.86	-2.06	-2.51	-3.20	-3.25